Technische Universität Berlin
Fakultät V
Institut für Strömungsmechanik und Technische Akustik (ISTA)

Large-eddy simulation and resolvent-based modelling of coherent structures in the boundary layer of a 2D airfoil

Master thesis

Advisors: Prof. Kilian Oberleithner
M. Sc. Jens Müller

Submitted by

Maximilian Brömmer

December 14, 2020

Eidesstattliche Erklärung

Hiermit versichere ich, dass ich die vorliegende Arbeit selbstständig verfasst und keine anderen als die angegebenen Quellen und Hilfsmittel benutzt habe. Alle Ausführungen, die anderen veröffentlichten oder nicht veröffentlichten Schriften wörtlich oder sinngemäß entnommen wurden, habe ich kenntlich gemacht.

Die Arbeit hat in gleicher oder ähnlicher Fassung noch keiner anderen Prüfungsbehörde vorgelegen.

Düsseldorf, 11.12.2020

Ort, Datum

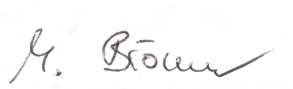

Unterschrift

Zusammenfassung

Diese Arbeit behandelt die Analyse und Modellierung von kohärenten Strukturen in der turbulenten Grenzschicht an einem Flügelprofil. Die Interaktion von Wirbeln einer turbulenten Strömung mit einer Wand führt zur Schallentstehung, beispielsweise zu Hinterkantenlärm der auch bei Windenergieanlagen auftritt. Durch tieferes Verständnis über entstehende Strukturen in der turbulenten Grenzschicht wird angestrebt in Zukunft geeignete Methoden zur Reduzierung von Lärm zu finden. Bei dem untersuchten Fall handelt es sich um das "Clark-Y"-Profil mit einem Anstellwinkel von 9° und einer Reynoldszahl von 295.005, wobei ein starker positiver Druckgradient auf der Saugseite anzutreffen ist. Zunächst wird eine dreidimensionale Large-eddy Simulation (LES) durchgeführt, bei der die Transition auf der Saugseite durch ein Stolperelement ausgelöst wird. Die Ergebnisse der Simulation werden mithilfe der "Spectral proper orthogonal decomposition"-Methode (SPOD) untersucht. Dabei werden Kelvin-Helmholtz-Moden auf der Saugseite des Profils festgestellt. Außerdem wird zur Modellierung der Strukturen, die in der turbulenten Grenzschicht entstehen, die zweidimensionale globale Resolvent Analyse angewandt. Diese wird bei der Berechnung durch ein Wirbelviskositätsmodell ergänzt. Dabei werden bei niederfrequenten Moden wieder Kelvin-Helmholtz-Strukturen auf der Saugseite beobachtet. Bei höheren Frequenzen treten dominante Strukturen an der Vorderkante des Flügelprofils auf. Im Vergleich der beiden Ergebnisse werden Übereinstimmungen in der Gestalt der Moden gefunden, womit weitere Untersuchungen von kohärenten Strukturen mithilfe der Resolvent Analyse in einer breitbandigen Strömung vielversprechend sind.

Abstract

This thesis covers the analysis and modeling of coherent structures in the turbulent boundary layer of an airfoil. The interaction of turbulent eddies and a wall lead to noise, for instance trailing-edge noise, which occurs in the operation of wind turbines. Through profound knowledge of the evolving structures in a turbulent boundary layer, suitable methods to reduce noise are pursued in the future. The investigated case deals with the "Clark-Y" profile with an angle of attack of 9° and a Reynolds number of 295,005, thereby a high positive pressure gradient on the suction side is obtained. First of all a three-dimensional large-eddy simulation (LES) is conducted, where transition is induced by an tripping element on the suction side. The results are examined by spectral proper orthogonal decomposition (SPOD). In the resulting modes Kelvin-Helmholtz structures are found on the suction side. Besides modeling of the structures is executed by a two-dimensional global resolvent analysis supplemented by an eddy-viscosity approach. For low frequency modes Kelvin-Helmholtz structures are detected as well, but for higher frequencies structures at the leading edge are the dominant force. In the comparison of both methods promising agreements between the shape of the modes are found, which support further investigations in resolvent-based modeling of structures in a broadband flow.

Contents

List of Figures V

List of Tables VII

List of Symbols VIII

List of Acronyms X

1 Introduction 1

2 Governing Equations 3
- 2.1 Large-Eddy Simulation . . . 3
  - 2.1.1 General . . . 3
  - 2.1.2 Dynamic Smagorinsky model . . . 4
- 2.2 Spectral Proper Orthogonal Decomposition . . . 6
- 2.3 Resolvent Analysis . . . 8

3 Numerical Setup 11
- 3.1 Large-Eddy Simulation . . . 11
  - 3.1.1 General . . . 11
  - 3.1.2 Mesh . . . 12
  - 3.1.3 Solver . . . 13
  - 3.1.4 Boundary layer tripping . . . 15
  - 3.1.5 Solution and simulation process . . . 17
- 3.2 Resolvent Analysis . . . 18

4 Results 21
- 4.1 LES . . . 21
  - 4.1.1 Reference cases . . . 21
  - 4.1.2 Instantaneous fields . . . 24
  - 4.1.3 Mean flow fields . . . 24
  - 4.1.4 Boundary layer profiles . . . 27
  - 4.1.5 Spectral analysis . . . 30
- 4.2 SPOD . . . 33
  - 4.2.1 Non-averaged flow . . . 33
  - 4.2.2 Span-averaged flow . . . 35
  - 4.2.3 Weighted span-averaged flow . . . 38
- 4.3 Resolvent Analysis . . . 42
  - 4.3.1 Velocity responses and gain distribution . . . 42
  - 4.3.2 Pressure responses and simulation issues . . . 49
  - 4.3.3 Mesh independence . . . 50
- 4.4 Comparison between SPOD and Resolvent Analysis . . . 52

4.4.1 Contour plots 52
4.4.2 Profile of the magnitude of the mode 56

5 Discussion **60**

6 Conclusions **63**

References **65**

List of Figures

Figure 1: Filtering process . . . 4
Figure 2: LES: Whole Mesh . . . 13
Figure 3: LES: Mesh around the airfoil . . . 14
Figure 4: Refinement levels . . . 14
Figure 5: Probe locations and refinement . . . 14
Figure 6: Near wall resolution at the trailing edge . . . 15
Figure 7: y^+-values . . . 16
Figure 8: Boundary layer trip . . . 17
Figure 9: Total viscosity ν_{tot} with the sponge layer . . . 18
Figure 10: Total viscosity ν_{tot} near the airfoil . . . 19
Figure 11: Resolvent: Whole mesh . . . 19
Figure 12: Resolvent: Near wall mesh . . . 20
Figure 13: Pressure coefficient C_p . . . 22
Figure 14: Skin friction coefficient C_f . . . 22
Figure 15: Skin friction coefficient C_f - dynamic Lagrangian Smagorinsky model 23
Figure 16: Drag coefficient C_d . . . 24
Figure 17: Lift coefficient C_l . . . 24
Figure 18: Snapshots at $t = 0.155\,76\,\mathrm{s}$ . . . 25
Figure 19: Mean flow fields of xy-plane at $z = 0\,\mathrm{m}$ . . . 26
Figure 20: Streamlines at the trailing edge and the mean velocity magnitude $|\overline{\boldsymbol{u}}|$ 27
Figure 21: Span-averaged Reynolds stresses . . . 28
Figure 22: Nondimensional boundary layer profiles . . . 29
Figure 23: Reynolds stresses in the boundary layer . . . 31
Figure 24: Power density spectrum - left: $x/c = 0.23$, middle: $x/c = 0.59$, right: $x/c = 0.95$ - top: buffer layer, middle: log layer, bottom: outer region 32
Figure 25: Eigenvalues over frequency of the SPOD . . . 33
Figure 26: SPOD modes at $f = 227\,\mathrm{Hz}$ . . . 34
Figure 27: Eigenvalues over frequency of the span-averaged SPOD . . . 35
Figure 28: SPOD modes at $f = 227\,\mathrm{Hz}$ of the span-averaged flow . . . 36
Figure 29: SPOD modes at $f = 445\,\mathrm{Hz}$ of the span-averaged flow . . . 37
Figure 30: SPOD modes at $f = 909\,\mathrm{Hz}$ of the span-averaged flow . . . 37
Figure 31: SPOD mode at $f = 3750\,\mathrm{Hz}$ of the span-averaged flow . . . 38
Figure 32: Eigenvalues over frequency of the weighted SPOD . . . 39
Figure 33: Weighted SPOD modes at $f = 227\,\mathrm{Hz}$ . . . 39
Figure 34: Weighted SPOD modes at $f = 568\,\mathrm{Hz}$ . . . 40
Figure 35: Weighted SPOD modes at $f = 909\,\mathrm{Hz}$ . . . 41
Figure 36: Weighted SPOD modes at $f = 568\,\mathrm{Hz}$ near leading edge . . . 41
Figure 37: Second and third SPOD mode at $f = 568\,\mathrm{Hz}$ . . . 42
Figure 38: Resolvent response modes at $f = 227\,\mathrm{Hz}$ . . . 43
Figure 39: Resolvent response modes at $f = 227\,\mathrm{Hz}$ near wall . . . 43

Figure 40: Resolvent forcing modes at $f = 341\,\mathrm{Hz}$ near wall . . . 44
Figure 41: Resolvent response modes at $f = 568\,\mathrm{Hz}$ . . . 45
Figure 42: Resolvent response modes at $f = 568\,\mathrm{Hz}$ near wall . . . 46
Figure 43: Resolvent response modes at $f = 909\,\mathrm{Hz}$ . . . 47
Figure 44: Resolvent response modes at $f = 909\,\mathrm{Hz}$ near wall . . . 47
Figure 45: Gain distribution . . . 48
Figure 46: Resolvent response modes at $f = 227\,\mathrm{Hz}$ near wall . . . 48
Figure 47: Resolvent response modes at $f = 227\,\mathrm{Hz}$ near wall . . . 49
Figure 48: Mesh independence: First mode of velocity component u' at $f = 227\,\mathrm{Hz}$ 50
Figure 49: Mesh independence: Gain distribution . . . 51
Figure 50: First velocity modes at $f = 227\,\mathrm{Hz}$, left: resolvent, right: SPOD, top: u', bottom: v' . . . 52
Figure 51: First velocity modes at $f = 909\,\mathrm{Hz}$, left: resolvent, right: SPOD, top: u', bottom: v' . . . 53
Figure 52: Comparison of velocity component u' at $f = 341\,\mathrm{Hz}$ in the boundary layer . . . 54
Figure 53: Comparison of velocity component v' at $f = 341\,\mathrm{Hz}$ in the boundary layer . . . 54
Figure 54: Comparison of velocity component v' at $f = 454\,\mathrm{Hz}$ in the boundary layer . . . 55
Figure 55: Comparison at $f = 909\,\mathrm{Hz}$ . . . 56
Figure 56: Velocity profiles at $x/c = 0.23$ for frequency $f = 343\,\mathrm{Hz}$ . . . 57
Figure 57: Velocity profiles at $x/c = 0.77$ for frequency $f = 343\,\mathrm{Hz}$ . . . 58
Figure 58: Velocity profiles at $x/c = 0.95$ for frequency $f = 343\,\mathrm{Hz}$ . . . 58
Figure 59: Velocity profiles at $x/c = 1.2$ for frequency $f = 227\,\mathrm{Hz}$ . . . 59

List of Tables

Table 1: Physical properties 11
Table 2: Mesh quality parameters 13

List of Symbols

c	chord length
c_s	speed of sound
f	frequency
f'	forcing
k	turbulent kinetic energy
k_h	roughness element height
l_s	characteristic length
p	pressure
p_∞	free flow pressure
q	snapshot
u	velocity
u_∞	free flow velocity
u^*	friction velocity
t	time
CFL	Courant-Friedrichs-Lewy-number
C_s	Smagorinsky Coefficient
$\overline{C}_s$	quadratic Smagorinsky Coefficient
L	characteristic length
L_z	spanwise length
L_{ij}	test-window stress tensor
Ma	Mach number
N	number of cells
N_b	number of blocks
N_{crit}	critical amplitude factor
N_f	number of snapshots
Q	data matrix
Re	Reynolds number
T	temperature
S	spectral stress tensor
$\tilde{S}_{ij}$	filtered rate of strain
T_{ij}	subtest-scale stress tensor
W	weight
y^+	dimensionless wall distance
y_n	normal wall distance
α	angle of attack
δ^*	displacement thickness
δ	Kronecker delta
η	dynamic viscosity
ν	kinematic viscosity
ν_e	eddy viscosity

ν_t	subgrid-scale viscosity
ν_{eff}	effective viscosity
ϱ	density
τ_w	wall shear stress
τ_{ij}	Reynolds stress tensor
τ^R	residual stress tensor
τ^r	anistropic residual stress tensor
Δ	grid width
$\tilde{\Delta}$	test grid width
Λ	eigenvalue matrix
Ψ	eigenvector matrix
Θ	eigenvector matrix

List of Acronyms

CFD Computational fluid dynamics

LES Large-eddy simulation

PISO Pressure-Implicit with Split-ting Operators

PSD Power spectral density

RANS Reynolds-averaged Navier-Stokes equation

SIMPLE Semi-Implicit Method for Pressure Linked Equations

SPOD Spectral proper orthogonal decomposition

1 Introduction

In the last couple of years climate change received increasing interest in society and among governments, as it is going to affect every single person on earth. As power generation is a strong contributor to the production of greenhouse gases, the development of alternative technology is necessary to reduce the emission of greenhouse gas. Promising technologies have been developed to increase the amount of energy from renewable resources. A rather old technology, the wind turbine, has been optimized for many years, but unfortunately there are still problems in the operation of wind turbines, where one of the issues is noise production. Pressure fluctuations emerge from the rotor blades and lead to noise, which can result in serious health issues and effects everyday life [WHS15, p. 1]. Because of the noise level emitted by the plant, it has to be located in distance to inhabited areas. Therefore the possible locations for wind turbines are limited especially in dense areas. Reduction of the noise level would expand the possible locations for new wind energy plants and increase the acceptance in local communities.

To tackle the problem of noise emission and to develop strategies dealing with it, profound knowledge about the mechanisms involved in the generation of the pressure fluctuations is needed and modeling approaches for the arising structures are of interest.

Sound production in flows can have several origins. One of them is turbulence, i.e. unsteady fluctuations, that involves fluid-body interaction near walls [Bla17, p. 3]. At high Reynolds numbers the boundary layer near the trailing edge is usually turbulent, which leads to interaction between the turbulent boundary layer and the edge. The noise emitted is called trailing-edge noise. For low angles of attack trailing-edge noise acts as a dominant force of sound generation [LL04].

One characteristic property of turbulence is its unsteady chaotic behavior, which makes analysis and modeling of turbulent flows a complex task. Hence special tools are needed. Besides instability mechanism in turbulence can produce coherent structures of large scale, which are high energetic and are important if control of the flow is targeted.

In this thesis various tools are used to examine the behavior of the boundary layer around the airfoil and the evolving coherent structures in it.

The investigated case in this thesis has a high Reynolds number $Re = 295,000$ and a low angle of attack $\alpha = 9$. Therefore a pressure gradient on the suction side of the airfoil is present, which promotes the development of Kelvin-Helmholtz instabilities. Kelvin-Helmholtz modes are caused by the shear at the interface of a low and high velocity flow and represent the coherent structures, which are of high interest in this work.

First of all a three-dimensional large-eddy simulation (LES) is conducted, which solves a filtered version of the Navier-Stokes equations. Thereby temporal well resolved data of the investigated configuration is recorded with a moderate effort of computational cost. Other prominent approaches in computational fluid dynamics (CFD) are direct numerical simulation (DNS) and Reynolds-averaged Navier-Stokes equations (RANS). As DNS solves all scales included in the flow, the computational effort is too big for high Reynolds numbers. In contrast RANS models turbulence as a whole, which is very efficient, but is considered less

accurate and reliable than LES [WHS15, p .90]. To get an accurate representation of the mechanisms in the flow, LES is the method of choice. Afterwards experimental data as well as results by *XFoil*, a calculation tool for airfoils, serve as a reference for validation. In addition general flow features are presented.

At the next step the results of the LES are examined by utilization of spectral proper orthogonal decomposition (SPOD). The data is separated into modes, which are ranked by their contribution to the energy in the flow. Thereby dominant structures in the flow, which are dependent on space and time, can be detected despite the complex behavior of the flow field.

Furthermore resolvent analysis is tested for the configuration. Resolvent analysis is a hybrid approach, i.e. data-driven simulation, of reduced-order modeling using the mean flow of a system and a modified version of the Navier-Stokes equations. The method computes forcings and corresponding responses, which are velocity and pressure fluctuations, of the flow field in an optimal way, so that the forcings that give rise to the highest responses are found. In addition the resolvent method is combined with an eddy-viscosity approach. A total eddy-viscosity is introduced, which contains the molecular viscosity, the subgrid viscosity from the LES and the eddy-viscosity by the Reynolds stresses.

In the end of the thesis the modes obtained from SPOD applied to the LES data are compared to the results of the resolvent-based modeling approach. Therefore it is investigated, if instability mechanisms present in the computed LES are also detected by the resolvent and if it is capable of representing the coherent structures, which evolve in the turbulent boundary layer caused by the high pressure gradient of the setup.

The exact structure of the following work is outlined here. In the next chapter the main mathematical methods of LES, SPOD and resolvent analysis are introduced. Afterwards the setup of the LES to attain the data for subsequent analysis is described. Furthermore the setup of the resolvent-based modeling is explained. Then the results of the LES data are presented. On the next step SPOD is performed on the LES data and coherent structures are analyzed. Thereafter resolvent analysis is executed followed by the comparison of the modes resulting from SPOD and resolvent analysis. In the end the results are discussed and conclusions of the work are drawn.

2 Governing Equations

In this chapter the main mathematical methods used in this thesis are explained. At first the LES procedure is introduced and it is stated, how models are applied in it. Furthermore SPOD, a method which is able to detect dominant structures in the flow data, and resolvent analysis, a physics driven reduced-order modeling approach, are described.

2.1 Large-Eddy Simulation

2.1.1 General

Governing equations for the motion of fluids are the Navier-Stokes equations. For incompressible flows without any sources the Navier-Stokes equations are represented by the equation for conservation of mass

$$\frac{\partial u_i}{\partial x_i} = 0 \tag{1}$$

and conservation of momentum [Pop00, p. 15, 17]

$$\frac{\partial u_i}{\partial t} + \frac{\partial u_i u_j}{\partial x_j} = -\frac{1}{\varrho}\frac{\partial \tilde{p}}{\partial x_i} + \nu \frac{\partial^2 u_i}{\partial x_j^2}. \tag{2}$$

Solving the Navier-Stokes equations for all scales of the flow is linked to a huge computational effort and mostly not feasible for high Reynolds numbers considering the speed of central processing units in computers. In LES, energy carrying large scales are resolved and the effect of small scales is modeled. This is motivated by the knowledge that small, dissipative scales are expected to be isotropic and thus can be represented by simple models in contrast to the anisotropic large scale motions. As the resolution of small structures increases the amount of grid points and minimizes the necessary time step in the simulation, the computational cost can be heavily reduced. Nevertheless the unsteady solution still is expected to be accurate [WHS15, p. 90].

The Navier-Stokes equations are modified by applying a low-pass spatial filter with a filter function G and a filter width Δ. The operation is done by convolution [Pop00, p. 561]

$$\tilde{\boldsymbol{u}}(\boldsymbol{x}, t) = G * \boldsymbol{u} = \int G(\boldsymbol{r}, \boldsymbol{x}) \boldsymbol{u}(\boldsymbol{x} - \boldsymbol{r}, t) d\boldsymbol{r}. \tag{3}$$

The relevant quantities can be distinguished with $\boldsymbol{u} = \tilde{\boldsymbol{u}} + \boldsymbol{u''}$ in a filtered component $\tilde{\boldsymbol{u}}$ and a residual or subgrid-scale component $\boldsymbol{u''}$. Figure 1 shows an example for the filtering procedure.

The filtered Navier-Stokes equations are

$$\frac{\partial \tilde{u}_i}{\partial x_i} = 0 \tag{4}$$

and

$$\frac{\partial \tilde{u}_i}{\partial t} + \frac{\partial \widetilde{u_i u_j}}{\partial x_j} = -\frac{1}{\varrho}\frac{\partial \tilde{p}}{\partial x_i} + \nu \frac{\partial^2 \tilde{u}_i}{\partial x_j^2}. \tag{5}$$

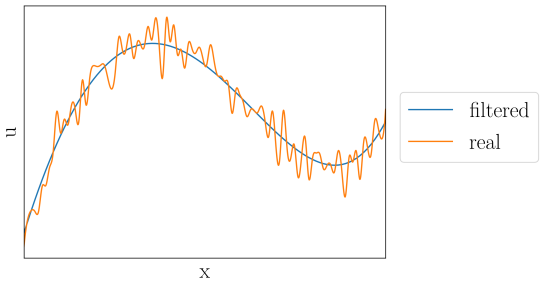

Figure 1: Filtering process

Through the filter operation a closure problem occurs, as the term $\widetilde{u_i u_j}$ yields new quantities. To resolve this problem the filtered Navier-Stokes equations are adapted with a new residual stress tensor also called subgrid-scale tensor [Pop00, p. 581]

$$\tau_{ij}^R = \widetilde{u_i u_j} - \widetilde{u}_i \widetilde{u}_j. \tag{6}$$

The anisotropic part of the residual stress tensor is needed

$$\tau_{ij}^r = \tau_{ij}^R - \frac{1}{3}\delta_{ij}\tau_{ll}^R \tag{7}$$

for the modeling procedure. The next step is to adjust the filtered pressure $\hat{p} = \tilde{p} + \frac{1}{3}\varrho\tau_{ll}^R$ with the isotropic part of the residual stress tensor. Finally the filtered momentum equation is provided by [Pop00, p. 582]

$$\frac{\partial \tilde{u}_i}{\partial t} + \frac{\partial \widetilde{u}_i \widetilde{u}_j}{\partial x_j} = -\frac{1}{\varrho}\frac{\partial \hat{p}}{\partial x_i} + \nu\frac{\partial^2 \tilde{u}_i}{\partial x_j^2} - \frac{\partial \tau_{ij}^r}{\partial x_j}. \tag{8}$$

The equations of mass and momentum keep the same form as in the previously introduced Navier-Stokes equations (Eq.: 8) but with filtered entities and added by a new term, the anisotropic residual stress tensor τ_{ij}^r. In the residual stress tensor τ_{ij}^r the unclosed terms are gathered and it includes the interaction between resolved and unresolved scales.

2.1.2 Dynamic Smagorinsky model

To solve the closure problem the anisotropic residual stress tensor τ_{ij}^r needs to be modeled. Importantly the model has to account for the dissipative behavior of the small unresolved eddies. Several models exist and the development of accurate and efficient models is still a current research topic. A model which was found to be widely used for flows around airfoils, for example by Wolf [Wol11] and Kitsios [Kit10], is the dynamic Smagorinsky model. It was firstly introduced by Germano [Ger+91] and modified by Lilly [Lil92]. Further the dynamic Smagorinsky model is going to be introduced and its advantages are explained.

For the group of Smagorinsky models in the beginning an eddy-viscosity model is utilized to substitute the anisotropic residual stress tensor[Pop00, p. 587]

$$\tau_{ij}^{r} = -2\nu_t \tilde{S}_{ij} \tag{9}$$

with an eddy viscosity ν_t and the filtered rate of strain $\tilde{S}_{ij} = \frac{1}{2}(\frac{\partial \tilde{u}_i}{\partial x_j} + \frac{\partial \tilde{u}_j}{\partial x_i})$. This is motivated by the assumption that the energy transfer mechanism from resolved to unresolved scales behaves like a molecular mechanism, i.e. molecular diffusion [Sag02, p. 93]. This procedure is also called Boussinesq hypothesis [Pop00, p. 93]. The next step is to model the eddy viscosity ν_t also called subgrid-scale viscosity. The mixing-length hypothesis, describing the turbulence as dependent on a characteristic length l_s and a characteristic velocity, results in

$$\nu_t = l_s^2 |\tilde{S}| = (C_s \Delta)^2 |\tilde{S}|, \tag{10}$$

where C_s is the Smagorinsky coefficient. The approach yields an isotropic value for the eddy viscosity at every point and for every time in the field. The original Smagorinsky model assumes the Smagorinsky coefficient as a constant over the whole domain, which bears problems. As studies showed different optimum values for different type of flows, like isotropic homogeneous turbulence or a channel flow, exist[Ger+91]. In addition the value of C_s should decrease near walls to reduce dissipation induced by the residual stress tensor in this area. The dynamic version of the Smagorinsky model tries to overcome these issues. It calculates the Smagorinsky coefficient locally, so that the Smagorinsky coefficient becomes $C_s = C_s(x, y, z, t)$ dependent on space and time. This is achieved by applying a second filtering to the Navier-Stokes equations and extrapolation of the resolved turbulent structures. Afterwards the new local Smagorinsky coefficient needs to provide a consistent solution for the residual stress tensor, resulting from the original filter operation, and the subtest-scale stress tensor, resulting from the new test-filter operation, at the same time.

First of all the already filtered Navier-Stokes equations (Equation (5)) are filtered with a coarser test filter $\hat{\tilde{\Delta}}$

$$\frac{\partial \hat{\tilde{u}}_i}{\partial t} + \frac{\partial \hat{\tilde{u}}_i \hat{\tilde{u}}_j}{\partial x_j} = -\frac{1}{\varrho}\frac{\partial \hat{\tilde{p}}}{\partial x_i} + \nu \frac{\partial^2 \hat{\tilde{u}}_i}{\partial x_j^2} - \frac{\partial T_{ij}}{\partial x_j}. \tag{11}$$

A new subtest-scale stress tensor $T_{ij} = \widehat{\widetilde{u_i u_j}} - \hat{\tilde{u}}_i \hat{\tilde{u}}_j$ is generated by adapting the equation as before in Equation (5). Next the Smagorinsky closure is applied to T_{ij}

$$T_{ij} - \frac{1}{3}\delta_{ij} T_{ll} = 2\overline{C}_s \hat{\Delta}^2 |\hat{\tilde{S}}| \hat{\tilde{S}}_{ij}. \tag{12}$$

Now the quadratic Smagorinsky coefficient $\overline{C}_s = (C_s)^2$ is examined. Note that this also allows negative values for C_s. Further the test-window L_{ij} is composed of the test stress tensor T_{ij} and the test-filtered subgrid-scale stress tensor $\widehat{\tau_{ij}^R}$

$$L_{ij} = T_{ij} - \widehat{\tau_{ij}^R} = -\widehat{\tilde{u}_i \tilde{u}_j} + \hat{\tilde{u}}_i \, \hat{\tilde{u}}_j. \tag{13}$$

Equation (13) is called the Germano identity. The test window L_{ij} is the resolved turbulent stress, which represents the small resolved scales between test filter width $\hat{\tilde{\Delta}}$ and filter width Δ. After applying the Smagorinsky closure to the test-window, it can be compared locally

$$L_{ij} - \frac{1}{3}\delta_{ij}L_{ll} = 2\overline{C}_s M_{ij}, \tag{14}$$

where

$$M_{ij} = (\tilde{\Delta}^2|\hat{\tilde{S}}|\hat{\tilde{S}}_{ij} - \Delta^2|\widehat{\tilde{S}|\tilde{S}_{ij}}). \tag{15}$$

Five independent components are described by Equation 14, so $\overline{C}_s$ can not be calculated directly. Instead the mean-square error is minimized by

$$\overline{C}_s = \frac{1}{2}(\frac{L_{ij}M_{ij}}{M_{ij}M_{ij}}). \tag{16}$$

Now the Smagorinsky coefficients are adjusted locally to the state of the flow. One drawback of the model is the tendency to produce high negative Smagorinsky coefficients. To prevent nonphysical behavior, the numerical scheme clips negative eddy viscosity, so that the effective viscosity $\nu_{eff} = \nu + \nu_t$ does not become negative. Besides the Smagorinsky coefficients are averaged locally over cell faces to prevent high values. Instead of local averaging other methods like averaging of the Smagorinsky coefficient over a homogeneous direction or in direction of particle trajectories are possible. The latter is called dynamic Lagrangian Smagorinsky model and was introduced by Meneveau [MLC94]. This model will also be tested during the simulation phase. But because the final simulation runs with the dynamic Smagorinsky model, the dynamic Lagrangian model is not explained here in detail. As mentioned above C_s can become negative. This effect is also called backscatter, where small eddies transfer energy to larger scales [OBR06, p. 257]. The constant Smagorinsky model can not account for this phenomenon, which is another negative aspect of the constant approach. But in comparison to the constant Smagorinsky model, the better performance of the dynamic models imposes a higher computational cost by solving Equation (16). Eventually not every issue of the Smagorinsky model approach is corrected by the dynamic modeling. Near walls problems still arise with these models. The Smagorinsky coefficient changes at walls in a favourable way by declining to $C_s = 0$ accordingly to the length scale at the wall. But complex near-wall dynamics can not be captured by the Smagorinsky model and therefore need to be resolved properly or modeled with extra wall models [Sag02, p. 280].

2.2 Spectral Proper Orthogonal Decomposition

The detection of dominant structures in the flow is a crucial aspect of the analysis. Given the highly unsteady and chaotic behavior of turbulent flows, the method for investigation needs to handle this aspects. To extract relevant structures SPOD as introduced by Towne et al. [TSC18] is utilized and explained analogous. The procedure decomposes the flow field into modes which are associated to a frequency and ranked by their contribution to the energy in the flow. Thereby dominant structures and their frequency can be determined.

Spectral proper orthogonal decomposition is a modification of the original proper orthogonal decomposition (POD). It has the advantage to represent structures as modes dependent on space and time over only spatially coherent modes in the POD [TSC18]. Given that tur-

bulence is highly dependent of both, space and time, SPOD is the proper tool of choice for further investigations.

The procedure of POD is described shortly as a starting point for the explanation of the SPOD. The goal of POD is to find a function $\boldsymbol{\Phi}(z)$ on a domain which on average approximates the data $\boldsymbol{q}$(z) best. First of all mean-centered data is considered, i.e. in fluid dynamics the fluctuations are observed. The search for the best-approximation function results in an eigenvalue problem, where the obtained eigenvectors $\boldsymbol{\Phi}(z)$ build a set of orthogonal basis functions or modes of the data [TSC18]

$$\boldsymbol{q}(z) = \sum_{j=1}^{\infty} a_j \boldsymbol{\Phi}_k(z), \tag{17}$$

which are ranked by their associated eigenvalue. The eigenvector $\boldsymbol{\Phi}_k(z)$ corresponding to the highest eigenvalue then is on average the best fit to the data. In terms of fluid dynamics the eigenvalue also shows the amount of energy a mode contributes to the flow, so that the structures containing the most energy are represented by the eigenvectors $\boldsymbol{\Phi}_k(z)$ corresponding to the highest eigenvalues. The approach is a reduced-order modeling method in the sense that usually just a few of the highest ranked modes are already a good approximation for the original data.

For SPOD this procedure is expanded to space and time dependent modes by transferring the process of optimization into the frequency domain. To find the SPOD modes, which contain the most energy, the eigenvalue problem [TSC18]

$$\int_{\Omega} \boldsymbol{S}(\boldsymbol{x}, \boldsymbol{x}', f')\boldsymbol{W}(\boldsymbol{x}')\boldsymbol{\Psi}(\boldsymbol{x}', f')d\boldsymbol{x}' = \lambda(f')\boldsymbol{\Psi}(\boldsymbol{x}, f') \tag{18}$$

with the cross-spectral density tensor $\boldsymbol{S}$, the eigenmode $\boldsymbol{\Psi}$ with corresponding eigenvalue λ, any frequency f' and the weight $\boldsymbol{W}$ needs to be solved. Furthermore the method is described for discrete data. At first the data matrix with M time steps and N spatial points

$$\boldsymbol{Q} = [\boldsymbol{q}_1, \boldsymbol{q}_2, ..., \boldsymbol{q}_M] \in \mathbb{R}^{\mathrm{NxM}}, \tag{19}$$

consisting of the snapshots $\boldsymbol{q}_k$, i.e. the flow field at a specific time step k, is constructed. Transformation into the frequency domain is then done by Welch's method [Wel67] to get converged estimates of the spectral densities. Therefore the data matrix $\boldsymbol{Q}$ is split in N_b overlapping blocks and discrete Fourier-transformation is computed for every block

$$\hat{\boldsymbol{Q}}^{(n)} = [\hat{\boldsymbol{q}}_1^{(n)}, \hat{\boldsymbol{q}}_2^{(n)}, ..., \hat{\boldsymbol{q}}_{N_f}^{(n)}] \in \mathbb{R}^{\mathrm{NxN_f}} \tag{20}$$

with N_f snapshots. Afterwards averaging the results for one frequency over all blocks yields the converged estimate. The discrete cross-spectral density tensor of frequency f_k is then obtained by [TSC18]

$$\boldsymbol{S}_{f_k} = \hat{\boldsymbol{Q}}_{f_k}\hat{\boldsymbol{Q}}_{f_k}^{*} \tag{21}$$

with

$$\hat{\boldsymbol{Q}}_{f_k} = \sqrt{\frac{\Delta t}{(sN_b)}}\,[\hat{\boldsymbol{q}}_k^{(1)}, \hat{\boldsymbol{q}}_k^{(2)}, ..., \hat{\boldsymbol{q}}_k^{(N_b)}] \in \mathbb{R}^{\mathrm{NxN_b}}, \tag{22}$$

so that the Fourier coefficients at frequency f_k from each block are gathered and averaged in the process. Finally the $N \times N$ eigenvalue problem [TSC18]

$$\boldsymbol{S}_{f_k} \boldsymbol{W} \boldsymbol{\Psi}_{f_k} = \boldsymbol{\Psi}_{f_k} \boldsymbol{\Lambda}_{f_k}, \tag{23}$$

where $\boldsymbol{\Lambda}_{f_k}$ contains the eigenvalues, can be solved for each frequency. A more efficient way corresponding to the same non-zero eigenvalues is given by the $N_b \times N_b$ eigenvalue problem [TSC18]

$$\hat{\boldsymbol{Q}}_{f_k}^{*} \boldsymbol{W} \hat{\boldsymbol{Q}}_{f_k} \boldsymbol{\Theta}_{f_k} = \boldsymbol{\Theta}_{f_k} \tilde{\boldsymbol{\Lambda}}_{f_k}. \tag{24}$$

From this the eigenvector $\boldsymbol{\Psi}_{f_k}$ can be reproduced. The eigenvectors $\boldsymbol{\Psi}_{f_k}$ at one frequency are ranked by their corresponding eigenvalues, thereby the structures containing the highest amount of energy at a specific frequency f_k are determined. This knowledge gives deeper insight in the propagation of eddies and instabilities in the turbulent flow. But, as the procedure only assumes harmonic oscillations and turbulent flow is not strictly harmonic by nature, there still exists some discrepancy between the tool and the data.

2.3 Resolvent Analysis

The resolvent method is a reduced-order modeling procedure rooting in control theory [MS13]. It is a hybrid approach as experimental or numerical data is used to solve a modified version of the Navier-Stokes equations. Only the mean flow has to be known to calculate the response of the system at a specific frequency. In order to control the behavior of the flow, knowledge about actuation frequencies, which are affecting the system the most, are precious to design effective, low effort approaches.

In the beginning Navier-Stokes equations are divided in a linear and nonlinear part and represented in the frequency domain. A transfer function, i.e. the resolvent operator, connects the nonlinear terms of the Navier-Stokes equations with response modes. Then the linear resolvent operator can be examined by singular value decomposition(SVD) to find optimal choices of inputs, i. e. the nonlinear terms, and corresponding outputs, the velocity and pressure response modes. The benefit of this method lies in the treatment of the nonlinear terms. Modeling the nonlinear interaction in a simple and correct way is a difficult task, as the whole range of scales needs to be considered. Resolvent method handles these terms by treating them as an unstructured forcing, which does not require modeling. The actual form of the nonlinear terms is not relevant to the system because of its selective behavior[MS13].

At first the Navier-Stokes equations for incompressible flows are considered [Mor+19]

$$\frac{\partial u_i}{\partial t} + \frac{\partial u_i u_j}{\partial x_j} + \frac{1}{\varrho}\frac{\partial p}{\partial x_i} = \nu \frac{\partial^2 u_i}{\partial x_j^2}, \tag{25}$$

$$\frac{\partial u_i}{\partial x_i} = 0. \tag{26}$$

Next Reynolds decomposition is applied by splitting the entities into $u_i = \overline{u}_i + u_i'$ with the mean value $\overline{u}_i$ and the fluctation u_i' as the first step. Inserting the Reynolds decomposition in Equation (26) and subtracting the averaged Navier-Stokes equations yields

$$\frac{\partial u_i'}{\partial t} + \frac{\partial \overline{u}_i u_j'}{\partial x_j} + \frac{\partial u_i' \overline{u}_j}{\partial x_j} + \frac{\partial p'}{\partial x_i} - \nu_{tot}\frac{\partial^2 u_i'}{\partial x_j^2} = -\frac{\partial u_i' u_j'}{\partial x_j} + \overline{\frac{\partial u_i' u_j'}{\partial x_j}}, \tag{27}$$

$$\frac{\partial u_i'}{\partial x_i} = 0. \tag{28}$$

In addition the pressure p' will include the division by density ϱ in the subsequent description.

Importantly in this step a new entity, the total viscosity ν_{tot}, is integrated into the resolvent approach. The introduction of this new parameter instead of the original molecular viscosity ν led to improved results for the system for example by Morra [Mor+19]. It accounts mainly for the influence of turbulent stresses. Primarily eddy-viscosity modeling was done by Reynolds and Hussain [RH71]. Here ν_{tot} is composed of molecular viscosity ν, eddy viscosity ν_e and subgrid-scale viscosity ν_t as done by [Kai+19]

$$\nu_{tot} = \nu + \nu_e + \nu_t. \tag{29}$$

The eddy viscosity ν_e is approximated with the Boussinesq approach by calculating [Kai+19]

$$\nu_e = \frac{(-\overline{u_i' u_j'} + \frac{2}{3}k\delta_{ij}) \cdot (\frac{\partial \overline{u}_j}{\partial x_i} + \frac{\partial \overline{u}_i}{\partial x_j})}{(\frac{\partial \overline{u}_j}{\partial x_i} + \frac{\partial \overline{u}_i}{\partial x_j} \cdot \frac{\partial \overline{u}_j}{\partial x_i} + \frac{\partial \overline{u}_i}{\partial x_j})}, \tag{30}$$

where k is the turbulent kinetic energy. With the least mean squares method a solution of the six independent equations for the eddy-viscosity ν_e is determined. Moreover to the total viscosity ν_{tot} the subgrid-scale viscosity ν_t from the LES is also added.

On the left hand side of Equation (27) the linear terms are gathered. The nonlinear terms on the right hand side can be merged to

$$-\frac{\partial u_i' u_j'}{\partial x_j} + \overline{\frac{\partial u_i' u_j'}{\partial x_j}} = \boldsymbol{f'}. \tag{31}$$

The new entity $\boldsymbol{f'}$ is called the forcing. For further analysis the frequency domain is

considered and the fluctuations and the forcing are Fourier transformed

$$\boldsymbol{u'} = \int_{-\infty}^{\infty} \hat{\boldsymbol{u}}(\omega) e^{-i\omega t} d\omega \tag{32}$$

$$\boldsymbol{f'} = \int_{-\infty}^{\infty} \hat{\boldsymbol{f}}(\omega) e^{-i\omega t} d\omega \tag{33}$$

with a real frequency ω. Rearranging Equation (27) and (28) in the frequency domain yields [Wag+19]

$$\begin{bmatrix} \hat{\boldsymbol{u}}(\omega) \\ \hat{p}(\omega) \end{bmatrix} = (-i\omega \begin{bmatrix} \boldsymbol{I} & \\ & 0 \end{bmatrix} - \mathcal{L})^{-1} \begin{bmatrix} \boldsymbol{I} \\ 0 \end{bmatrix} \hat{\boldsymbol{f}}(\omega). \tag{34}$$

The linear Navier-Stokes operator $\mathcal{L}$ is given by

$$\mathcal{L} = \begin{pmatrix} -\overline{\boldsymbol{u}} \cdot \nabla() - () \cdot \nabla \overline{\boldsymbol{u}} + \nu_{tot} \nabla^2() & -\nabla() \\ \nabla \cdot () & 0 \end{pmatrix} \tag{35}$$

and contains the mean velocity field. Further simplification of Equation (34) with the new resolvent operator

$$\mathcal{H}(\omega) = (-i\omega \begin{bmatrix} \boldsymbol{I} & \\ & 0 \end{bmatrix} - \mathcal{L})^{-1} \tag{36}$$

becomes

$$\begin{bmatrix} \hat{\boldsymbol{u}}(\omega) \\ \hat{p}(\omega) \end{bmatrix} = \mathcal{H}(\omega) \begin{bmatrix} \boldsymbol{I} \\ 0 \end{bmatrix} \hat{\boldsymbol{f}}(\omega). \tag{37}$$

The linear transfer function $\mathcal{H}(\omega)$ connects the forcing with the output, the velocity and pressure response modes. To construct the resolvent operator $\mathcal{H}$ only the mean velocity field and a frequency is needed. The next step is to obtain solutions for the forcing which result in the highest responses. Therefore the energy norm of the system is considered. The optimization problem to find optimal choices of forcings and responses that maximize the amplification G is [Wag+19]

$$G(\omega) = \max_{\hat{f}} \frac{\hat{\boldsymbol{u}}^* Q_u \hat{\boldsymbol{u}}}{\hat{\boldsymbol{f}}^* Q_f \hat{\boldsymbol{f}}} \tag{38}$$

with matrices Q_u and Q_f from discretization and entities still assigned to a specific frequency $\hat{\boldsymbol{f}} = \hat{\boldsymbol{f}}(\omega)$.

This problem is solved numerically using the program *FeLiCS* by the department FLOW of TU Berlin, which discretizes the domain with the Finite Element Method project *Fenics* and exploits the eigenvalue problem by utilizing the *scipy* "scipy.sparse.linalg" module.

Now the eigenvector $\begin{bmatrix} \hat{\boldsymbol{u}}_k(\omega) \\ \hat{p}_k(\omega) \end{bmatrix}$ corresponding to the highest eigenvalue is the structure that represents the highest response of the system for each frequency ω. The forcing modes are also accessible and give information about the structure of inputs that are highly effective on the flow.

3 Numerical Setup

In this section the setup of the realized LES and resolvent simulation are presented. A wall-resolved three-dimensional LES with the open source software *OpenFOAM* is performed to analyze structures evolving in the boundary layer. At first physical properties of the setup and boundary conditions are described. Next the mesh and mesh quality are discussed followed by the solver settings. Afterwards the boundary layer tripping is explained. Aside from that the configuration of the resolvent analysis is defined. Therefore the total viscosity field in combination with a sponge layer is presented. Finally the mesh properties and the parameters for the mesh independence study of the resolvent simulation are included.

3.1 Large-Eddy Simulation

3.1.1 General

The examined airfoil is the "Clark-Y" profile with a blunt edge. The chord length c equals the one in the experimental setup with $c = 0.3\,\mathrm{m}$. The Reynolds number is set to a high value with $Re = 295,005$ at an angle of attack of $\alpha = 9°$. With a low mach number $Ma = \frac{u}{c_s}$ of $Ma \approx 0.04$ compressibility effects play a minor role in the flow and it is sufficient to assume it as incompressible. Moreover a constant temperature T in the flow is assumed. In Table 1 the physical properties of the flow are summarized.

Table 1: Physical properties

Entity	Symbol	Unit	Value
Density	ϱ	$\frac{kg}{m^3}$	1.193
Kinematic viscosity	ν	$\frac{m^2}{s}$	$1.5254 \cdot 10^{-5}$
Temperature	T	$°C$	20
Reynolds number	Re	-	295,005
Mach number	Ma	-	0.04

A LES of a whole blade would not be feasible with current resources, hence only a part of the blade is simulated. Since the flow is homogeneous in spanwise direction only a section of the span is considered in the simulation. The size of the whole domain is $[L_x \text{ x } L_y \text{ x } L_z] = [15c \text{ x } 10c \text{ x } 0.16c]$ with length L in streamwise direction x, transversal direction y and spanwise direction z. In spanwise direction symmetric boundary conditions are applied. Therefore the spanwise length L_z needs special attention in order to respect the flow characteristics, as the restriction of the domain could force the flow to unnatural behavior and large eddies could be "squeezed" [Frö+05]. But as the amount of computational effort rises with the size of the domain, L_z should be as low as possible without affecting the flow, so that the simulation is still on a feasible level. For this purpose a time correlation in spanwise direction can be performed to check if there is enough space for the larger scales to evolve [Kit10, p. 163]. By comparison with simulations at similar Reynolds numbers the spanwise length L_z is chosen. For this investigation it should also be noted that for higher Reynolds numbers the structures tend to reduce in size and a smaller L_z, considering the chord length

c, is acceptable [Kit10, p. 32]. Through literature research a value of $L_z = 0.16c$ seems to be a conservative choice as Wolf [Wol11] uses $L_z = 0.1c$ at $Re = 408,000$ with a higher Reynolds number and Yeh [YT19] $L_z = 0.2\,c$ at $Re = 23,000$ with a lower Reynolds number.

At the inflow constant Dirichlet boundary condition $\boldsymbol{u} = (15\ 0\ 0)\ \mathrm{m\,s^{-1}}$ is used and assigned all around the "C-surface" as well as at the top and bottom of the far-field. To guarantee no interference of the outflowing fluid with the inner domain, advective boundary condition is active at the outlet. As mentioned before symmetric boundary conditions are applied to the front and back of the simulation, i.e. spanwise direction, and at the blade "noSlip" is set. For the initial flow field of the final setup the simulation already ran more than $T = 0.1\,\mathrm{s}$ of physical time starting with a constant flow, so that the simulation is in a nearly "converged" turbulent state.

The filter operation applied to the Navier-Stokes equation is done implicitly by the grid width Δ and can be computed locally by $\Delta = (\Delta x \Delta y \Delta z)^{\frac{1}{3}}$. The modeling procedure of the residual stress tensor, which arises in the derivation of the filtered Navier-Stokes equations, is done by the dynamic Smagorinsky model introduced in Section 2.1.2. A test of the dynamic Lagrangian model also is conducted as well and shortly presented in Section 4.1.1.

3.1.2 Mesh

A "C-shaped" mesh is generated for the simulation using the meshing tool ICEM. Figure 2 and 3 illustrate the whole domain and the area near the airfoil. The mesh is structured in two parts, an outer and inner part, shown by the red and black lines in Figure 4. The inner part is resolved two times finer in spanwise direction as the outer part. The two refinement levels exist to lower aspect ratio in the far-field and more important reduce the computational effort. The total amount of cells is $N = 13,927,800$, consisting of $N_{hex} = 13,870,750$ hexahedron shaped cells and $N_{poly} = 57,050$ polyhedrons at the border between outer and inner region. Moreover the domain is divided in the inner region in spanwise direction by $N_z = 100$. Around the airfoil the mesh is discretized by $N_c = 608$.

Near wall motions of the flow are crucial for the result. The anisotropic behavior near walls can not be captured well by the subgrid-scale models of the Smagorinsky approach for LES [Sag02, p. 280]. In addition high gradients are present in the boundary layer. To describe physics near the wall appropriately, the near wall area is highly resolved and needs to fulfill requirements, i.e. special dimensionless wall distance values y^+ need to be satisfied. In Figure 6 the resolution of the mesh at the blunt trailing edge is shown, which is the most difficult area in the meshing process. A smooth transition at the edge is needed but also non-orthogonality and skewness of the cells have to be respected. On the suction side near the trailing edge non-orthogonal cells appear, it is noted that this is not the case over the whole suction side, but just in the area very close to trailing edge due to the curvature of the airfoil.

The dimensionless wall distance

$$y^+ = \frac{u^* y}{\nu}, \tag{39}$$

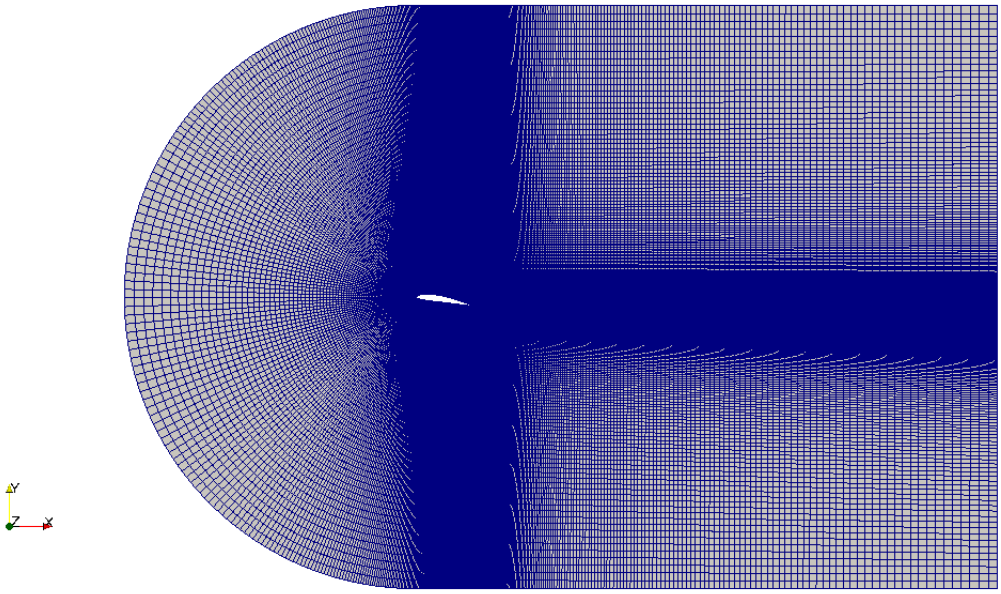

Figure 2: LES: Whole Mesh

where $u^* = \sqrt{\frac{\tau_w}{\varrho}}$ is the friction velocity with the wall shear stress τ_w and $y$the distance to the nearest wall is observed [WHS15, p. 106]. In the case of x- and z- direction the length of the cell at the wall for the according direction is used. Suggested values for a wall-resolved LES are $\Delta x^+ = 50 - 150$, $\Delta z^+ = 10 - 40$ and $\Delta y^+ < 1$ [WHS15, p. 209]. The y^+-values are shown in Figure 7 and are, except for the point right at the tip of the airfoil, below the critical value $y^+ = 1$. For the spanwise direction all cells have a dimensionless wall length of at least $z^+ < 32$ and in streamwise direction $x^+ < 80$ with most of the cells containing lower values. As all dimensionless wall distance values meet the provided specifications, the boundary should be resolved enough to produce accurate results.

In addition the quality of the mesh is shown regarding skewness, non-orthogonality and apect ratio in Table 2. Highest aspect ratios exist in the far-field, where gradients of the flow entities are low and therefore are not of high interest. The issue of non-orthogonality, which occurs especially in the "C-shaped" region, is addressed in the solver by employing a non-orthogonal corrector. Finally maximum skewness is still in acceptable range.

Table 2: Mesh quality parameters

Parameter	**Value**
Max. non-orthogonality	31
Average non-orthogonality	5.6
Max. skewness	0.51
Max. aspect ratio	313

3.1.3 Solver

Incompressible Navier-Stokes equations are discretized by finite volume method. The solver used in the simulation is the PIMPLE algorithm which is a mixture of the SIMPLE (Semi-

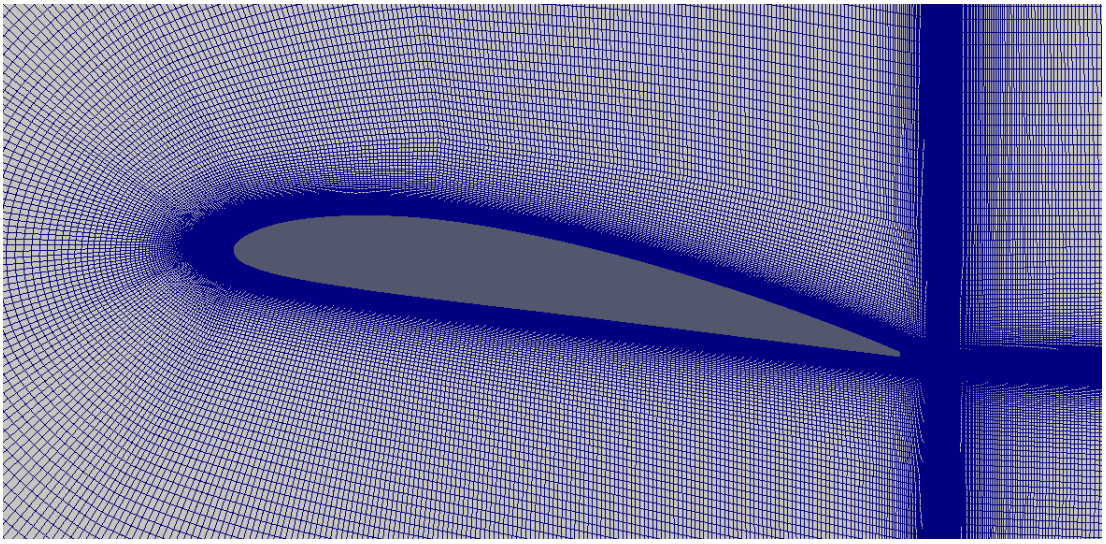

Figure 3: LES: Mesh around the airfoil

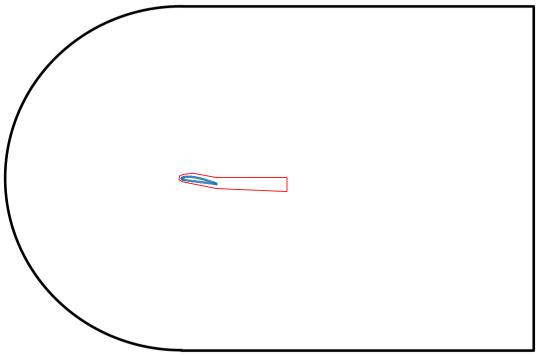

Figure 4: Refinement levels

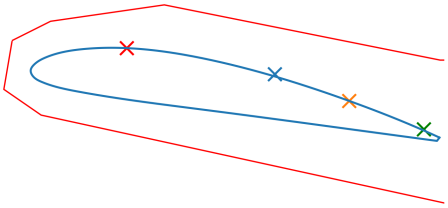

Figure 5: Probe locations and refinement

Implicit Method for Pressure Linked Equations) and the PISO (Pressure-Implicit with Splitting Operators) algorithm. The SIMPLE algorithm is a pressure correction method for steady cases where a pressure is at first estimated to solve the Navier-Stokes equation and later corrected. PISO algorithm is also a pressure correction method but for transient problems [Jas96, p. 147-149]. The amount of PISO-corrector steps is set to two, whereas one is a non-orthogonal corrector dealing with the error caused by non-orthogonal cells in the mesh. The PISO-correctors are calculated for every cycle of the seven outer loops. During one time step velocity and pressure are solved several times until convergence is reached. Exact configuration of the solver can be found in the appendix via the *fvSolution*-file.

The time step is set to $\Delta t = 2.2 \cdot 10^{-6}$ s. The maximum CFL-number $CFL = \frac{u \cdot \Delta x}{\Delta t}$ reached during the simulation is $CFL_{max} < 2$. It still provides a stable simulation as an implicit time scheme is used and the highest CFL-numbers are only found in some cells of the well resolved

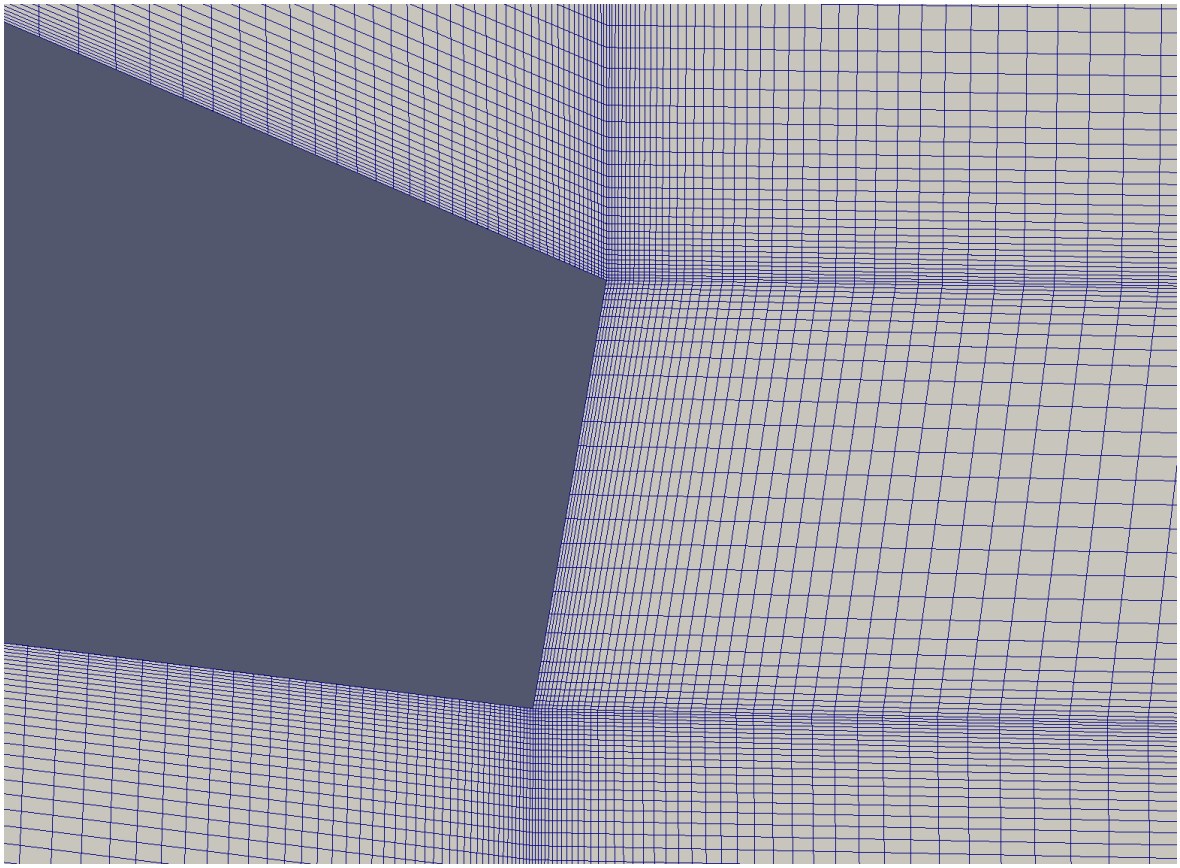

Figure 6: Near wall resolution at the trailing edge

boundary layer. The time scheme is the backward time scheme and of second order

$$\frac{\partial \phi}{\partial t} = \frac{1}{\Delta t}(\frac{3}{2}\phi - 2\phi^{o} + \frac{1}{2}\phi^{oo}), \tag{40}$$

where the flow entity ϕ with the index o is the state at the last time step.

The spatial numerical schemes are all of second order to achieve the necessary accuracy and appended in the *fvSchemes*-file. With GAMG a multigrid solver is used to compute the pressure equation.

3.1.4 Boundary layer tripping

As wind turbines are located outside in the range of atmospheric boundary layer, most of the time turbulent flow is surrounding them. In the experiment the airfoil possesses a surface of high roughness. Fluctuations in the flow or a rough surface induce earlier transition at a wall but the inflow of the simulation is set to be constant. Also there is no roughness present at the airfoil's surface. To simulate the behavior of the flow analogous for the blade of the wind turbine or the setup in the experiment, a tripping element is introduced to force an earlier start of transition. For this a roughness element is chosen and the location and height of this element needs to be determined. From experimental data the location of transition is not accessible. To identify the location of the trip and accordingly the point of transition,

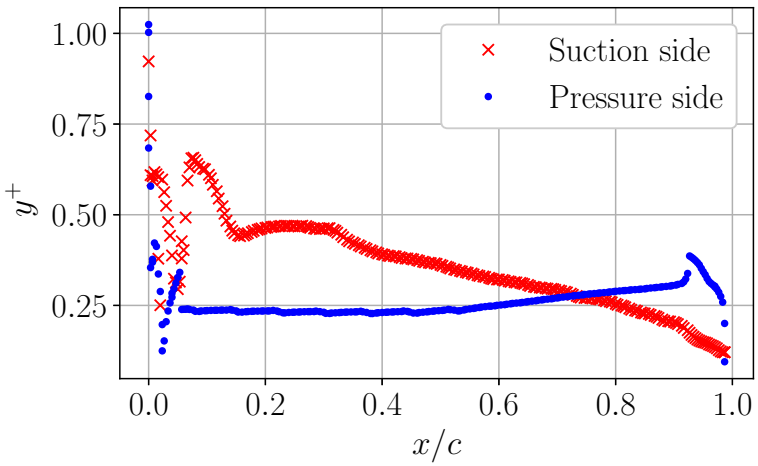

Figure 7: y^+-values

XFoil [Dre89] is used. It utilizes the e^N-method, where transition is triggered, when e^N-criterion, i. e. a specific amplitude factor, is met. The e^N-method evolved from linear stability theory and is precise if Tollmien-Schlichting waves are the dominant mechanism of transition. In flows with low turbulence intensities this is mostly true. But for the investigated configuration with an airfoil of significant roughness or high turbulence other instabilities could be dominant. A low value for the critical amplitude factor N_{crit} could mimic the behavior of this kind of flows as mentioned in [DY01], but relying only on this assumption would probably lead to a poor estimation. To get a accurate estimation of the location of transition, simulations with various critical amplitude factors N_{crit} are performed. Afterwards the pressure distribution of the *XFoil* results and the experimental data are compared. *XFoil* and the conducted comparison are also discussed in Section 4.1.1. With $N_{crit} = 1$ the best fit for the data occurs, which actually reflects the notion of early transition. The beginning of transition is located right after linear instabilities start to rise in the boundary layer. Free transition begins at $x/c = 0.034$ for the suction side, though transition is not triggered on the pressure side. At first a simulation with a roughness element on both sides at x/c=0.034 was executed because high roughness in the experiment could lead to transition on both sides. Nevertheless it resulted in a laminar pressure side as predicted by *XFoil*. Therefore the roughness element is only implemented on the suction side at $x/c = 0.034$. The height of the element k_h is computed like it is described in [Dry58] used as well by Boudet [BM15]. The ratio between the element height and the displacement thickness δ^* is $\frac{k_h}{\delta^*} = 0.92$ to excite transition immediately. The displacement thickness δ^* at the beginning of transition can be calculated by *XFoil* once again. Finally the height of the roughness element is $k_h = 0.92\delta^* = 0.92 \cdot 3.853 \cdot 10^{-4}\text{m} = 3.545 \cdot 10^{-4}\text{m}$. The length of the element is set to be one cell and it is realised by constraining the cells of the roughness element to zero velocity $\boldsymbol{u} = (0\ \ 0\ \ 0)\ \text{m}\,\text{s}^{-1}$ all over the span. The element on the airfoil is illustrated in Figure 8.

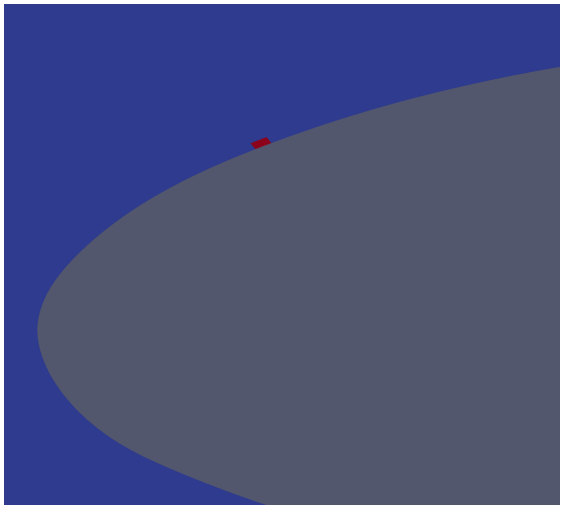

Figure 8: Boundary layer trip

3.1.5 Solution and simulation process

The simulation has a total of $T = 0.155\,76\,\mathrm{s}$ physical run-time with a sampling frequency $f_s = 4545.45\,\mathrm{Hz}$ resulting in 7080 snapshots. Computations were executed on Intel Xeon Platinum 8260 CPU using 40 and 80 cores during the simulation. One time step with 40 cores took $t_{40} \approx 20\,\mathrm{s}$ and one time step with 80 cores $t_{80} \approx 13\,\mathrm{s}$ of execution time. Consequently for 80 cores the number of cores already does not scale linear with the execution time per time step. The total time for the computation was about 25,000 h of one core running.

In the process of mesh generation several problems occurred as nonphysical disturbances in the flow field appeared. Different parts of the mesh were affected. One problem have been regions of high growth rate around the airfoil. Another location was at the “C-shaped inlet”. Wavelike perturbations started to propagate from the inlet even with a constant inflow. Presumably the cause of this disturbance was the non-orthogonality of the cells in this region. Because of the very small time step and therefore the large amount of computational steps needed, the small error by non-orthogonality in every time step sums up to a disturbance of the global flow field. Through further refinement and adjustment of cell distribution the mesh quality was improved. Besides the residual controls were raised to achieve a higher accuracy per time step. Another problem appeared at the transition between “C-shaped” inlet and the top and bottom planes in the far-field. At this intersection running also through the trailing edge an nonphysical rise in streamwise velocity was observed. Further refinement could reduce this problem to a level below $\Delta u < 1\%$. The final reason for this problem could not be found in the end.

3.2 Resolvent Analysis

Next the setup of the global two-dimensional resolvent analysis is explained. As the resolvent is a data-driven approach the necessary flow fields have to be provided as inputs. Therefore the results of the LES, which are described in the next section, serve as these inputs. The flow fields which are used for the calculation are the mean velocity components $\overline{u}$ and $\overline{v}$ (Figure 23) as well as the total viscosity ν_{tot}. In addition the flow fields are span-averaged to neglect effects in homogeneous direction and to get a more accurate mean value, as the duration of the LES is too short for converged statistics. The total viscosity ν_{tot} contains the molecular viscosity, the eddy viscosity from the Reynolds stresses and the subgrid-scale viscosity of the LES. The molecular viscosity for the setup is former $\nu = 1.5254 \cdot 10^{-5}\,\mathrm{m^2\,s^{-1}}$. In addition the time- and span-averaged subgrid-scale viscosity, shown in the coming Section 4.1.3, is used, which is obtained from the LES results. Furthermore the eddy-viscosity obtained from Equation (29) is also derived from the results of the LES. The Reynolds stresses utilized for this are presented in Figure 21 and are span-averaged results. Furthermore a sponge layer is applied to the total viscosity ν_{tot}. Resolvent analysis often struggles with perturbations at the far-field boundary. The use of the sponge layer in the far-field, so that the total viscosity rises to high a value of $\nu = 0.02\,\mathrm{m^2\,s^{-1}}$, should prevent perturbations at the far-field including inlet and outlet by the damping nature of a high viscosity. The sponge layer starts at a

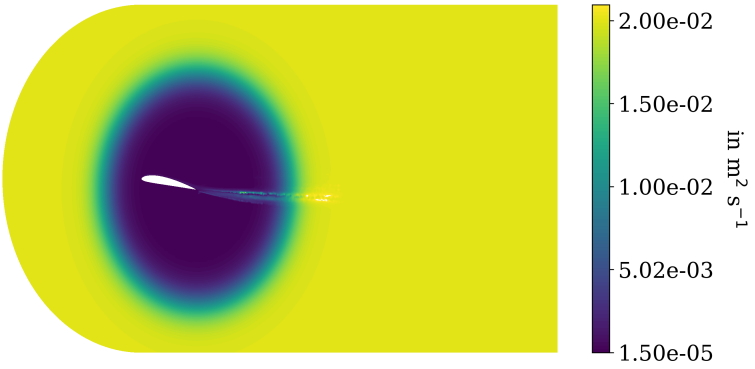

Figure 9: Total viscosity ν_{tot} with the sponge layer

radius of $r = 0.35\,\mathrm{m}$ circling the trailing edge of the airfoil and is realized by the hyperbolic tangent function to achieve a continuous transition to the far-field. The final total viscosity ν_{tot} with the applied sponge layer for the simulation is presented in Figure 9 and 10. The dominant source for the total viscosity is given by the eddy viscosity ν_e from the Reynolds stresses yielding values in the magnitude of $\approx 1 \cdot 10^{-3}\,\mathrm{m^2\,s^{-1}}$. In comparison molecular and subgrid-scale viscosity are of similar order of magnitude $\approx 1 \cdot 10^{-5}\,\mathrm{m^2\,s^{-1}}$. The viscosity is high in the boundary layer on the suction side and the wake. A line of low viscosity splits the wake due to the characteristics of the Reynolds stresses. In addition at the trailing edge viscosity is low on account of the recirculation zone in this area.

After the execution of SPOD on the LES data major frequencies of structures are found until $f = 1000\,\mathrm{Hz}$, so that the modes computed by resolvent are also covering the range of

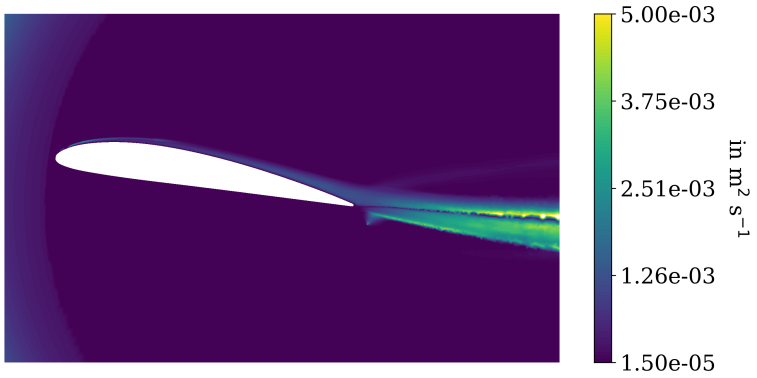

Figure 10: Total viscosity ν_{tot} near the airfoil

frequencies up to $f = 1000\,\text{Hz}$ with the same distribution as in the SPOD.

The domain of the mesh has the size $[L_x \text{ x } L_y] = [7.5c \text{ x } 5c]$, where the area of the inlet is again realized as a "C-shape". It is created with the meshing tool *gmsh* and consists of triangles. The main mesh of the final simulation is shown in Figure 11. For resolvent analysis

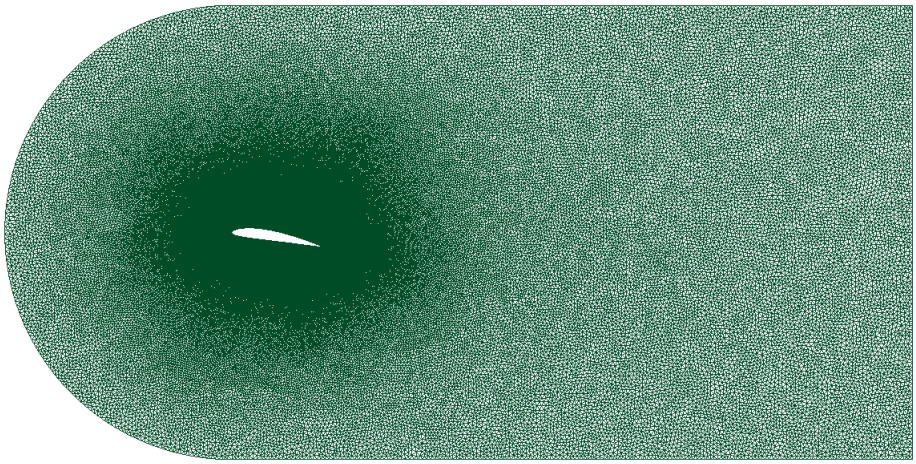

Figure 11: Resolvent: Whole mesh

the requirements for mesh resolution are lower in comparison to the LES, therefore the amount of cells overall and resolution near the wall are less. Nevertheless the mesh has to resolve the features of the mean flow well enough. The total amount of cells is $N^1 \approx 309,000$. At the boundary of the airfoil a cell width of $\Delta x = 4.5 \cdot 10^{-4}\,\text{m}$ is reached. Near wall resolution is presented in Figure 12. To guarantee mesh independence of the results, two other grids are utilized and compared with the results of the main solution. Therefore the amount of cells is modified by the factor by ≈ 20 % for each new mesh. The amount for the obtained grids are $N^2 \approx 257,000$ and $N^3 \approx 212,000$. No finer mesh refinement could be used as the resulting eigenvalue problem is huge and can not be processed by the working memory of the computer anymore.

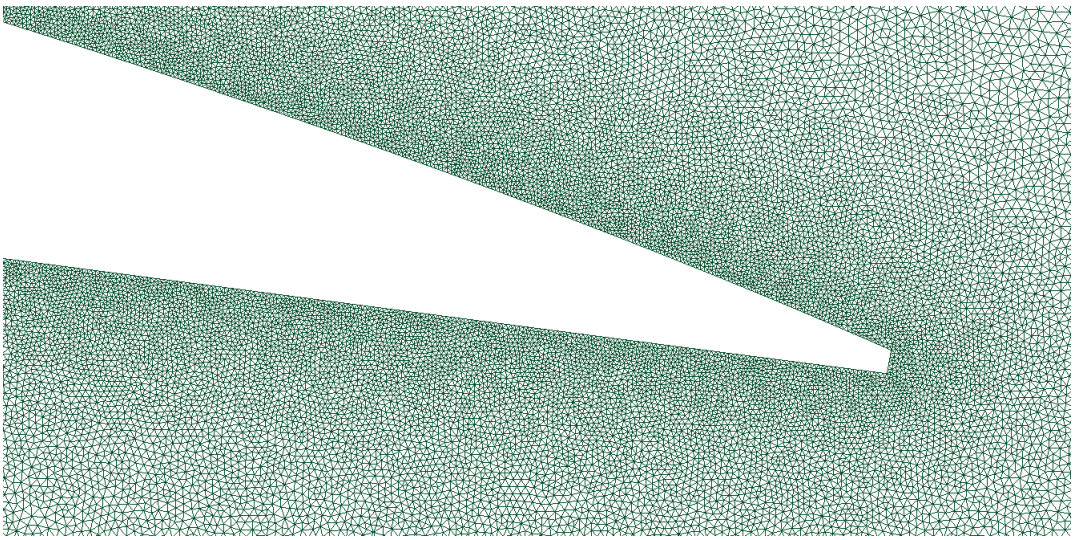

Figure 12: Resolvent: Near wall mesh

As already mentioned, resolvent analysis is sensitive to disturbances because of the involved eigenvalue problem. Hence the boundary conditions are of high importance for a stable solution and different boundary conditions were tested by terms of stability. In contrast to the LES the boundary conditions for the fluctuating part of the flow entities is set in the resolvent setup. In the far-field, including outlet and inlet, homogeneous Dirichlet condition $u' = v' = p' = 0$ is applied. For this reason structures evolving at the airfoil are going to vanish near the outlet. Considering this the length of the domain is extended in streamwise direction enough, so that the modes at the airfoil are not effected. Nevertheless the damping by the high viscosity in the sponge layer is going to weaken structures leaving the unaffected area near the wall. Homogeneous Dirichlet conditions are also used at the wall for the velocity components, but for the pressure homogeneous Neumann condition is used. Finally for the two-dimensional setup the spanwise wave number is set to zero to prohibit any influence of spanwise structures.

4 Results

This chapter contains the results and validation of the conducted LES. In addition SPOD is applied to the obtained flow data. Afterwards the results of the resolvent anlysis are presented and compared to the SPOD.

4.1 LES

In order to validate the LES, the result is compared with experimental data consisting of wall-pressure measurements at the airfoil and with an *XFoil* simulation with the same physical properties. Next the flow features of the instantaneous and the mean flow field are investigated as well as properties of the boundary layer. Furthermore results relevant for the resolvent analysis are shown and temporal features are inspected.

4.1.1 Reference cases

For validation purposes experimental data and *XFoil* simulations are used. At "Institut für Strömungsmechanik und Akustik" of TU Berlin experimental data of the investigated geometry exists. Thereby the wall pressure around the airfoil was measured. As only this one source of experimental data is available for validation, the results of *XFoil* simulations serve as an extra data set for comparison. *XFoil* is a tool for analysis of subsonic flow around airfoils [Dre89]. It includes a panel method with compressible correction and integral boundary layer formulation. Transition criterion is given by e^N- method. Moreover solutions can be computed very quickly and the accuracy of the tool is approved by many sources [Sel03]. The search for the correct configuration of the *XFoil* simulation is already described in Section 3.1.4. The crucial parameter is the point of transition in the *XFoil* simulation. Here it is chosen to provide the best match according to the experimental data. For comparison the pressure coefficient [SN10, p. 368]

$$C_p = \frac{p - p_\infty}{\frac{1}{2}\varrho u_\infty^2} \tag{41}$$

is considered, where u_∞ and p_∞ are the free flow velocity and free flow. Figure 13 shows the values of the pressure coefficient C_p of the *XFoil* simulation, the LES and the experimental data.

Naturally pressure has the highest rise at the leading edge. Due to the angle of attack it is located on the pressure side represented by the lower line. Low pressure values are present at the leading edge on the suction side on account of velocity acceleration. The curve of the pressure coefficient C_p also shows the positive pressure gradient along the suction side. Overall good agreement between experiment, LES and *XFoil* is achieved. Only in the area close to the leading edge on the suction side, deviations from the experimental are found. Near the leading edge a bump in the LES result is observed, which arises due to the tripping element at the surface of the airfoil, where the flow impounds and as a result the pressure increases. For subsequent analysis the *XFoil* simulation is a good further reference case due

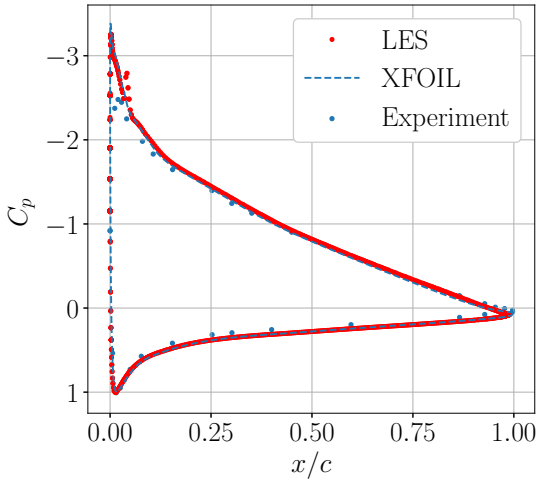

Figure 13: Pressure coefficient C_p

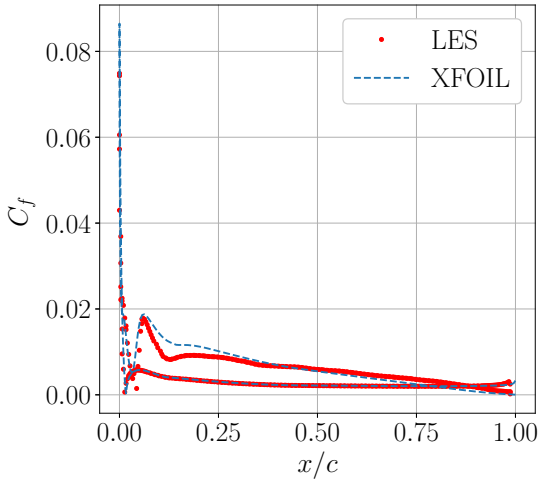

Figure 14: Skin friction coefficient C_f

to the good match between the *XFoil* simulation and the experimental data.

Next *XFoil* and LES results are compared by means of skin friction coefficient as well as drag and lift coefficient. The skin friction coefficient C_f [SN10, p. 483]

$$C_f = \frac{\tau_w}{\frac{1}{2}\varrho u_\infty^2} \tag{42}$$

describes the nondimensionalized local wall shear stress $\tau_w = \eta(\frac{\partial u}{\partial y})_w$, where η is the dynamic viscosity. It is illustrated in Figure 14. The amount of wall shear stress τ_w over the blade serves as an indicator of the flow state in the boundary layer, whether it is laminar or turbulent. High wall shear stresses are linked to a high velocity gradient which occurs in turbulent boundary layers in contrast to lower velocity gradients which are present in laminar flows.

For the LES the temporally and spatially spanwise averaged wall shear stress is observed. The lower line is representing the development on the pressure side and is perfectly matching the results by *XFoil*. The low values of the skin friction coefficient C_f confirm the statement that the boundary layer on the pressure side stays laminar. In comparison skin friction coefficient C_f on the suction side is significantly higher. The boundary layer tripping device excites transition right at the location of the trip, which is visible by the bump at $x/c \approx 0.034$. The location is almost at the same location as in the *XFoil* simulation. Moreover C_f increases exactly to the same value in both cases. Behind the point of transition the LES result underestimates the skin friction coefficient from *XFoil*. Later good agreement is reached, only a slightly higher coefficient in the LES is observed. Overall regarding the skin friction coefficient C_f one can recognize the correct start of transition within in the LES and the turbulent behavior in the boundary layer at the suction side opposed by the laminar pressure side.

As mentioned in Section 2.1.2 modifications of the original dynamic Smagorinsky model by Germano/Lilly exist, that tackle drawbacks of the original version. In the process of LES

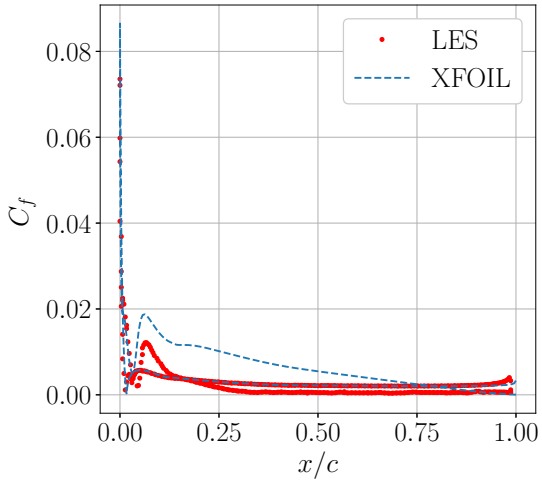

Figure 15: Skin friction coefficient C_f - dynamic Lagrangian Smagorinsky model

simulations the performance of another model, i.e. the dynamic Lagrangian Smagorinsky model is also tested. In Figure 15 the time- and spanwise-averaged skin friction coeffcient of the dynamic Lagrangian Smagorinsky model is presented.

On the pressure side the behavior coincides with the results of *XFoil* and the dynamic Smagorinsky model. However there are huge differences on the suction side. Again the location of transition is correct but skin friction coefficient C_f decreases sharply right after the trip and stays very low along the surface. The solution is in no aggreement with the *XFoil* simulation and led to the decision to use the original dynamic Smagorinsky model in the further process.

The drag coefficient C_d is defined as [SN10, p. 87]

$$C_d = \frac{F_d}{\frac{1}{2}\varrho A u_\infty^2}, \tag{43}$$

where F_d and A are the drag force F_d and the relevant area. For *XFoil* the drag coefficient yields $C_d^X = 0.0214$ versus $C_d^L = 0.0247$ in the LES averaged over time. This is a deviation of $\approx 13.3\%$. The difference is partly induced by the tripping element, which constructed as a block, leads to a drag increase as it impounds the flow. In contrast *XFoil* transition is not accompanied by this drag force as it is excited in an alternative way. The rise of the pressure coefficient C_p at the tripping element in Figure 13 for the LES confirms this conclusion. In Figure 16 the progression of the drag coefficient C_d and the mean drag coefficient are illustrated, showing the highly unsteady behavior of the flow.

Finally the lift coefficient [SN10, p. 418] is

$$C_l = \frac{F_l}{\frac{1}{2}\varrho S u_\infty^2} \tag{44}$$

with the lift force F_l and the relevant area S .The result for *XFoil* is $C_l^X = 1.25$ and in the

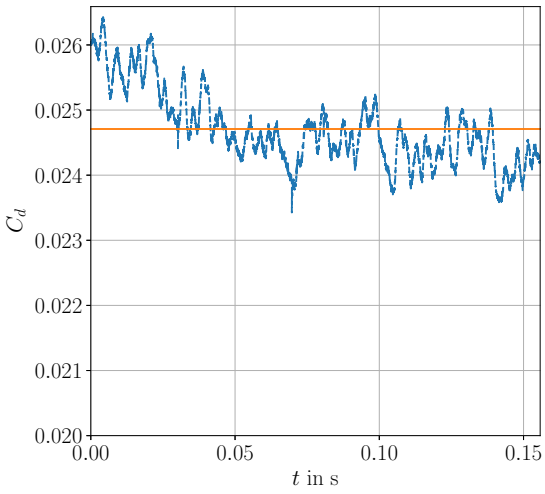

Figure 16: Drag coefficient C_d

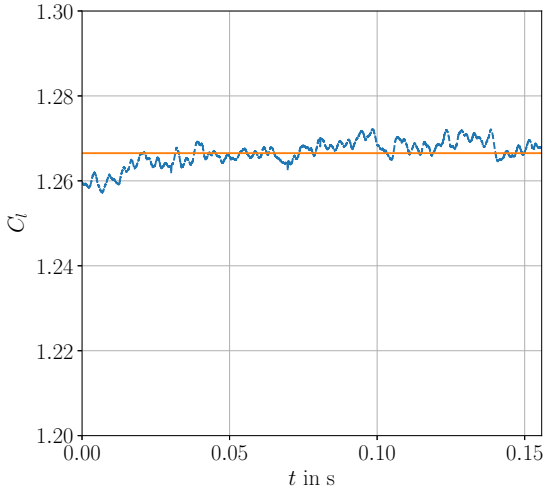

Figure 17: Lift coefficient C_l

LES $C_l^L = 1.266$ which is a low difference of $\approx 1.1\%$. The lift coefficient C_l is shown in Figure 17 and indicates that the simulation is in a converged state after half of the simulation which is also confirmed by the progression of the drag coefficient C_d in Figure 16.

In summary the results of LES are in good agreement with the *XFoil* and experimental data. Only small deviations can be found except for the drag coefficient C_d, where differences can partly be traced back to the different approaches for the tripping. Further the instantaneous and mean flow features are illustrated.

4.1.2 Instantaneous fields

The instantaneous flow field also called a snapshot of the flow is shown for time step $t = 0.155\,76\,\text{s}$. It is presented at the xy-plane for $z = 0\,\text{m}$. In subsequent analysis the snapshots play an important role for the evaluation of the SPOD. In Figure 18 the fluctuating velocity components and the pressure are therefore shown. For this the flow entities are subtracted by their mean $u' = u - \overline{u}$, where the time-averaged value is denoted by an overbar $\overline{u}$.

Given the velocity fields, the laminar state of the pressure side and turbulent state of the suction side can easily be distinguished. Early transition on the suction side at $x/c = 0.034$ induced by the tripping element leads to a highly turbulent boundary layer. In addition unsteady components are seen in every dimension. The boundary layer starts to thicken in size heavily after the thickest position of the blade. The highest fluctuation at the moment of the snapshot is observed in the streamwise component u'. Besides the existence of coherent structures in the flow is already weakly recognizable, as connected objects are visible in the flow.

4.1.3 Mean flow fields

The mean flow of the LES is of high interest in this analysis, as it supplies one part of the inputs for the resolvent analysis later in the process. In Figure 23 the time-averaged fields of

Fluctuating velocity component u'

Fluctuating velocity component v'

Fluctuating velocity component w'

Figure 18: Snapshots at $t = 0.155\,76\,\mathrm{s}$

all velocity components $\boldsymbol{u} = (u\ v\ w)$, pressure p and turbulent viscosity ν_t are illustrated at the xy-plane where $z = 0\,\mathrm{m}$.

The velocity component in streamwise direction $\overline{u}$ shows clearly the thickening of the turbulent boundary layer on the suction side. In the direction of the span the mean velocity $\overline{w}$ decreases strongly in comparison to the already shown instantaneous velocity w in Figure 18. Nevertheless because of the homogeneity in spanwise direction w should be zero on average. This observation indicates that the simulation has not yet "converged" statistically. However, as for the resolvent analysis only the 2D dimensional flow field in x and y direction are of interest and the solutions of those components are better "converged", it should not

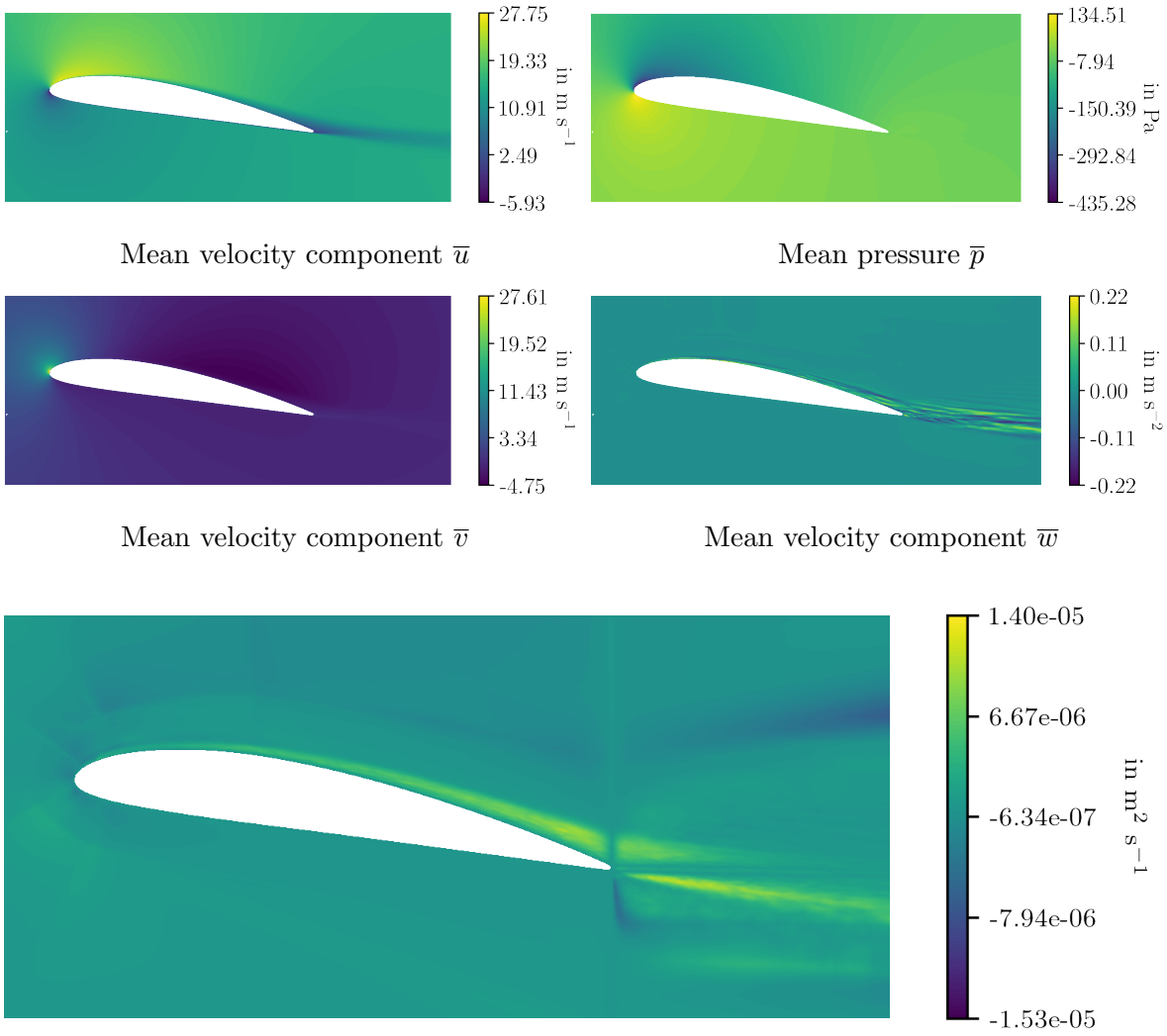

Figure 19: Mean flow fields of xy-plane at $z = 0\,\mathrm{m}$

affect the future analysis. In Figure 20 streamlines of the time-averaged velocity field $\overline{\boldsymbol{u}}$ and the magnitude of the velocity field $|\boldsymbol{u}|$ are shown. At the blunt edge a small recirculation zone is detected, where the streamlines are wrapping around and velocity is very low. Besides that no separation on the suction side is observed.

The mean pressure field has a stagnation pressure at the leading edge of $p_{stag} = 134.51\,\mathrm{Pa}$. Low pressure due to high velocity at the beginning of the suction side is strongly increasing further downstream and leads to a positive pressure gradient at the suction side which is slowing down the flow. When viewing the turbulent viscosity ν_t, areas of negative viscosity are detected. This is possible, because the Smagorinsky coefficient C_s can yield negative values in the dynamic Smagorinsky model. The negative values of the turbulent viscosity are considered as backscatter effects. Unfortunately negative values are also observed in regions, where no turbulence is expected, especially downstream in the top right corner of Figure 23. The disturbances are a product of the only locally averaging dynamic Smagorinsky

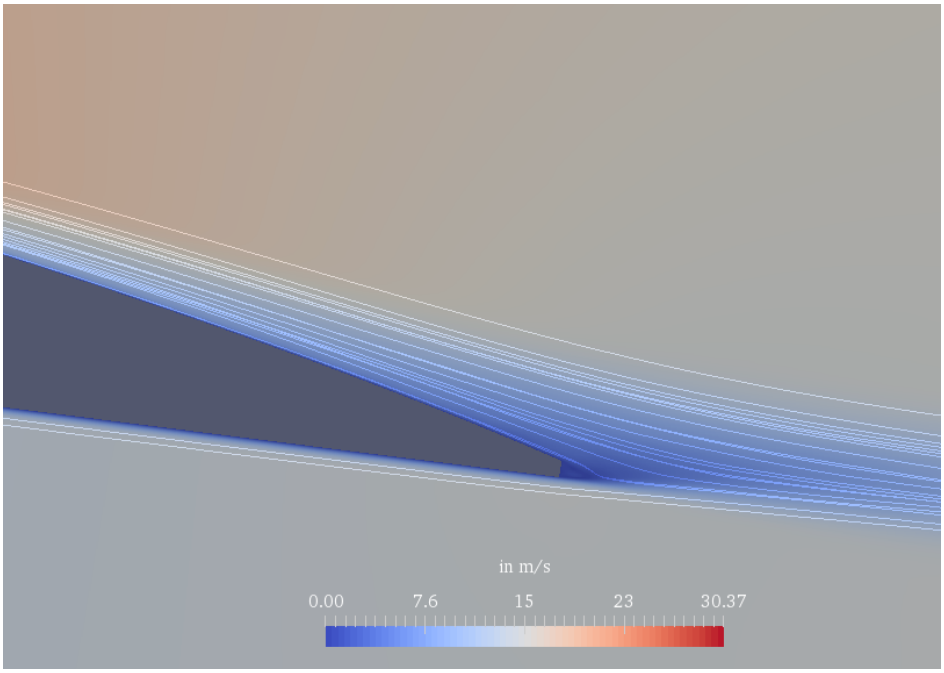

Figure 20: Streamlines at the trailing edge and the mean velocity magnitude $|\overline{\boldsymbol{u}}|$

model and low mesh quality. Noteworthy is that these problems did not occur in the test simulation with the dynamic Lagrangian Smagorinsky model, thus the mesh is not the main reason of the issue. Luckily the erroneous zones are mostly in distance to the airfoil and are not interfering with the turbulent flow. Besides this problem the simulation shows expected behavior of a high turbulent viscosity ν_t in the turbulent boundary layer with a maximum value of $\nu_t^{max} = 1.4 \cdot 10^{-5}\,\mathrm{m^2\,s^{-1}}$ almost the value of molecular viscosity. Directly at the blade and at the trailing edge the turbulent viscosity ν_t vanishes as the mesh resolution is very fine and turbulence modeling is low in comparison.

Next the mean fields of the Reynolds stresses τ_{ij} or respectively the equivalent without division by density $\tau'_{ij} = \frac{\tau_{ij}}{\varrho} = \overline{u'_i u'_j}$ is shown. Further the entities are shown after averaging over the span of the blade, as these are the flow fields used for the calculation of the total viscosity ν_{tot}, which serves a an input of the resolvent analysis. Naturally Reynolds stresses are non-zero in the turbulent boundary layer and the wake. Especially at the shear layer downstream the recirculation zone at trailing edge, where turbulent suction side and laminar pressure side meet the Reynolds stresses peak. Even higher Reynolds stresses are encountered in the region of transition downstream the trip, whereas for the Reynolds stress $\overline{u'^2}$ values stay high for a long distance downstream.

4.1.4 Boundary layer profiles

For further investigations of the flow the mean velocity profile is presented in the boundary layer in Figure 22 . This is done at four locations of the blade $x/c = 0.23, 0.59, 0.77, 0.95$, which are also visible in Figure 5. Therefore the tangential component is normalized by the friction velocity u^* and shown over the nondimensional wall distance y^+. For the turbulent

Reynolds stress component $\overline{u'^2}$

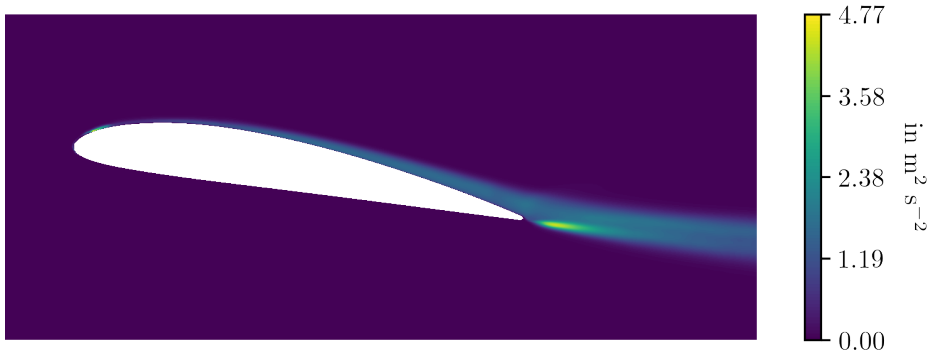

Reynolds stress component $\overline{v'^2}$

Reynolds stress component $\overline{u'v'}$

Figure 21: Span-averaged Reynolds stresses

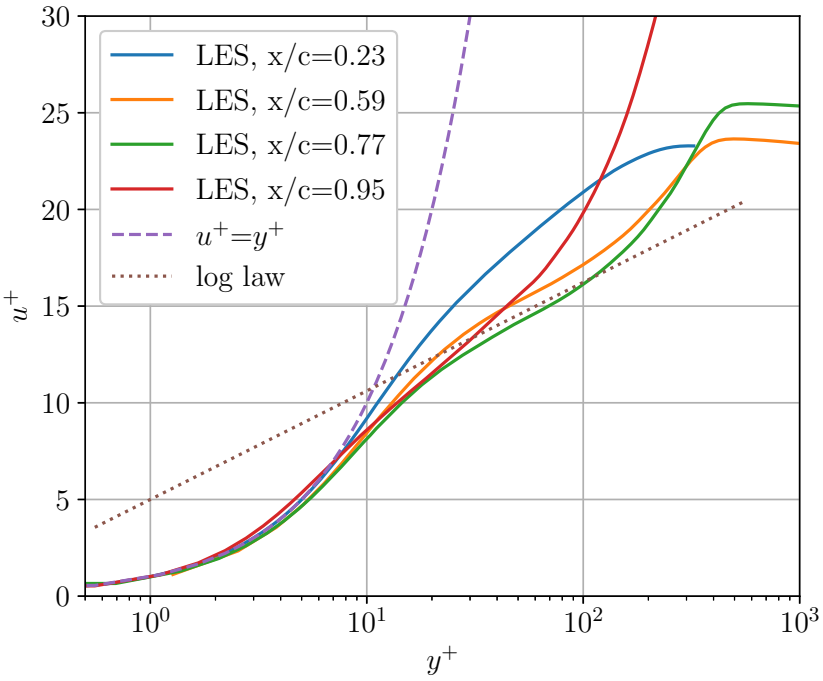

Figure 22: Nondimensional boundary layer profiles

boundary layer the universal behavior directly at the wall is well known. In the first layer at the wall, i.e. the viscous sublayer, linear relation between the dimensionless velocity and the nondimensional wall distance exists $u^+ = y^+$. This zone ranges from $0 < y^+ < 5$. The second universal law in the boundary layer concerns the log layer region. It is located at $30 < y^+ < 350$. The equation for the logarithmic law of the wall is $u^+ = \frac{1}{k} \log y^+ + C$ where $k \approx 0.41$ and $C \approx 5$ [OBR06, p. 136]. In between the so called buffer layer is present, connecting sublayer and loglayer. For comparison the universal laws for turbulent flows are shown in the resulting plot as well. Firstly the viscous sublayer is considered, which is resolved by $\approx 8 - 10$ points in the grid. The results of the LES are very close to the universal law in the viscous sublayer for most of its length and therefore show good agreement in this region. Slight differences for all locations could be the consequence of a not yet converged value of the mean wall shear stress $\overline{\tau}_w$ in the nondimensionalization process. This distorts the scaling in the graph. In the log layer higher deviations are found. The location most downstream at $x/c = 0.95$ has a too steep slope. The values show a logarithmic relation but not in the same proportion as the log law. Possibly the near presence of the trailing edge impacts the velocity in the boundary layer. Best fit for the log law area are achieved at locations $x/c = 0.59$ and $x/c = 0.77$. One can recognize logarithmic behavior in the range of $20 < y^+ < 150$ so that the log law area is smaller than the usual range. At $x/c = 0.23$ the behavior is almost logarithmic but with higher nondimensional velocities. It is located near the tripping element, which is certainly influencing the curve. In fact historic effects of the tripping could disturb the universal behavior of turbulent flow. Another major issue concerning differences between

the simulation and the universal law is the presence of the pressure gradient at the suction side of the blade. The universal laws are not considering a pressure gradient, so that some deviation is inevitable. Regarding this fact and the good agreements in distance of either trip or trailing edge the boundary layer until $y^+ = 150$ appears well resolved.

Next the Reynolds stresses $\overline{u_i u_j}$ without multiplication by density ϱ in the boundary layer are presented. In addition the stresses are normalized by friction velocity u^* and the tangential and normal velocity components u'_t and u'_n are observed. The locations are $x/c = 0.23, 0.59, 0.95$. The first location $x/c = 0.23$ shows a high rise for the tangential component of the Reynolds stress $\overline{u_t^2}^+$ in comparison to the other line probes. This is probably an effect of the near tripping element as this high value decreases farther downstream respecting the other locations. The tangential Reynolds stress $\overline{u_t^2}^+$ should peak at $y^+ = 10$. This behavior is visible only at the last location. For the other two positions a small shift for the peak exists. Again this shift could be induced by the tripping, so that universal turbulent boundary layer evolves first in some distance past the trip. Moreover tangential Reynolds stress $\overline{u_t^2}^+$ is increasing after the first peak again and forms a bump at location $x/c = 0.95$. The beginning of this bump is already visible upstream for location $x/c = 0.59$. The positive pressure gradient is responsible for this appearance. In addition the Reynolds stresses lose their smooth behavior at the trailing edge. This is another indication of insufficient simulation time. Finally the wall-normal component $\overline{u_n^2}^+$ appears odd. Usually it should rise after the tangential component, but here it is also rising at $y^+ = 10$. In summary the Reynolds stresses show expected or explainable behavior for most components.

4.1.5 Spectral analysis

Furthermore the unsteadiness of the flow in the turbulent boundary layer is analyzed. At three locations in the boundary layer $x/c = 0.23,\ 0.59,\ 0.95$ (see Figure 5) on the suction side the power spectral density (PSD) of the velocity fluctuations is computed. This is realized in three different distances to the wall. The first point is located in the buffer layer, i.e. the transition between viscous sublayer and log layer, which is also visible in Figure 22. In addition the other probes are located in the log layer and the margin of the boundary layer respectively as it is represented in Figure 22. The results are shown in Figure 24. The columns represent each streamwise location and the rows are from top to bottom, buffer layer, log layer and outer region.

Welch's method [Wel67] is applied to the data to extract the power spectral density. The averaging procedure implemented in Welch's method offers the advantage to denoise the data and therefore helps to visualize the flow field of high turbulence in a clearer way as normal discrete Fourier transformation. The procedure divides the time period in overlapping segments. A segment length of one fifth of the total amount of snapshots in combination with 50 % overlap is used. Further a hanning window is utilized in the calculations of a periodogram of every segment. Averaging over each result gives the final power spectral density. Typically three regions in the energy spectrum of the flow exist. There are large, high energetic structures with low frequency and small dissipating scales of high frequency on

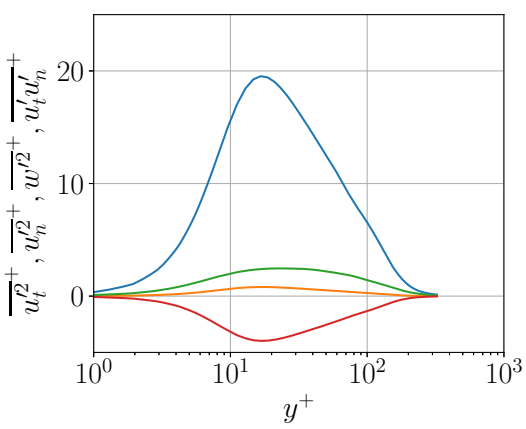

Location at $x/c = 0.23$

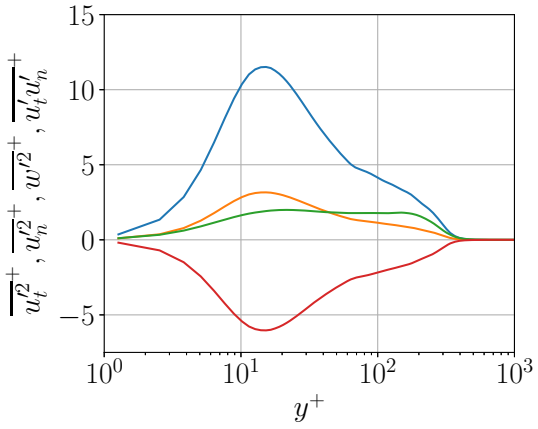

Location at $x/c = 0.59$

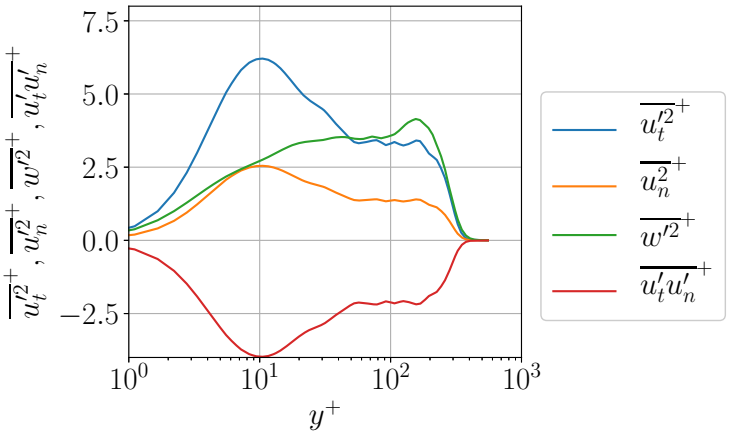

Location at $x/c = 0.95$

Figure 23: Reynolds stresses in the boundary layer

the respective side of the spectrum. In between lies the inertial subrange, which is determined by Kolmogorov's -5/3 law, so that the energy per Hz in the spectrum decreases by the slope of $k^{-\frac{5}{3}}$ throughout this zone [OBR06, p. 253]. The slope of this law is inserted into the power spectrum graphs of the probes. By comparison between the Kolmogorov law and the spectrum one can see that only the beginning of the inertial subrange is resolved during the simulation. Another important aspect of inertial subrange is, that it contains the zone where LES switches from resolving turbulence to the modeling of turbulence. Since the filtering is done implicitly by the grid width, resolved scales differ in the computational domain. This can be observed in the results of power spectral density in Figure 24. It is especially the case for $x/c = 0.95$ where the mesh coarsens strongly in the boundary layer. The frequencies are cut sharply in the outer region in contrast to the other two probe locations. Overall the cutoff frequency f_c is about $\approx 5000\,\text{Hz}$. Therefore the point in the power spectral density graphs where the power per frequency starts to decline steeper than the slope by Kolmogorov's law

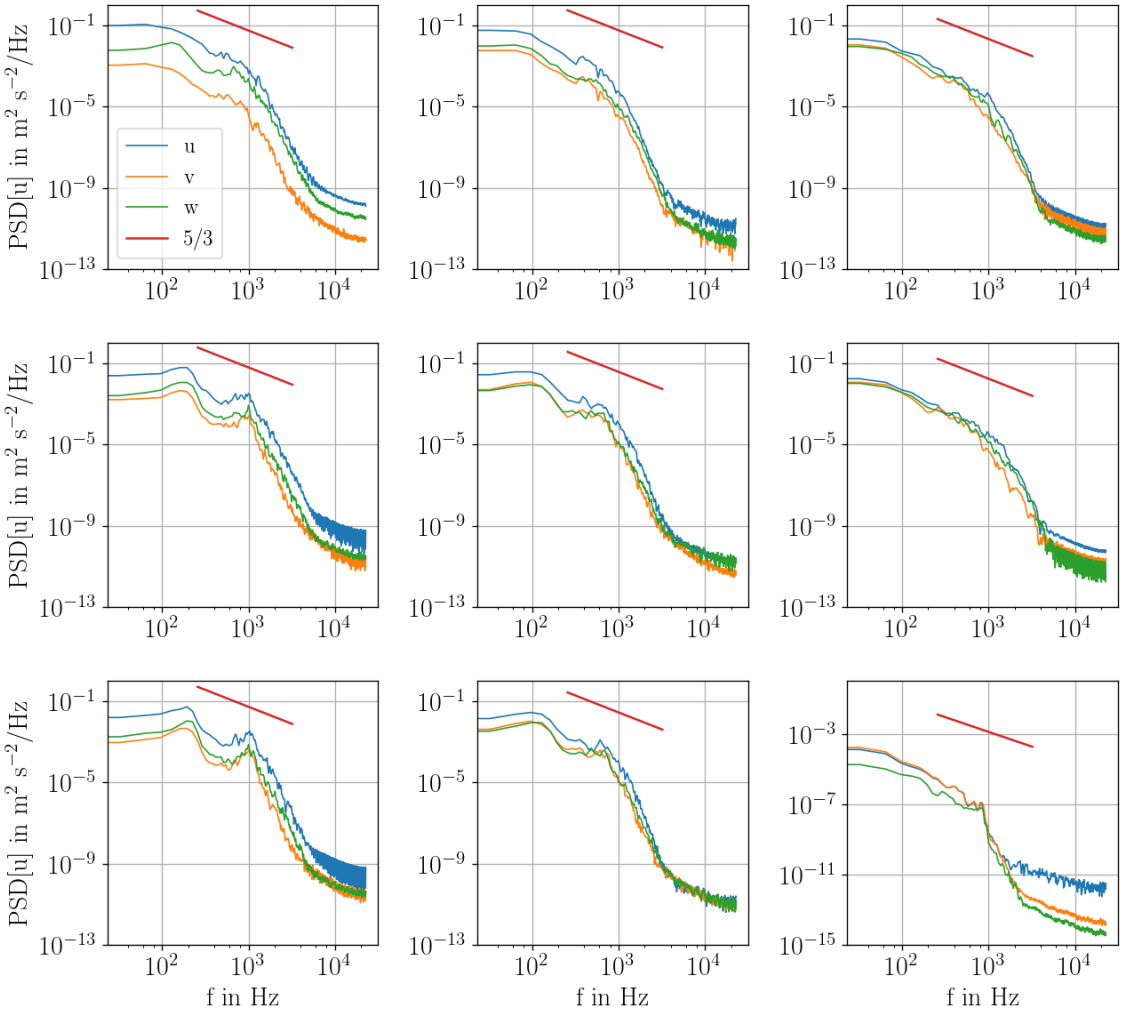

Figure 24: Power density spectrum - left: $x/c = 0.23$, middle: $x/c = 0.59$, right: $x/c = 0.95$ - top: buffer layer, middle: log layer, bottom: outer region

is not the start of dissipating scales but the influence of the cutoff filter. For the streamwise location $x/c = 0.23$ two peaks at $f = 300\,\text{Hz}$ and $f = 1100\,\text{Hz}$ are noted in the log layer and the outer region. Those peaks are also visible for $x/c = 0.59$ but with less intensity. Probably these are frequencies excited by tripping element, propagating and disintegrating on the suction side. Concluding this by the observation that at the location $x/c = 0.95$ furthest downstream, this bump isn't observed.

Usually a low angle of attack for an airfoil produces a broadband power spectrum where most of the frequencies contribute almost equally to the energy in the flow. Then the spectrum does not show peaks for a specific frequency. This is observed in the buffer layer for all locations and at $x/c = 0.95$ in the log layer. Unfortunately the simulation time is too short to resolve low frequencies in the order $\approx 100\,\text{Hz}$ precisely. By splitting the data into five segments, structures with a frequency $f = 100\,\text{Hz}$ only appear about three times in the flow.

4.2 SPOD

In this section the results of SPOD applied to the LES data are presented. At first SPOD is calculated from one cross-section of the LES in the area of interest near the airfoil. Major aspects of the case are explained, but the focus lies on the following results of the span-averaged data, as it is more relevant in the comparison to the resolvent analysis. After examination of the span-averaged SPOD for the region all around the airfoil and the wake, a weighted SPOD is performed, which concentrates on the suction side of the blade. Throughout only two-dimensional flow data is considered, so that the data matrix Q contains velocity components u' and v'. Besides the data matrix Q consists of 7080 snapshots saved during the LES. For every computed SPOD the segment length, of the undertaken Welch's method during computation, is set to 400 snapshots per block with an overlap of 50 %. After tests of different segment lengths it was found to be an appropriate length to get a good resolution of the structures in the flow. This setup for the SPOD results in 200 frequencies ranging from 114 to 22 727 Hz. For the computation of the SPOD the *Python* module "pyspod" is utilized.

The frequencies of interest are the high energetic, low frequency modes, so that the focus lies on the frequencies up to $f = 1000\,\text{Hz}$.

4.2.1 Non-averaged flow

For the initial analysis the cross-section lies at $z = 0\,\text{m}$. At the beginning the resulting eigenvalues for the corresponding frequencies are computed and shown in Figure 25. Each line is representing one of the sorted eigenvalues and the intensity of the line reduces with decreasing rank of the eigenvalue.

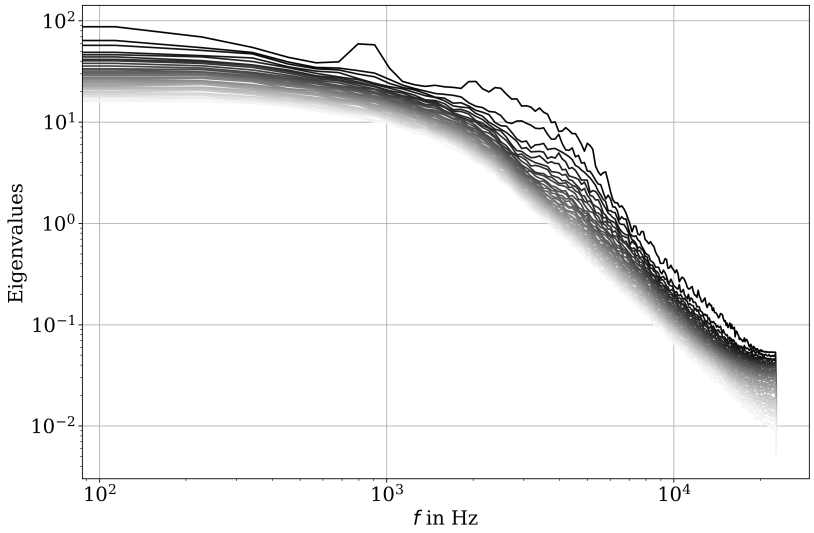

Figure 25: Eigenvalues over frequency of the SPOD

The eigenvalues are rising for lower frequencies as large eddies are the energy carrying structures and the eigenvalues are corresponding to the amount of energy at each frequency.

A peak for the first eigenvalue occurs at $f \approx 900\,\text{Hz}$, which appears odd as the configuration of high Reynolds number and low angle of attack $\alpha = 9°$ should yield a broadband spectrum with no dominant structure at a specific frequency. The concerned mode for this frequency is examined in the deeper analysis for the SPOD of the span-averaged LES. At the cut-off length, which is about $f \approx 5000\,\text{Hz}$, the eigenvalues decrease sharply as expected because eddies of this size should not be resolved anymore. Usually one can say that the modes are well separated when the eigenvalues differ by one order of magnitude. This is not the case in the SPOD results and will be investigated further for the truncated span-averaged SPOD, as second and third mode are plotted there. Along the analysis the SPOD modes corresponding to the highest eigenvalue are called the first SPOD modes. In Figure 26 the first modes of frequency $f = 227\,\text{Hz}$ are shown for u' and v' component. These are the most clear modes

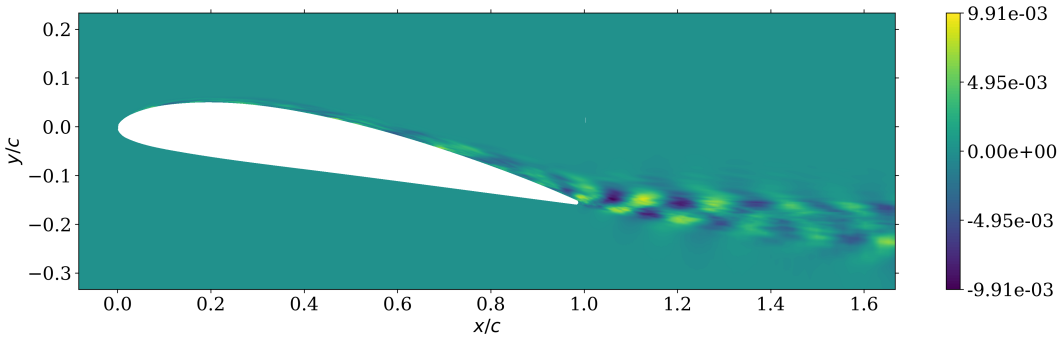

First mode of velocity component u'

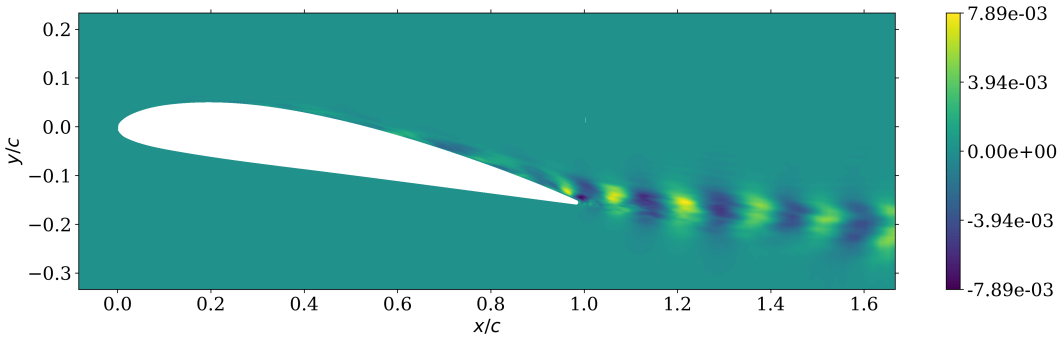

First mode of velocity component v'

Figure 26: SPOD modes at $f = 227\,\text{Hz}$

until $f = 1000\,\text{Hz}$. The existence of coherent structures in the turbulent boundary layer and the wake is already visible. Distinct wake modes are present, which start evolving at about $x/c = 0.3$ on the suction side of the airfoil. Still the modes are blurred and unfortunately for most of the frequencies the structures in the result are not well resolved. The modes are ambiguous and difficult to interpret because of the comprised noise, a consequence of the relative short computation time, as the simulation is not yet statistically "converged".

For further analysis the span-averaged LES data is considered, which offers two benefits. On the one hand the results of the SPOD should yield clearer information as averaging over

the homogeneous direction is performed. On the other hand for the comparison of the SPOD to the later conducted resolvent analysis it is preferable that both cases are set up with the same properties. Resolvent analysis will be computed for the two-dimensional flow without existing spanwise structures. Regarding this the snapshots of the LES are averaged in span direction for elimination of the dependency in the z-direction.

4.2.2 Span-averaged flow

At first the eigenvalues are considered in Figure 27. The peak at $\approx 900\,\mathrm{Hz}$ is amplified after the averaging. Despite this the spectrum does not vary much in comparison to the non-averaged eigenvalue spectrum.

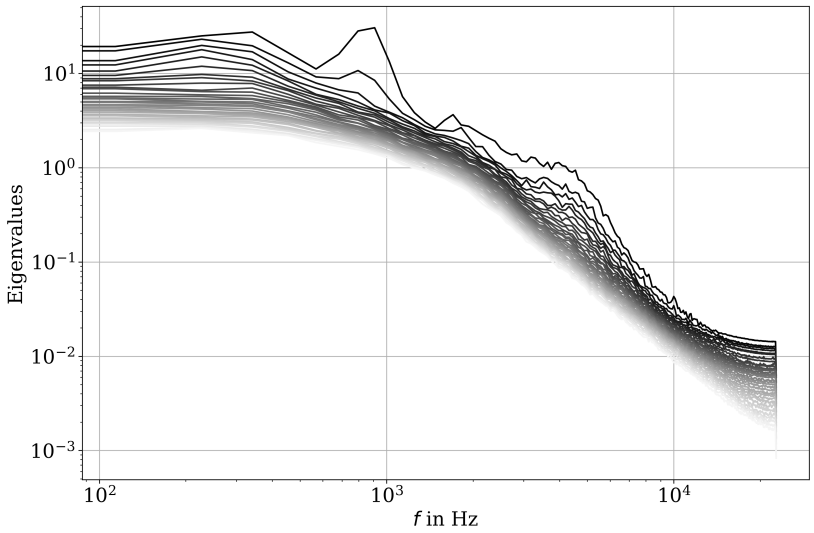

Figure 27: Eigenvalues over frequency of the span-averaged SPOD

In Figure 28 the SPOD modes are shown for the same frequency $f = 227\,\mathrm{Hz}$ as in the non-averaged data. The same type of coherent structures as in the non-averaged SPOD evolve, but they appear more clear and most of the noise is removed. Again wake modes are the dominant structure visible, but for u' and v' a different shape of the mode in the wake is detected. The wave packet of the v' component is symmetric in the vertical direction though the mode for the u' component is shifted diagonally. Due to the span-wise averaging the intensity in the wake increased, probably a consequence of removing the noise. In comparison to the former non-averaged SPOD the modes are starting further downstream on the suction side. This could just be the result of the new scaling induced by the rise in the intensity of the structures in the wake, so that structures at the blade are relatively smaller than before. As a weighted SPOD is conducted later in the analysis, structures in the boundary layer are then in the focus of the investigation.

Next the SPOD modes of higher frequencies are shown, as they reveal other structures present in the flow fields. At first the first modes at frequency $f = 445\,\mathrm{Hz}$ are illustrated

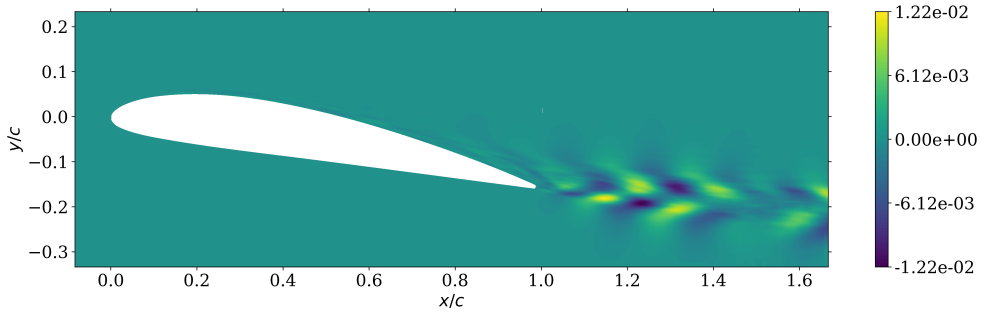

First mode of velocity component u'

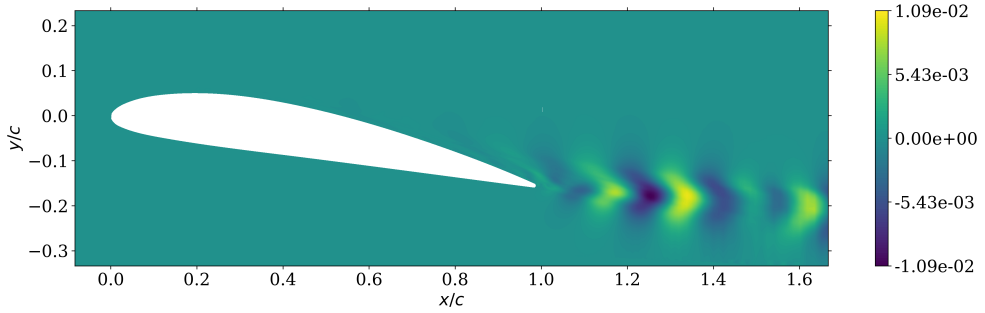

First mode of velocity component v'

Figure 28: SPOD modes at $f = 227\,\text{Hz}$ of the span-averaged flow

in Figure 29. Coherent structures in the turbulent boundary layer are faintly present, but the most energetic zone is downstream the trailing edge. By contrast with the wake mode of $f = 227\,\text{Hz}$ the amplitude of the wave packets decreases rapidly after a short amplification. For the u' component the split shape of the wake is again visible. In Figure 30 for the first mode at a higher frequency $f = 909\,\text{Hz}$ only wave packets at the trailing edge are present. The small zone right at the trailing edge, where no energetic structures are found, represents the area of recirculation with small velocities.

The high amplification of the structures downstream the trailing edge in the wake is detected for all frequencies. This is cause by the fact that at the trailing edge the turbulent flow from the suction side and the laminar pressure side meet, which boosts the intensity of the already existing coherent structures. Furthermore a peak in the eigenvalue spectrum at frequencies around $f \approx 900\,\text{Hz}$ was observed. For this frequency dominant structures only appear in the highly amplified region downstream the trailing edge. One aspect, which could be connected to this rise in the eigenvalues, is the difference of mesh refinement around the airfoil. The region downstream the trailing edge is better resolved in comparison to the suction side and therefore represents high frequencies better. This could yield a higher magnitude for high frequencies in this area. In addition other possibilities for the high eigenvalues remain. More detailed investigations would be needed for a certain explanation, but as this work concentrates on the structures in the boundary layer, it is not further discussed. Besides the wave length of the modes visible naturally decreases with a higher frequency.

For even higher frequencies the dominant component in the flow becomes the area at the tripping element. At a frequency of $f = 3750\,\text{Hz}$, represented in Figure 31, the structures

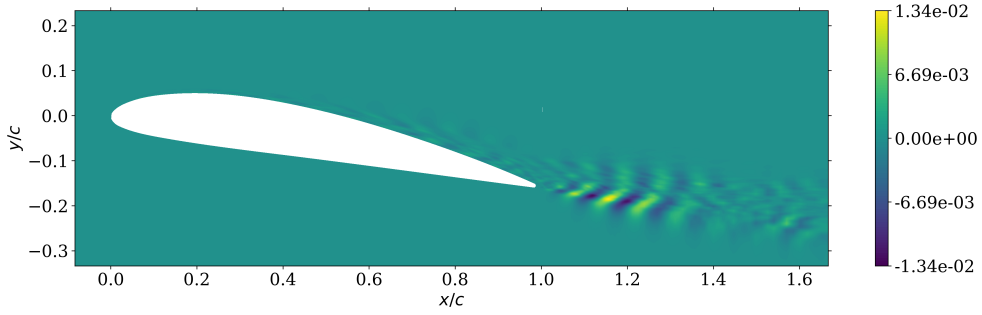

First mode of velocity component u'

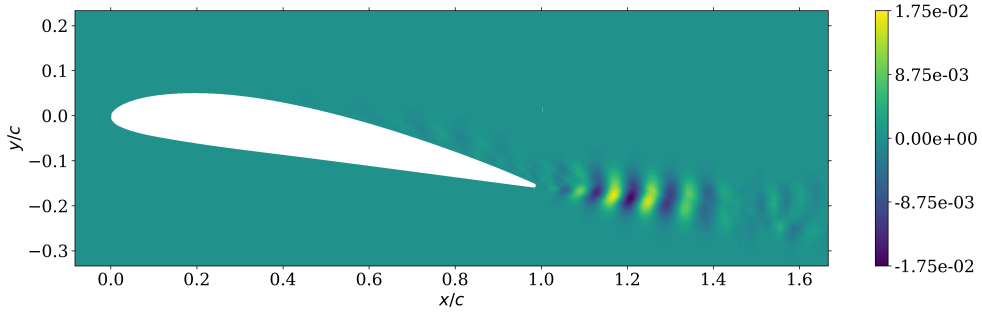

First mode of velocity component v'

Figure 29: SPOD modes at $f = 445\,\mathrm{Hz}$ of the span-averaged flow

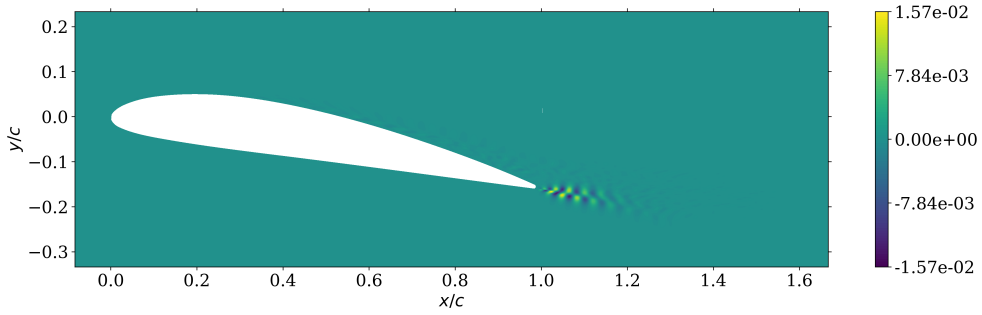

First mode of velocity component u'

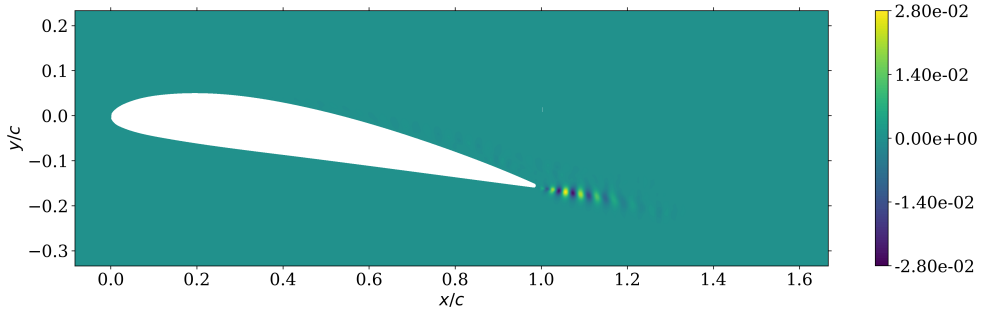

First mode of velocity component v'

Figure 30: SPOD modes at $f = 909\,\mathrm{Hz}$ of the span-averaged flow

induced by the tripping element, where transition starts, are the dominant feature of the flow. The first mode only contains amplitudes in this small region near the leading edge. Moreover the structures induced by the trip dissolve rapidly for this frequency. Hereby the tripping element appears only as a local stimulator for this frequency, which is in fact a good sign, as the trip should cause the start of transition, but it should not affect the whole flow features in a different way than natural transition does. Besides the tripping modes start to be the only major factor at a frequency of about $f \approx 3500\,\mathrm{Hz}$ by examining the other frequencies.

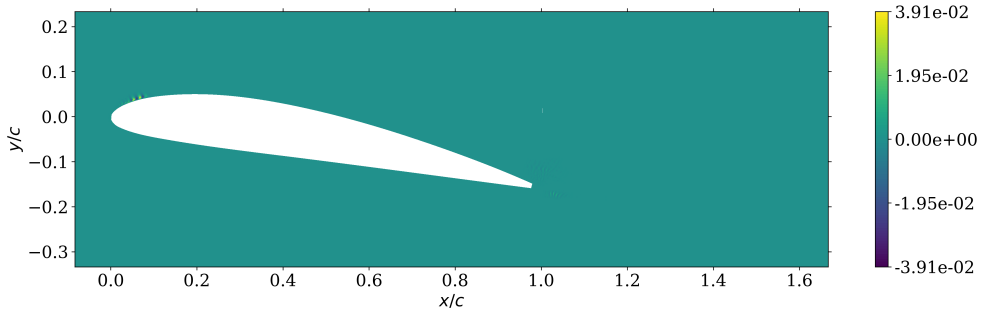

First mode of velocity component v'

Figure 31: SPOD mode at $f = 3750\,\mathrm{Hz}$ of the span-averaged flow

4.2.3 Weighted span-averaged flow

Finally the results of the weighted SPOD are examined. For this only the flow until $x/c = 1$ is weighted. The eigenvalues are shown in Figure 32. A distinct peak is not detected anymore like in the former SPOD results, which becomes obvious, when considering that the region of the structures downstream the trailing edge are truncated. This leads to the expected broadband turbulence in the flow. In addition a strong decrease in the range of the cut-off frequency reoccurs. Moreover the first and second eigenvalue do not differ significantly, therefore the eigenvalues are not well separated. This is investigated by observation of the second and third eigenmode at one frequency at the end of this section.

At first frequency $f = 227\,\mathrm{Hz}$ is demonstrated in Figure 33. The beginning of coherent structures evolving in the boundary layer are visible at $x/c \approx 0.7$. The u' mode includes more noisy features, but one can say that both modes u' and v' coincide by their shape, location and magnitude. The Figures 34 and 35 show the results of respectively $f = 568\,\mathrm{Hz}$ and $f = 909\,\mathrm{Hz}$. In contrast to the mode at $f = 227\,\mathrm{Hz}$ the modes of u' and v' differ strongly. The u' mode separates into two zones. One shear layer part on top of another zone, where wave packets are propagating along the wall. Contrary to the u' mode for the v' mode one homogeneous mode is detected. These observations hold for both higher frequencies $f = 568\,\mathrm{Hz}$ and $f = 909\,\mathrm{Hz}$. In general the structures increase in intensity while moving downstream the airfoil but for $f = 909\,\mathrm{Hz}$ intensity declines again at the trailing edge. This may be due to structures behind the trailing edge. In addition structures are naturally smaller for the higher frequencies as the wave length reduces accordingly. With increasing frequency the start of arising structures moves towards the leading edge. This

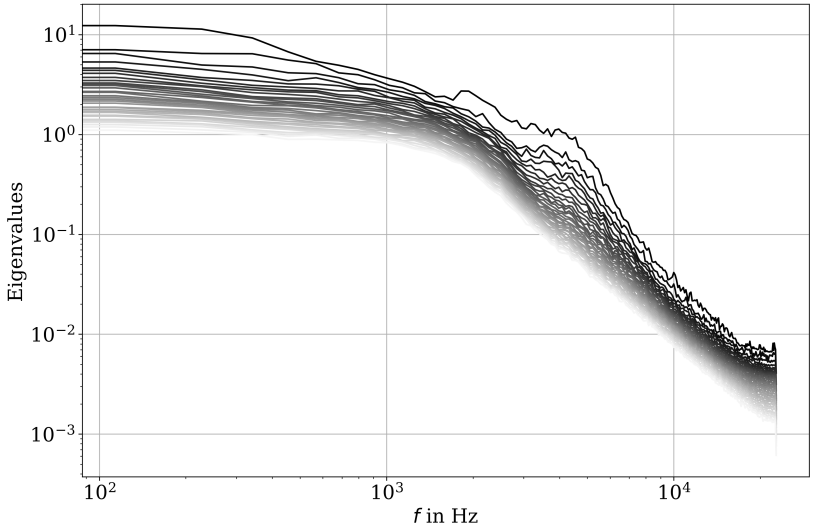

Figure 32: Eigenvalues over frequency of the weighted SPOD

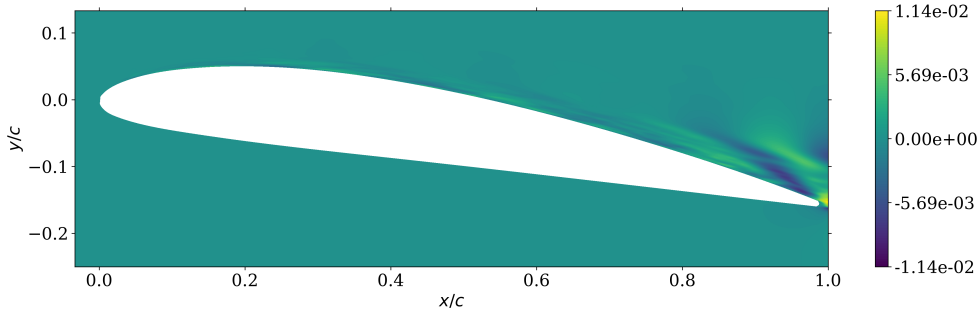

First mode of velocity component u'

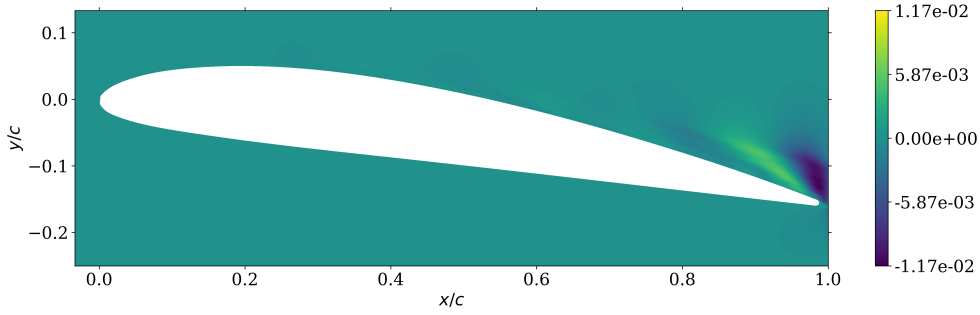

First mode of velocity component v'

Figure 33: Weighted SPOD modes at $f = 227\,\mathrm{Hz}$

effect can be explained by the connection between eddy size and frequency. Small wave lengths, which are associated to a high frequency, are the initiator for instabilities, so that they are present with higher amplitude further upstream at the wall. This observations lead to the conclusion that Kelvin-Helmholtz structures evolving in the turbulent boundary layer are the major instability mechanism present after excitation of transition by the trip. Thus the high positive pressure gradient leads to a significant Kelvin-Helmholtz instability.

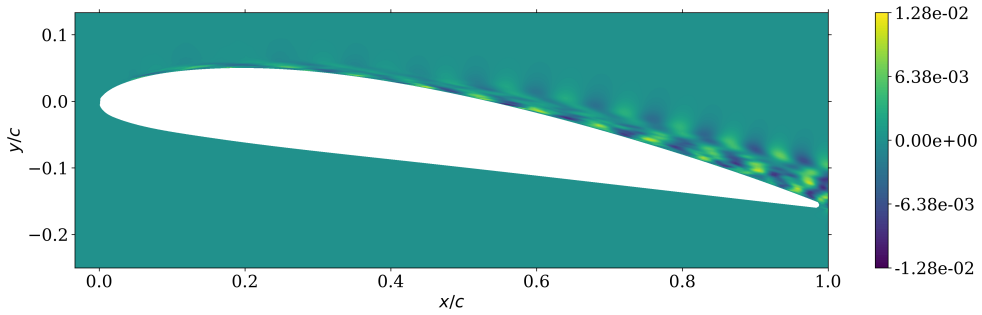

First mode of velocity component u'

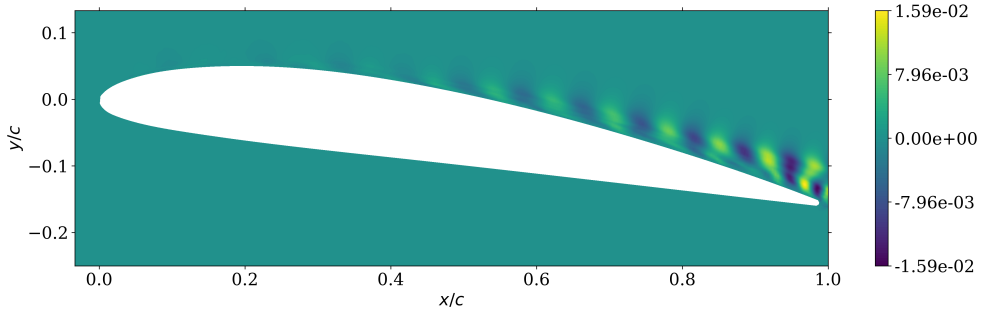

First mode of velocity component v'

Figure 34: Weighted SPOD modes at $f = 568\,\mathrm{Hz}$

From the earlier plots the development of structures near the leading edge does not become clear. Therefore the modes near the leading edge are shown in Figure 36. Interestingly for the SPOD mode of the u' component the structures evolve right after the trip, whereas structures in the v' component are only faintly present at the beginning of the wall. Possibly the modes induced by the trip are more present in the streamwise component. Further the result of the u' component could be partly a mix of tripping modes and modes evolving from Kelvin-Helmholtz structures through the instability mechanism.

Moreover other modes than the one corresponding to the first eigenvalue are examined as for all SPOD results eigenvalues are not strongly separated. The second and third SPOD mode of the frequency $f = 568\,\mathrm{Hz}$ are illustrated in Figure 37 as an example. First and third mode are very similar to each other. The second mode differs a little more as the shape of the wave packets in the boundary layer are more inclined. But overall the major coherent structures are represented by the same mechanism, hence the noise may hinder the SPOD to reach one dominant mode of the structures and leads to several similar high energetic modes. A longer simulation time may improve the result and yield a stronger separation between the eigenvalues as the modes are better “converged”.

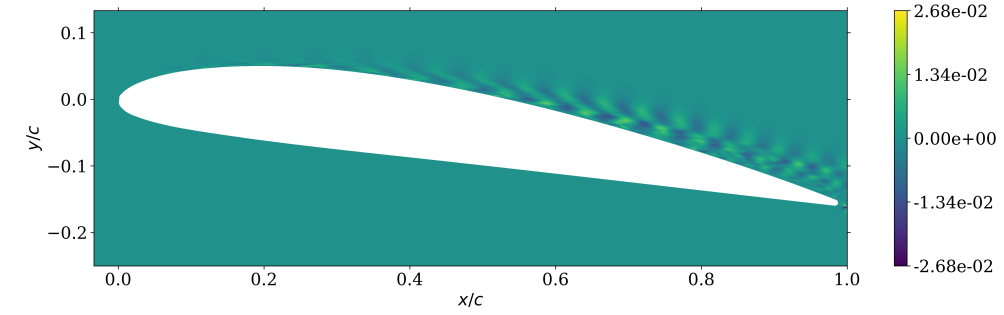

First mode of velocity component u'

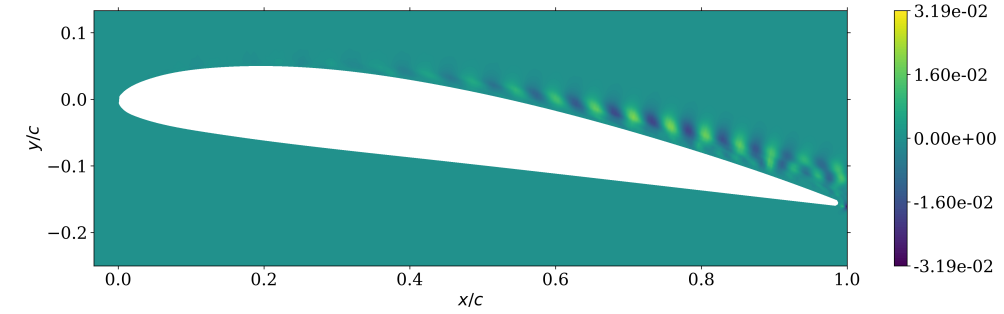

First mode of velocity component v'

Figure 35: Weighted SPOD modes at $f = 909\,\mathrm{Hz}$

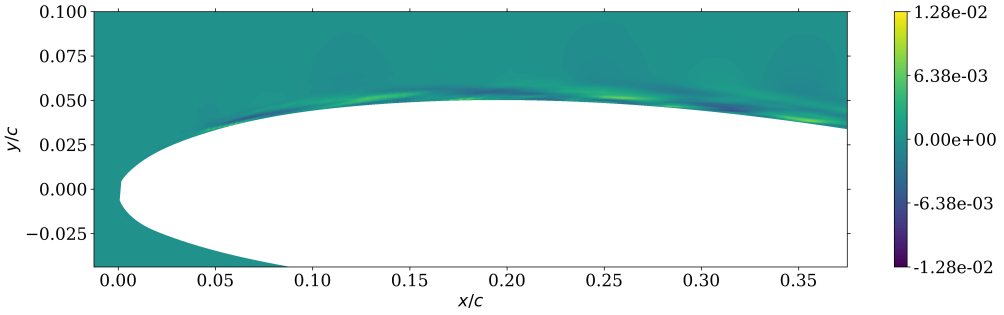

First mode of velocity component u'

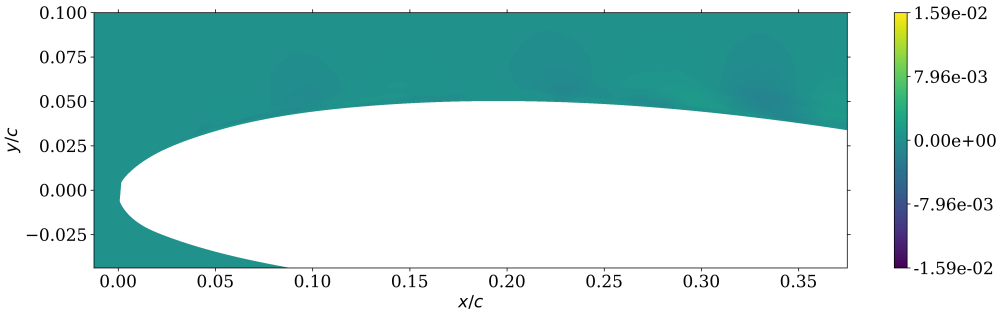

First mode of velocity component v'

Figure 36: Weighted SPOD modes at $f = 568\,\mathrm{Hz}$ near leading edge

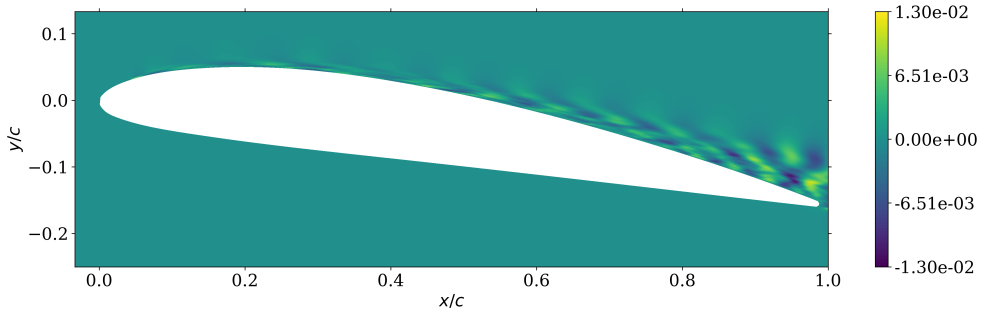

Second mode of velocity component u'

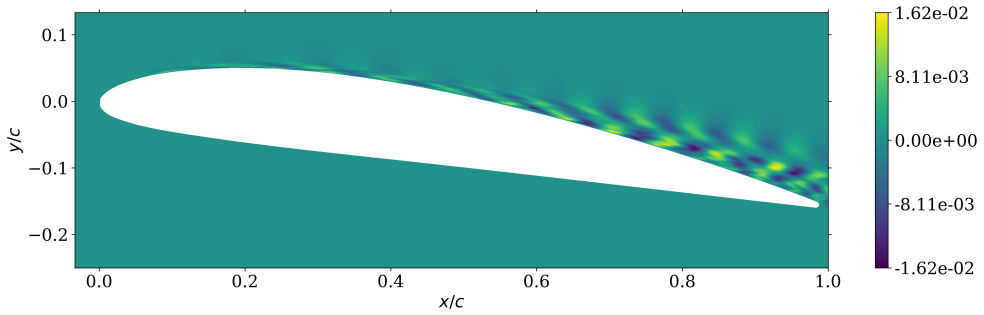

Third mode of velocity component u''

Figure 37: Second and third SPOD mode at $f = 568\,\mathrm{Hz}$

4.3 Resolvent Analysis

This section covers the results of the resolvent-based modeling approach in combination with an eddy-viscosity model. The resolvent analysis is executed on the same range of frequencies up to 1000 Hz, where the most important features are found in the SPOD. The contour plots of the velocity modes are shown to identify shape and location of coherent structures. In addition the gains are considered and shortly the forcing for one frequency is described. Furthermore the scaling of the graphs is adjusted, so that structures in the boundary layer are more clearly visible. Next problems occurring during the simulation are addressed and finally the results are compared with other grid resolutions to guarantee mesh independence of the simulation.

4.3.1 Velocity responses and gain distribution

At first the modes of the first response at frequency $f = 227\,\mathrm{Hz}$ are observed in Figure 38. Coherent structures are visible in the boundary layer on the suction side and in the wake. Wave packets start early at the wall with low amplitude. Downstream the trailing edge the structures are strongly amplified. This is induced by the interaction of the flow from the suction and pressure side. For the streamwise velocity u' the structures are inclined in the wake. In contrast the modes referring to the v' component are almost symmetrical in vertical direction. Moreover for the u' component waves on top of the near wall modes are seen. For a better recognizability the area of the boundary layer on the suction side, where structures start to evolve, is under further investigation. Therefore the boundary layer is shown with

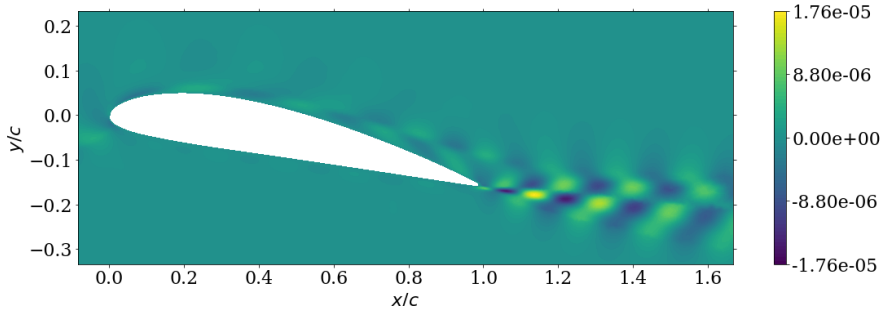

First mode of velocity component u'

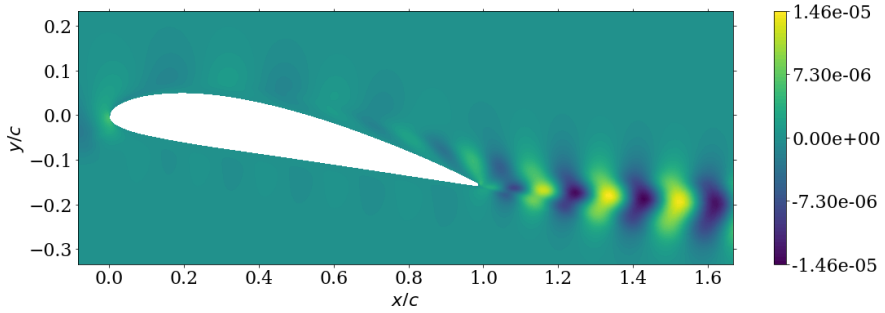

First mode of velocity component v'

Figure 38: Resolvent response modes at $f = 227\,\mathrm{Hz}$

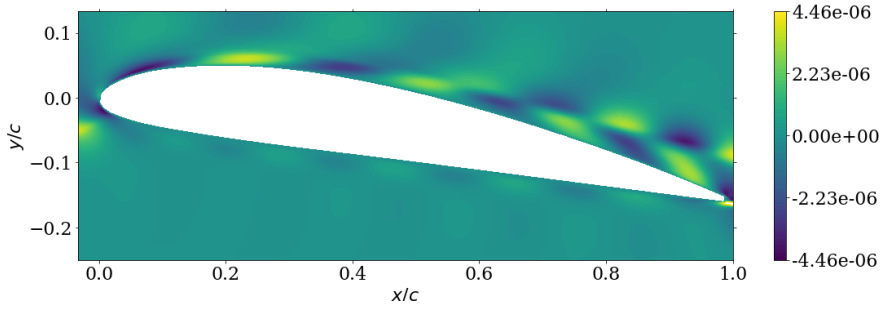

First mode of velocity component u'

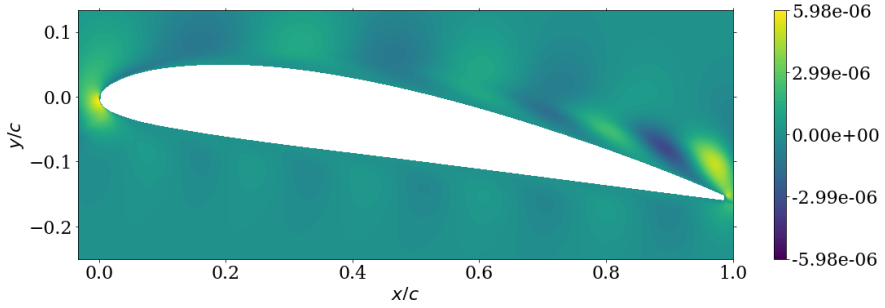

First mode of velocity component v'

Figure 39: Resolvent response modes at $f = 227\,\mathrm{Hz}$ near wall

an adjusted scaling, so that the weaker amplitudes can be seen more clearly in Figure 39. This is accomplished by limiting the scale to the minimum/maximum value of the visible domain. Interestingly this shows that wave packets are already excited at the leading edge of the airfoil and are also present at the pressure side but only faintly. The structures evolving on top of the waves at the wall, induced by shear with the outer flow, are found to begin not directly at the leading edge but at $x/c \approx 0.4$. These coherent structures on the suction side appear as modes with peaks of same intensity for the wall near wave packets and the packets distant to the wall, which is an observation referring to the presence of Kelvin-Helmholtz instabilities.

The solutions obtained by resolvent analysis also include the forcing modes. The forcing associated to the frequency $f = 341\,\mathrm{Hz}$ is shown in Figure 40. A strong forcing mode is coming upstream to the leading edge at the stagnation point. The influence of this forcing mode is also visible in most of the response modes, where a response at the same spot is found. This is already detectable for the earlier response at a lower frequency, where right at the leading edge amplitudes are recognized. Besides forcing modes develop on the suction side at the wall of the airfoil, where the Kelvin-Helmholtz structures are present. In comparison these modes are less energetic.

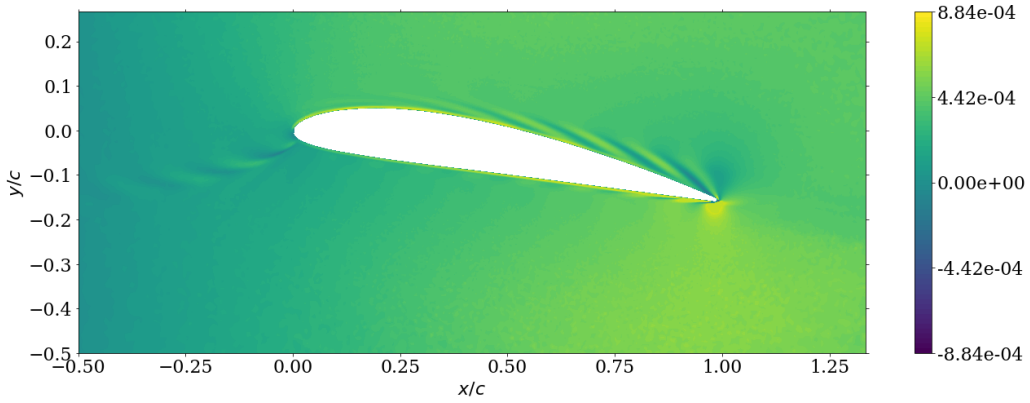

First mode of velocity component u'

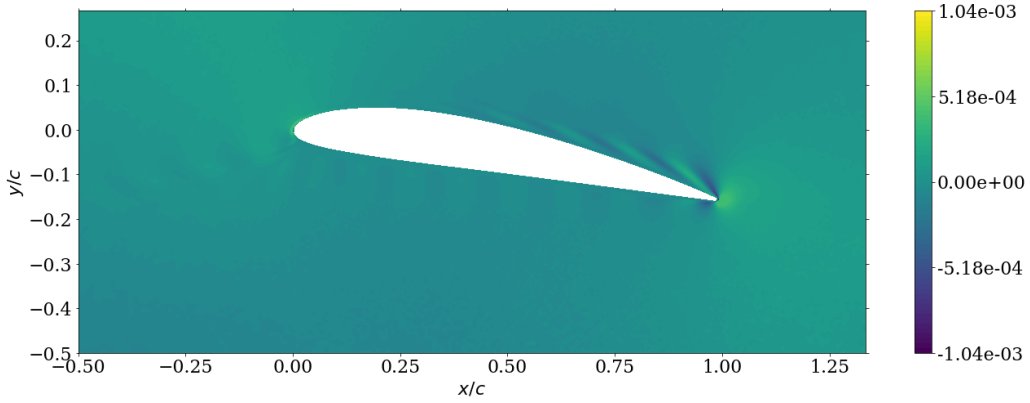

First mode of velocity component v'

Figure 40: Resolvent forcing modes at $f = 341\,\mathrm{Hz}$ near wall

For a higher frequency $f = 568\,\mathrm{Hz}$, which is illustrated in Figure 41, coherent structures

differ in various ways. The wave length of the structures reduces with increasing frequency.

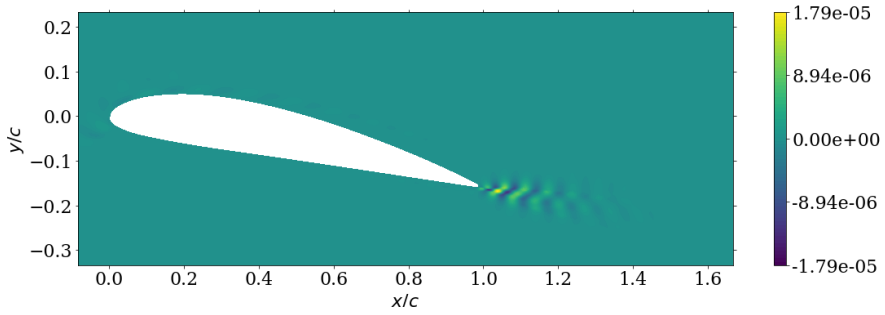

First mode of velocity component u'

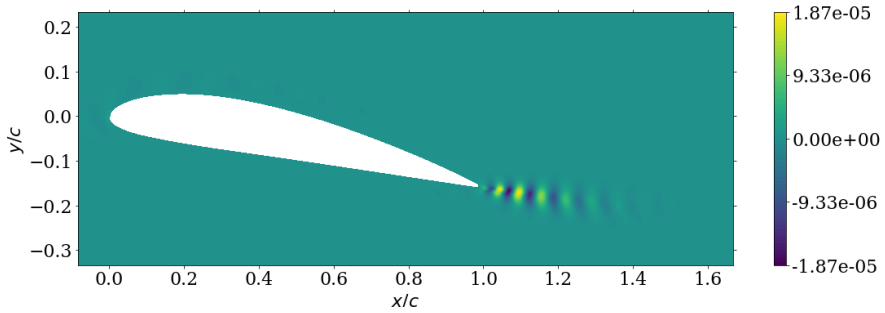

First mode of velocity component v'

Figure 41: Resolvent response modes at $f = 568\,\mathrm{Hz}$

Furthermore amplitudes are only visible after the trailing edge and decrease rapidly in their intensity. Unchanged are the unequal shapes of u' and v' component of the response modes. Next the boundary layer is in focus in Figure 42. Here another mechanism is observed at the walls. The modes are dominant at the leading edge and decrease in amplitude further downstream. This observation indicates that the modes appearing at the start of transition are more energetic for higher frequencies than the Kelvin-Helmholtz structures. The wave packets near the leading edge of the suction side appear with a high amplitude directly at the wall and a smaller peak on top, which probably represent Tollmien-Schlichting waves. These are one major initiator for transition from a laminar to a turbulent boundary layer. The mean flow and total viscosity suggest transition in this area in the input of the resolvent simulation. For the resolvent analysis no explicit tool for the tripping is used, so that transition could be computed as Tollmien-Schlichting waves. But interestingly these structures are stretching far up to the trailing edge edge, which states that they are not only present in the area of transition but remain further downstream. This observation could be caused by the fact that resolvent analysis can hardly capture nonlinear mechanisms. At the start Tollmien-Schlichting waves evolve linearly. Later they are transformed typically by nonlinear effects and dissolve to turbulence. This is not represented here, as the structures maintain their shape.

Next the frequency $f = 909\,\mathrm{Hz}$ is considered in Figure 43. Similar to frequency $f = 568\,\mathrm{Hz}$ dominant structures are only visible downstream the trailing edge, but the wave

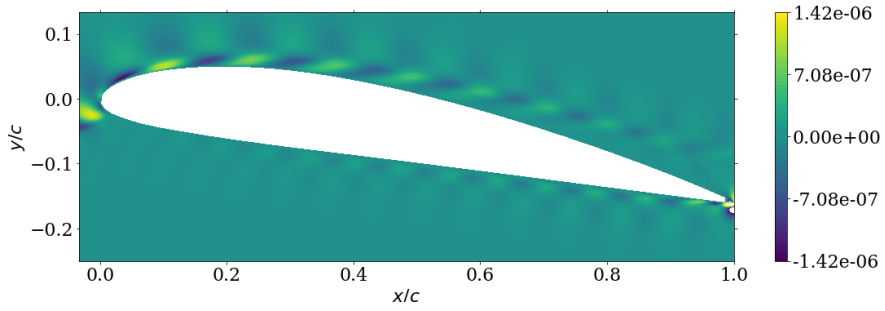

First mode of velocity component u'

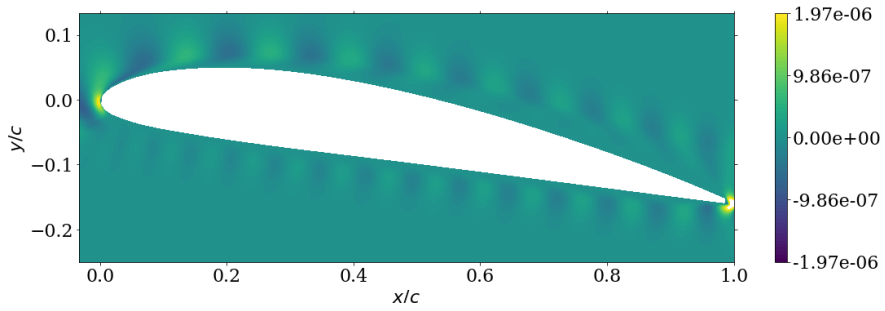

First mode of velocity component v'

Figure 42: Resolvent response modes at $f = 568\,\mathrm{Hz}$ near wall

length shortens furthermore. Proceeding with the structures in the boundary layer in Figure 44 yields also high amplitudes at the leading edge. In addition weak modes at the pressure side start to rise after $x/c = 0.5$ and seem to affect the structures evolving at the trailing edge.

In summary the most amplified structures are visible downstream the trailing edge over all frequencies. Structures at the leading edge are present for all frequencies. For low frequencies Kelvin-Helmholtz structures are observed on the suction side overlapping with the wave packets from the trailing edge, but for higher frequencies they are not recognizable.

Next the gains or eigenvalues associated up to the third mode are presented for the considered frequencies in Figure 45. The gains are peaking for low frequencies. Higher frequencies are almost on the same intensity level. The rise for low frequencies could be caused on the one hand by the larger area affected by the long wave packets for the low frequencies. The coherent structures for high frequencies vanish rapidly behind the trailing edge in contrast to the modes associated to lower frequencies. On the other hand it could be the absence of Kelvin-Helmholtz structures on the suction side for higher frequencies. Therefore the flow appears less energetic.

The gains also show that the magnitude of the eigenvalues is not separated very well. Hence the second and third eigenvalue are taken into account as well. The second and third response of frequency $f = 227\,\mathrm{Hz}$ are illustrated in the boundary layer in Figure 46. The mode shape of the second response does not differ strongly from the first response, but in the third mode the main wave packets are more amplified upstream the trailing edge. This

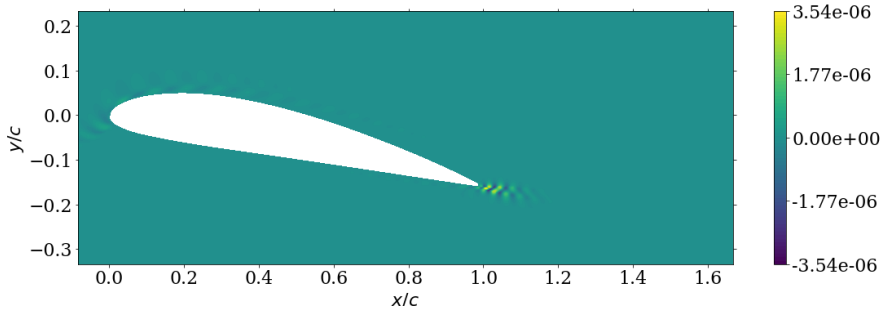

First mode of velocity component u'

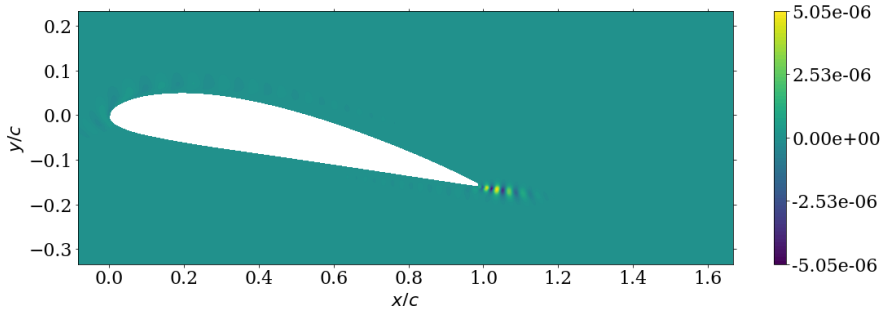

First mode of velocity component v'

Figure 43: Resolvent response modes at $f = 909\,\mathrm{Hz}$

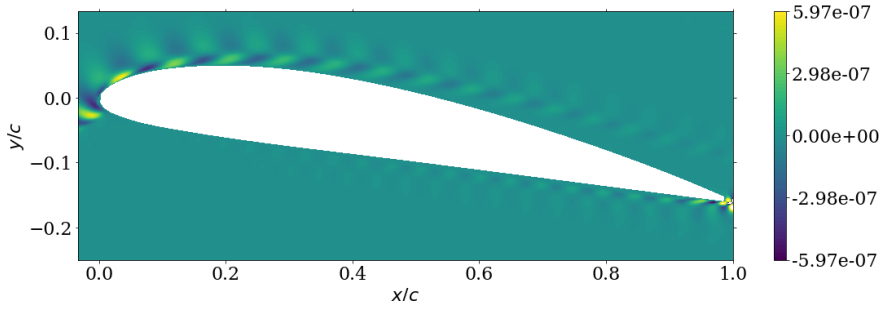

First mode of velocity component u'

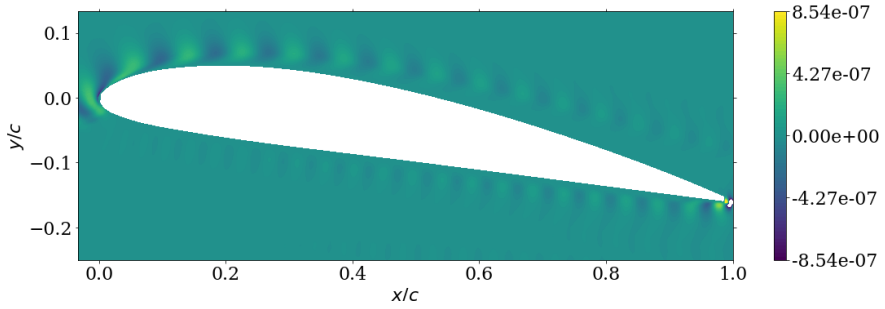

First mode of velocity component v'

Figure 44: Resolvent response modes at $f = 909\,\mathrm{Hz}$ near wall

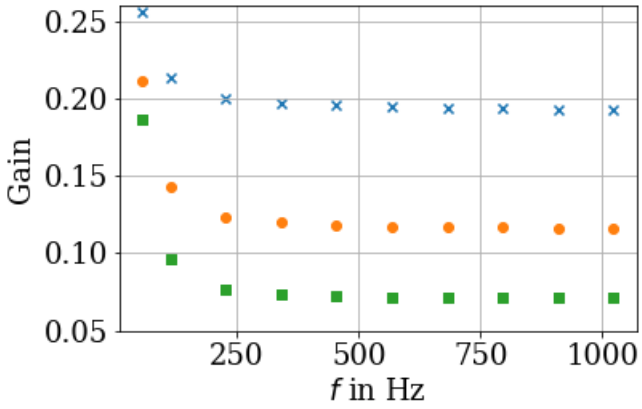

Figure 45: Gain distribution

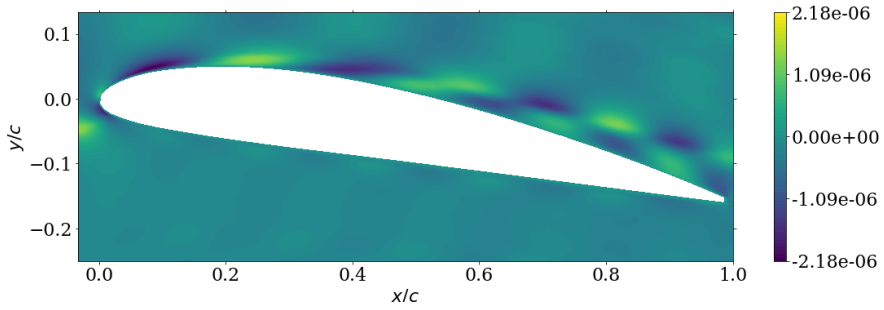

Second mode of velocity component u'

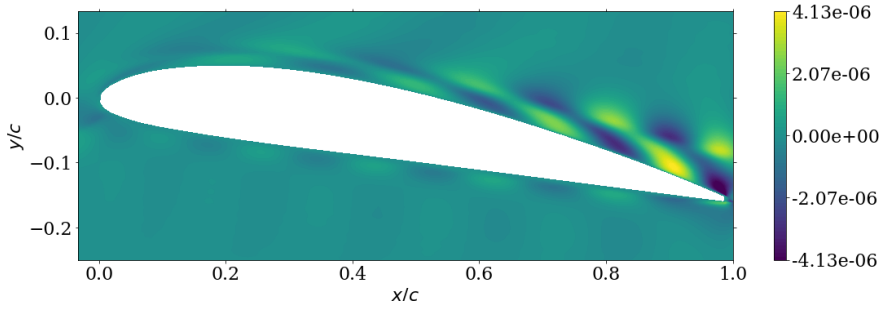

Third mode of velocity component u'

Figure 46: Resolvent response modes at $f = 227\,\mathrm{Hz}$ near wall

yields a promising observation for further comparison between SPOD and resolvent in the means of evolving Kelvin-Helmholtz instabilities.

4.3.2 Pressure responses and simulation issues

While the velocity modes appear very consistent in their physical behavior, unfortunately abnormal features are included in the pressure response. Areas of a pressure offset are found, which are not physically explainable. These disturbances are shown in Figure 47. Through different grid sizes and boundary conditions this effect could not be dissolved. Finally the sponge layer was replaced by a constant total viscosity without succeeding in removing these unusual features. Although the pressure response is reasonable, when the high values in the background are neglected. This is leading to the conclusion that the nonphysical phenomenon of the high pressure area should not impact the shape of the velocity responses severely, although it needs further investigation in future works. Furthermore the gain distribution is probably impaired by the high value of the nonphysical offset, which contributes to the magnitude of the corresponding eigenvalue. Hence the structures at the airfoil are not the only source for the rise in the eigenvalues and can not be solely associated to amplification in the gain.

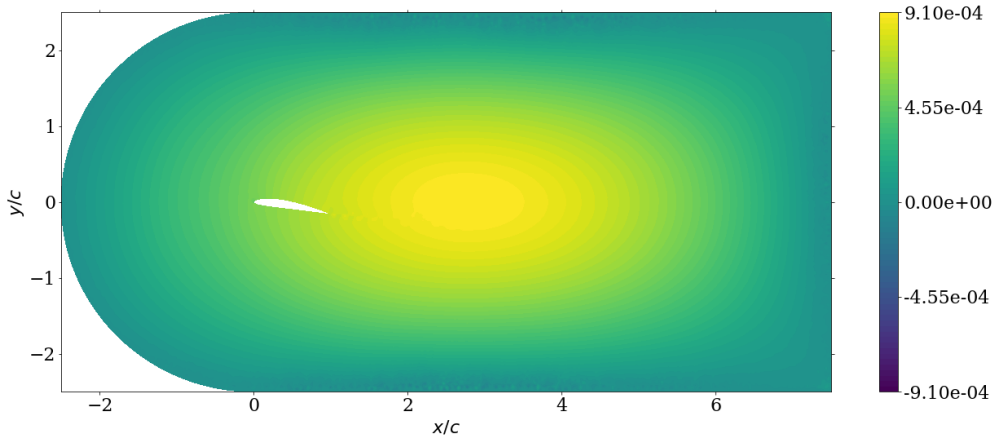

First mode of pressure component p'

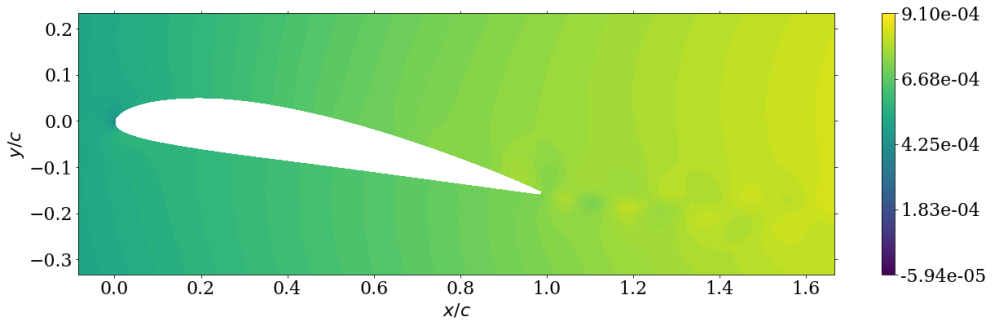

First mode of pressure component p'

Figure 47: Resolvent response modes at $f = 227\,\mathrm{Hz}$ near wall

In addition although different boundary conditions are used and a sponge layer is applied problems also occur at the far-field region in the forcing of the velocities. But these perturbations vanish in the inner domain and should not have influence on the area of interest at the airfoil.

4.3.3 Mesh independence

To guarantee mesh independence of the presented results, simulations are conducted for three different mesh resolutions. The modes of the first response modes of u' at a frequency of $f = 227\,\mathrm{Hz}$ are shown in Figure 48. Deviations between the simulations are small, as the responses appear almost identical. Hence the flow field is well resolved in the results.

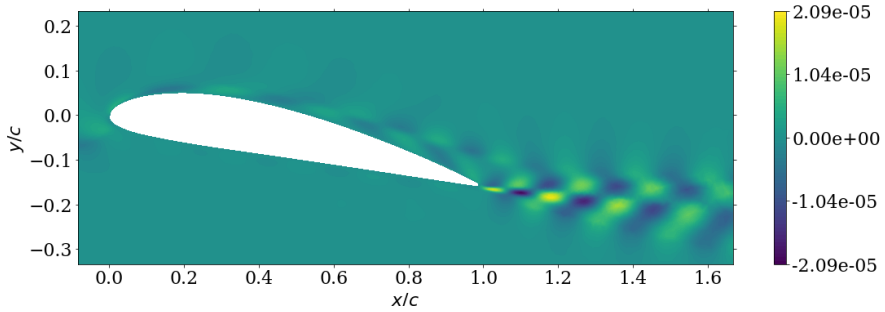

Coarse mesh $\approx 210,000$ cells

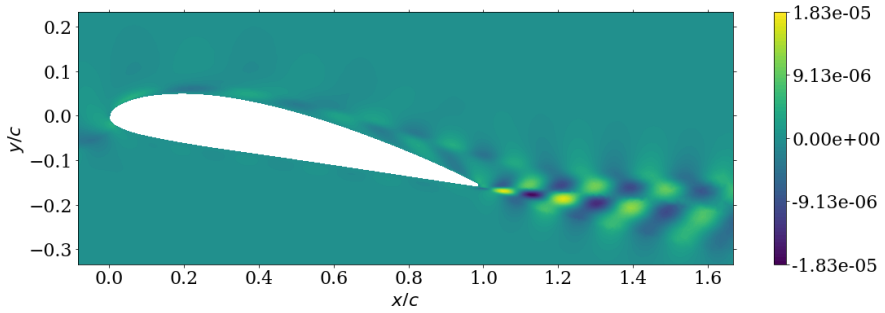

Intermediate mesh $\approx 260,000$ cells

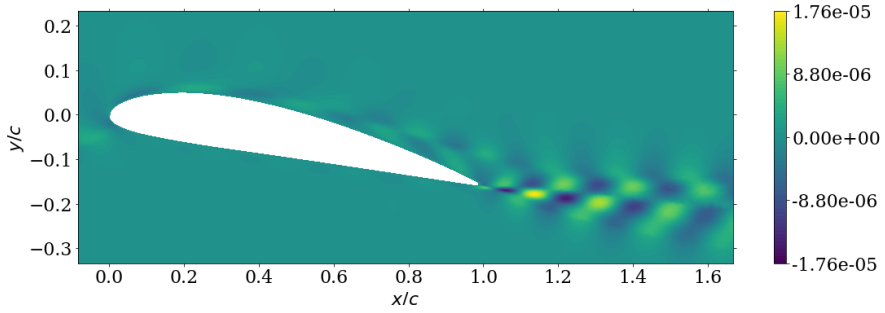

Fine mesh $\approx 310,000$ cells

Figure 48: Mesh independence: First mode of velocity component u' at $f = 227\,\mathrm{Hz}$

Furthermore the gain of the different meshes is shown in Figure 49. Very good agreement

is reached here. For frequencies above $f = 200\,\text{Hz}$ the slope is very similar. For the lowest frequencies the general feature, i.e. high gain which is declining rapidly by increasing frequency, coincides.

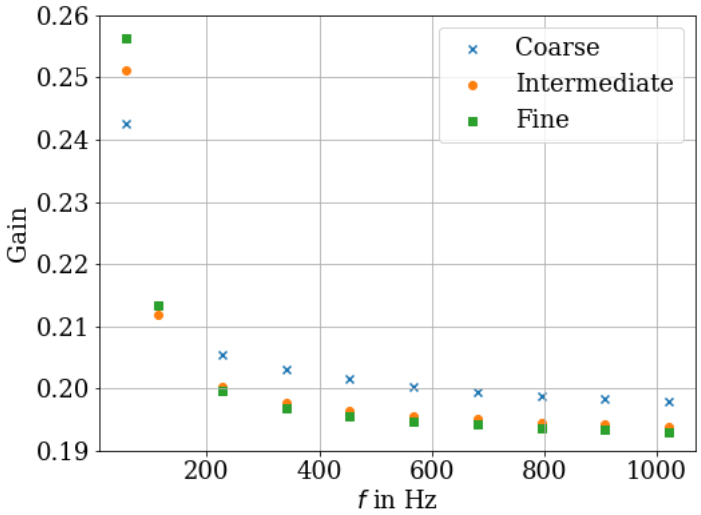

Figure 49: Mesh independence: Gain distribution

4.4 Comparison between SPOD and Resolvent Analysis

Eventually the results of the SPOD based on the LES are compared to the results of the modeling procedure, the resolvent analysis. For this at first the mode shapes at the same frequency are examined. For the analysis of the boundary layer the second and third mode of the SPOD and resolvent are also considered, as the eigenvalues are not highly separated and high energetic coherent structures are also contained in these modes. Furthermore quantitative investigations are performed by interpolation over lines in the boundary layer normal to the wall. As a turbulent boundary layer is the object of interest an exact agreement between resolvent and LES is not expected. From the investigations of the resolvent modes the appearance of structures in the boundary layer near the trailing edge are only visible for low frequencies, so that the focus in the comparison lies on these modes as well. Unfortunately the SPOD results, due to the short duration of the simulation, are not yet completely "converged" for low frequencies and therefore appear blurred for some features, which makes interpretations difficult in parts.

4.4.1 Contour plots

The appearance of Kelvin-Helmholtz structures in both results for frequency $f = 227\,\mathrm{Hz}$ makes this the first target for comparison of the mode shapes. Therefore the velocity components are shown for SPOD and resolvent in Figure 50 in respect to the first mode. The scale of the graphs is adjusted, so that for each plot the visible area is scaled in between the highest and lowest value corresponding to each result.

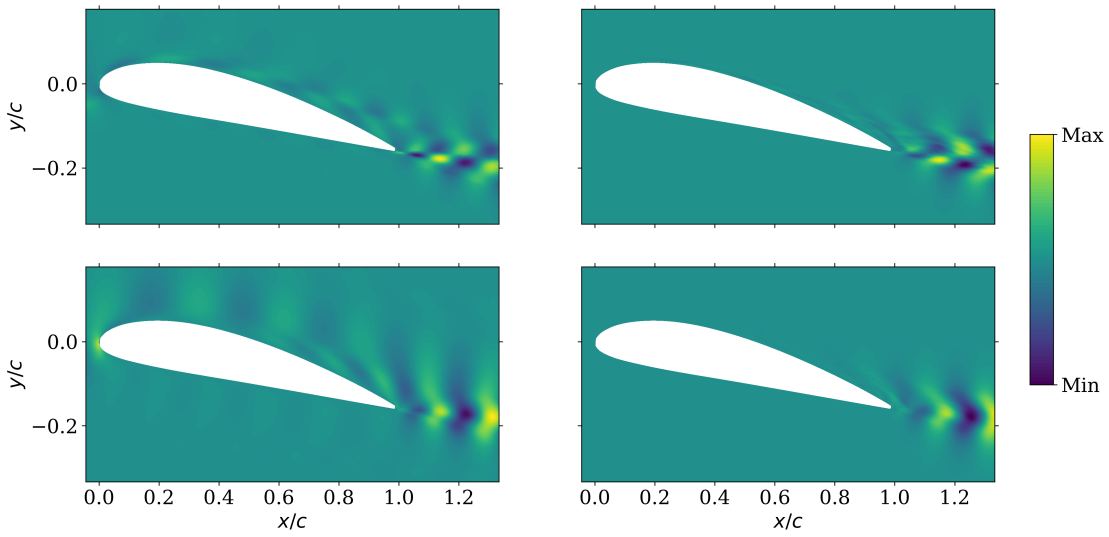

Figure 50: First velocity modes at $f = 227\,\mathrm{Hz}$, left: resolvent, right: SPOD, top: u', bottom: v'

In the wake the shape of the modes of both simulations are almost equal for the velocity components u' and v'. For both results the most energetic structures emerge in the wake,

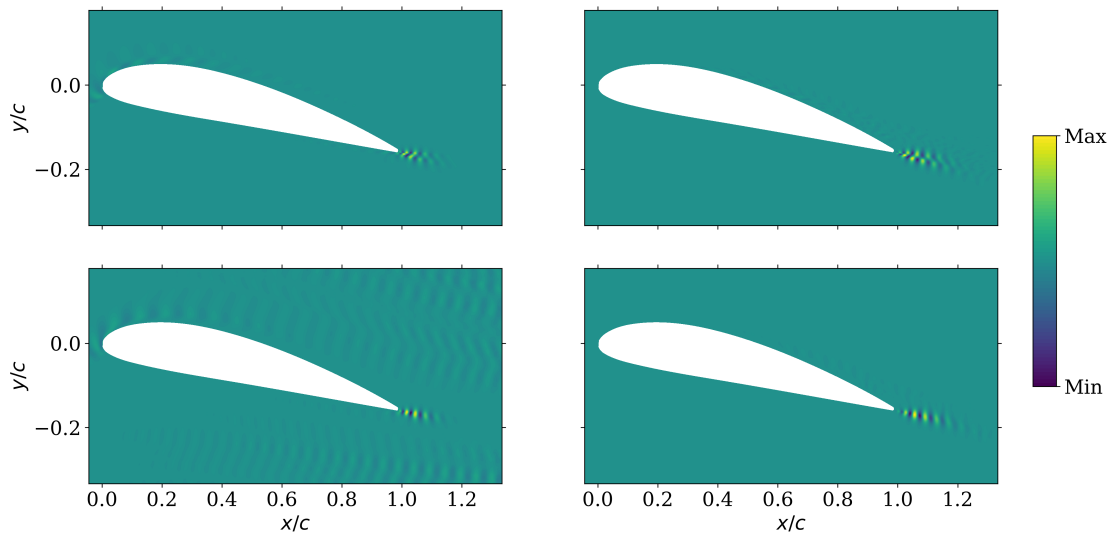

Figure 51: First velocity modes at $f = 909\,\mathrm{Hz}$, left: resolvent, right: SPOD, top: u', bottom: v'

where suction and pressure side meet. In the resolvent modes coherent structures appear earlier. They are already visible at the leading edge, so that these wave packets are at least nearby the magnitude of the highly amplified structures in the wake. In comparison the LES shows weak structures in the boundary layer, which can only be detected near the trailing edge.

For a higher frequency of $f = 909\,\mathrm{Hz}$ the most energetic structures appear in the wake right at the trailing edge for both cases. The shape of the modes are very much alike. The only difference existing is the faster decline of the amplitudes in the wake for the resolvent modes. Furthermore the presence of low amplitude structures at the leading edge are only visible for the resolvent results.

In the next step the modes in the boundary layer are in focus. The modes of the first, second and third rank are presented in Figure 52 for $f = 341\,\mathrm{Hz}$ for the streamwise component.

Over the whole suction side of the resolvent mode wave packets are found. The structures appearing by transition and the Kelvin-Helmholtz structures are overlapping. The SPOD does not represent structures of significant amplitude at the leading edge for low frequencies. This observation refers to the different type of transition in the resolvent simulation and the LES. In the LES transition is triggered by the tripping element at the leading edge on the suction side. As the element is constructed by a momentum source term that achieves zero velocity in the cells of the tripping element, the effect should also be present in the mean flow, which is an input of the resolvent setup. Nevertheless the LES grid refinement at the wall is considerably higher than the refinement in the resolvent, hence the tripping is not resolved accurately in the resolvent. Therefore instabilities involving low frequency structures are possible in the resolvent. In contrast the trip in the LES mainly induces structures of high frequency. Besides Figure 52 shows a match for coherent structures evolving at $x/c = 0.5$,

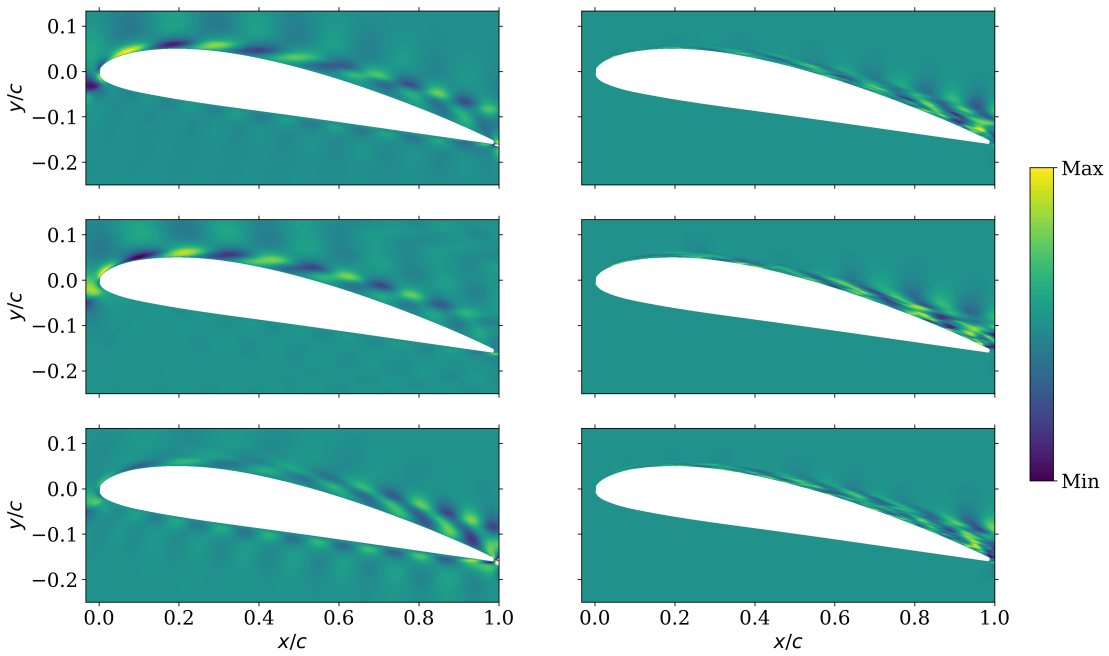

Figure 52: Comparison of velocity component u' at $f = 341\,\mathrm{Hz}$ in the boundary layer

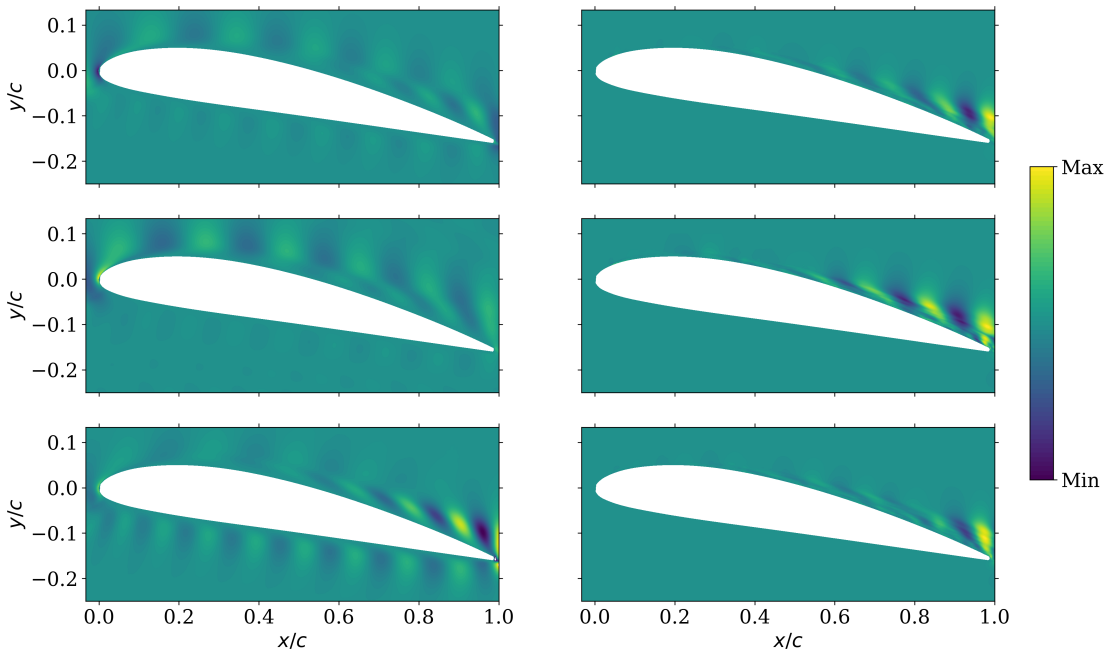

Figure 53: Comparison of velocity component v' at $f = 341\,\mathrm{Hz}$ in the boundary layer

when the first SPOD mode and third resolvent mode are compared. The noise contained in the SPOD modes complicates the interpretation, but the conclusion is confirmed by observing the v' component at the same frequency in Figure 53. There the agreement on the suction side between first SPOD and third resolvent mode is clearly recognizable. In the first and second mode of the resolvent the structures are difficult to distinguish due to the simultaneous presence of wave packets at the leading edge, but in the third mode those structures reduced in intensity. As in the SPOD the shape of all three modes are very similar, the third mode of the resolvent fits to all three SPOD modes. Although the transition appears to behave in different means, similar Kelvin-Helmholtz structures are detected in both, the resolvent and LES results. In addition the third mode of the resolvent reveals other weak structures along the pressure side. As the LES flow stays laminar on the pressure side no structures are detected there.

In order to show that not only for frequency $f = 343\,\mathrm{Hz}$ but also for other low frequencies there are modes of resolvent and SPOD that are consistent upstream the leading edge, the same configuration of the first, second and third mode is illustrated in Figure 54 for the v' component at frequency $f = 453\,\mathrm{Hz}$. Yet for this frequency structures evolving at the leading edge become the most dominant source for the first and second mode in the result of the resolvent, whereas the main feature in the SPOD are the Kelvin-Helmholtz modes significant downstream $x/c = 0.3$. But in the third mode of the resolvent, structures coinciding with the shape of the modes of the SPOD are detected. Again the modes of the SPOD are blurred but the similarity is still recognizable.

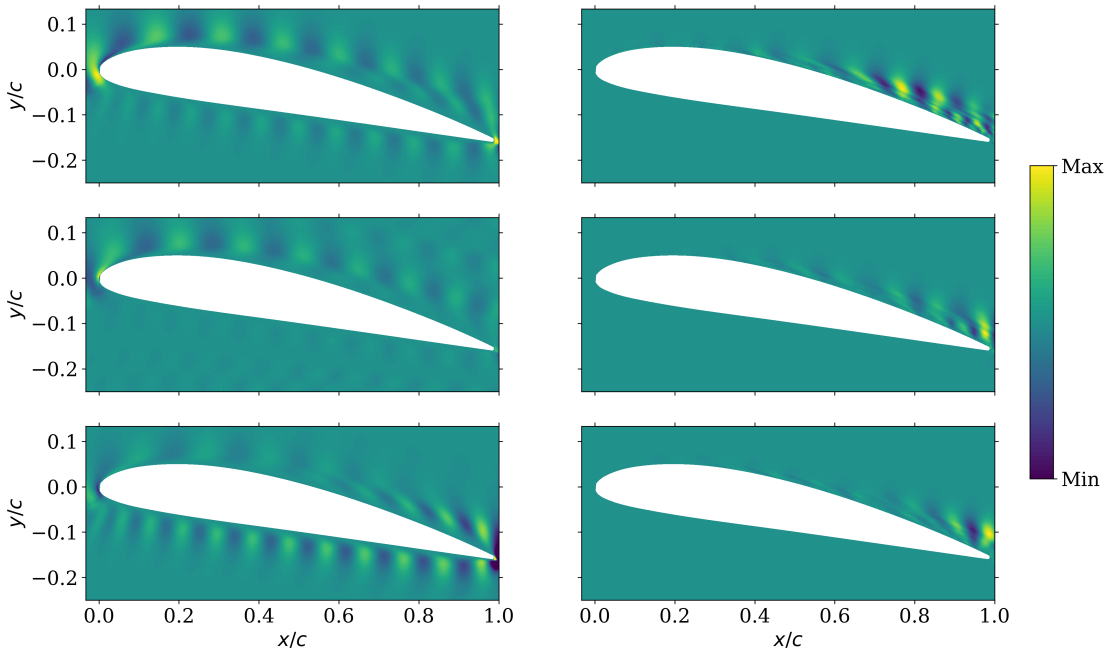

Figure 54: Comparison of velocity component v' at $f = 454\,\mathrm{Hz}$ in the boundary layer

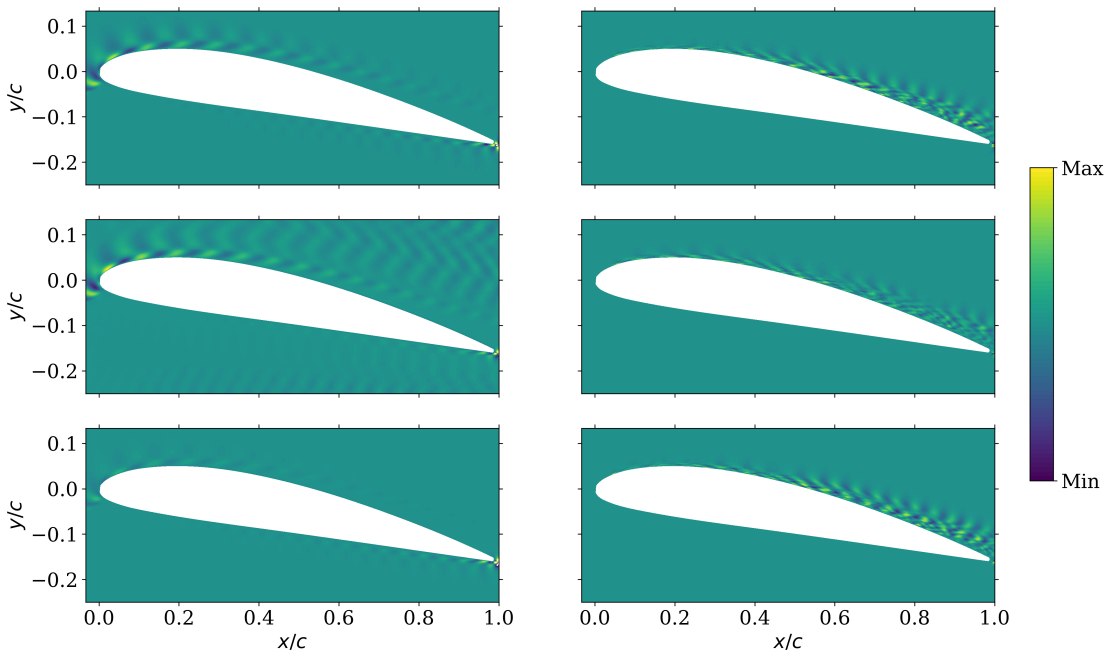

Figure 55: Comparison at $f = 909\,\mathrm{Hz}$

To complete the analysis also structures of frequency $f = 909\,\mathrm{Hz}$ are observed. The most energetic structures differ a lot. The results of the resolvent shows structures evolving at the leading edge, which separate from the wall at $x/c = 0.4$. No structures at the wall upstream the trailing edge are detected, whereas this is the region, where wave packets for the SPOD are found. But interestingly the structures in the SPOD contain a wave packet on top of the wave packet directly at the wall. This structures seem to be similar to the structures, which are evolving in the resolvent right at the leading edge but are separating from the wall right where the SPOD wave packets begin.

As the comparison of the contour plots shows good agreement between different ranked modes especially for low frequencies those frequencies are further inspected next.

4.4.2 Profile of the magnitude of the mode

The results of SPOD and resolvent are represented by a complex mode. The phase of the modes can be shifted between SPOD and resolvent results. Therefore the magnitude of the complex values are considered in the velocity profiles. In addition the velocity is split into a wall tangential component u'_t and a wall normal component u'_n. Former investigation of the contour plots presented that a good fit between the results can be observed between modes of different ranks. As the modes of the SPOD are mostly similar for the first modes only the first mode is necessary in this case. But as the resolvent modes illustrate different features, the first three modes are displayed. The frequency $f = 343\,\mathrm{Hz}$, which shows good agreement between SPOD and resolvent in the former investigations, is further analyzed. At

the y-axis y_n describes the wall distance at the point in the profile. All observed profiles are on the suction side as in the SPOD a turbulent boundary layer only evolves on this side of the airfoil. The first profile is located at $x/c = 0.23$ and shown in Figure 56. First of all

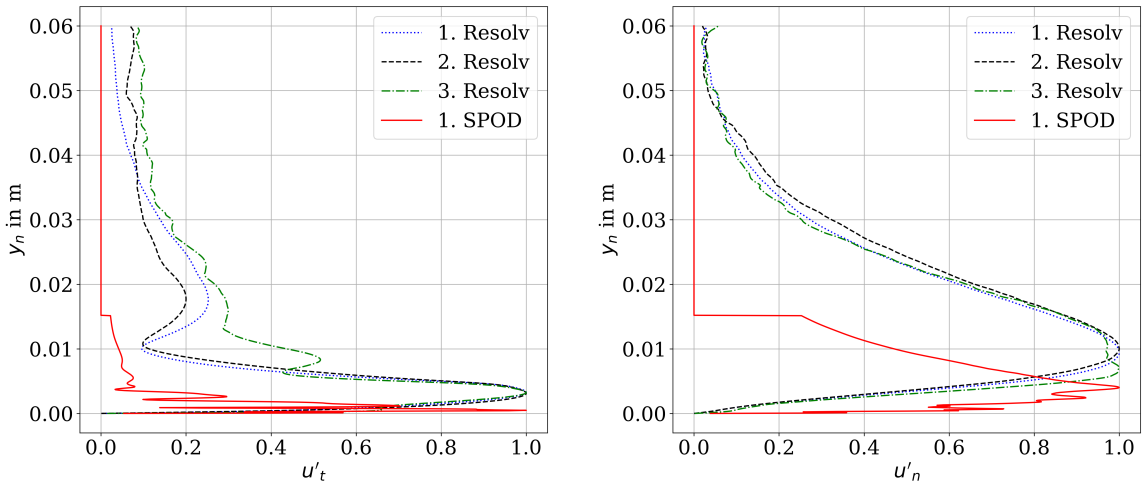

Tangential velocity component u'_t Normal velocity component u'_n

Figure 56: Velocity profiles at $x/c = 0.23$ for frequency $f = 343\,\mathrm{Hz}$

the SPOD profile appears very noisy, which is observed in most of the other profiles as well. Furthermore the abrupt step to zero in the SPOD profiles is due to the size of the domain used in the SPOD, which stops there. From the contour plots it is already concluded, that different transition behavior are present in resolvent and LES, therefore the profiles are not matching to each other very well. But interestingly the tangential velocity profiles of the first and second mode of the resolvent shows the typical features of Tollmien-Schlichting waves with a first high peak followed by a smaller second peak, which is confirming the observations in the contour plots of the resolvent modes.

Proceeding with the next location at $x/c = 0.77$, the third mode of the resolvent and the SPOD mode are showing good agreement in the normal component u'_n. Still the SPOD mode appears noisy, but the overall shape is very close and the location of the peak matches perfectly. Furthermore the first resolvent mode peaks at the same location as the third resolvent mode, but afterwards increases for a second peak. Possibly the first mode is still affected by the coherent structures from the leading edge at this location, which do not emerge in the LES. But this influence is only present in further distance to the wall, which was observed by the separation of the structures from the wall. Because of the noise an accurate interpretation is not possible for the tangential component.

The last location on the airfoil at $x/c = 0.95$ shows again a good match between the third mode of the resolvent and the first SPOD mode. The first mode of the resolvent predicts the peak also well and the intensity of the second peak declines in comparison to location $x/c = 0.77$, so that deviation starts only at $y_n = 0.02\,\mathrm{m}$.

Although the focus of this thesis lies on the structures evolving in the boundary layer the wake profiles are presented next (Figure 59). Here the y-axis is associated to the location in

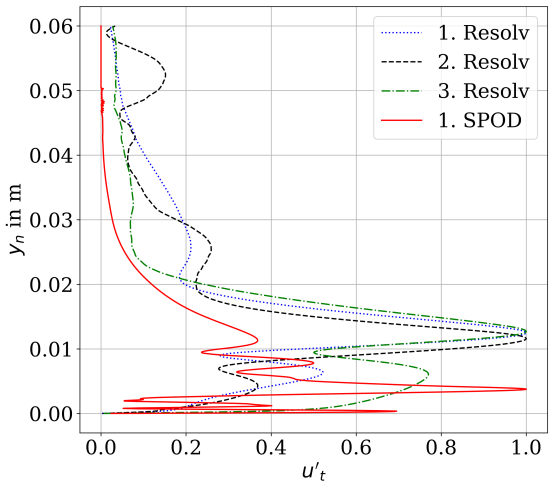

Tangential velocity component u'_t

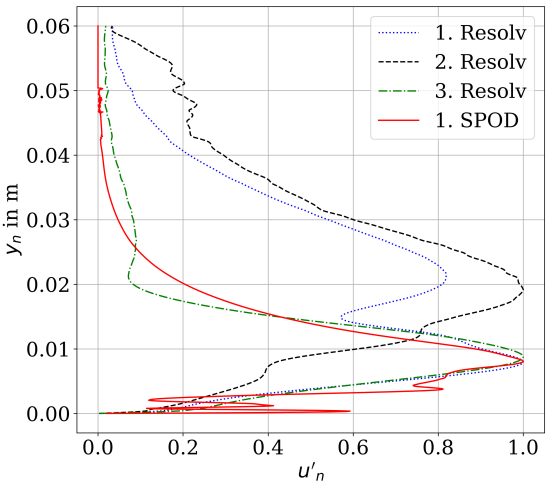

Normal velocity component u'_n

Figure 57: Velocity profiles at $x/c = 0.77$ for frequency $f = 343\,\mathrm{Hz}$

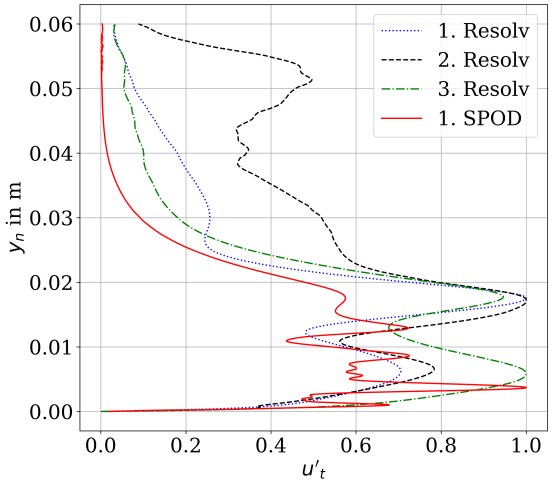

Tangential velocity component u'_t

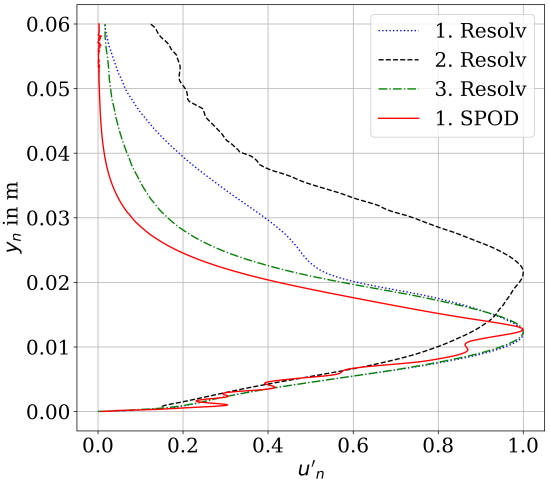

Normal velocity component u'_n

Figure 58: Velocity profiles at $x/c = 0.95$ for frequency $f = 343\,\mathrm{Hz}$

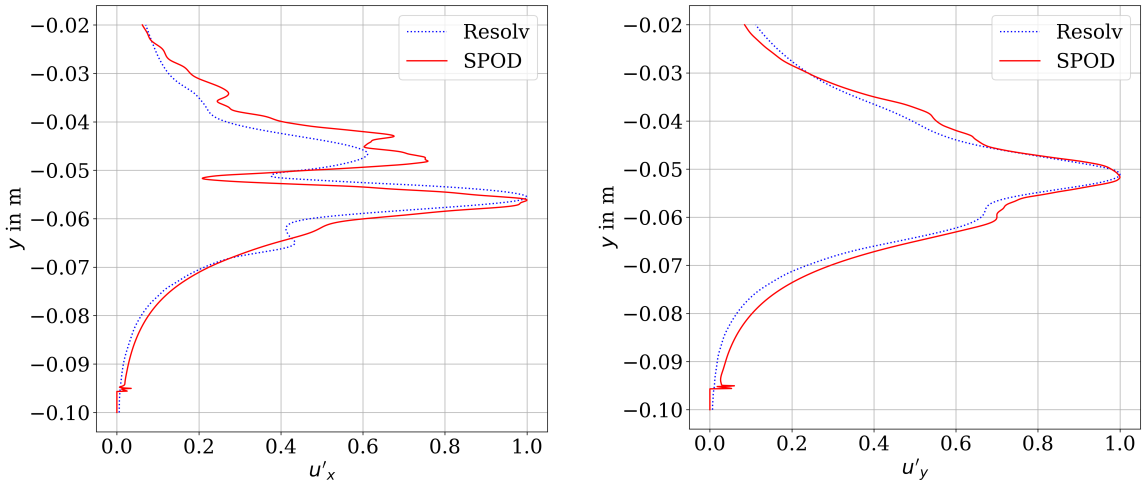

Streamwise velocity component u'_x Vertical velocity component u'_y

Figure 59: Velocity profiles at $x/c = 1.2$ for frequency $f = 227\,\mathrm{Hz}$

the domain and the velocities in streamwise and vertical direction are considered. Already in the contour plots a very good agreement of the mode shapes in the wake is observed for frequency $f = 227\,\mathrm{Hz}$. This is confirmed by the velocity profiles. The vertical velocity component u'_y is matching almost perfectly. Furthermore the tangential part is also in good agreement and has the same overall shape for both results.

Concluding from the comparison very good matches occur for low frequencies. But also the general flow features presented in the SPOD are matching well in the resolvent, as the amplified structures in the wake are observed in both results and the velocity profile matches almost perfectly in the wake. But the problematic feature stays the transition, i.e. the area downstream the leading edge in the suction side, which needs further discussion in the next chapter.

5 Discussion

As already stated a turbulent boundary is investigated in this work, therefore no exact match in the comparison of the results is expected. Considering this the results of the resolvent are in good agreement with the coherent structures arising after the transition in the LES. The resolvent analysis as a method of reduced-order modeling is not respecting the nonlinear terms of the Navier-Stokes equations in their original form but modeling them in an unstructured way. Yet the modeling approach succeeds in the prediction of Kelvin-Helmholtz modes, which are firstly detected in the LES data by SPOD and are also present later in the resolvent modes of low frequency. This concludes that the mechanism in the development of the structures is driven by linear behavior as the accurate representation of highly nonlinear mechanisms by the resolvent is doubtful. Furthermore the wave packets in the wake are matching almost perfectly and the general feature of highly amplified structures in the wake is displayed equally in both simulations.

The SPOD and resolvent results coincide in some aspects, but they also differ in others. Here possible reasons for this deviations are discussed, which are implied by the modeling procedures or the specific setup of the simulations in this thesis. Thereby adjustments to improve results in further research are suggested.

Major differences in the results of the SPOD and resolvent are found near the leading edge, where the resolvent shows high amplitudes already for a frequency of $f = 227\,\mathrm{Hz}$. In the SPOD high energetic structures at the leading edge emerge only in the area of the trip for much higher frequencies above $f \approx 3500\,\mathrm{Hz}$. As already discussed in Section 4.4.1 the type of transition differs for the LES and resolvent simulation due that the tripping is realized differently. But considering the amount of cells needed for the refinement at the wall for an exact embodiment of the LES setup, the calculation of the eigenvalue problem would be unfeasible. The limit of maximum cells is already reached by the used mesh with the available resources. In fact through the thickening of the boundary layer in the mean flow the resolvent input indicates transition but the exact type of transition is not communicated. Through the representation of the nonlinear parts of the Navier-Stokes equations as an unstructured forcing in the resolvent approach, the modeling of highly nonlinear effects in the flow appears questionable. Indeed the resolvent result shows the sign of Tollmien-Schlichting waves, which can be modeled well by linear approaches as the e^N-method, emerging from linear stability analysis. Maybe other tripping procedures could be used for the resolvent setup to present the same setup as in the LES. For instance a high viscosity ν_{tot} could be introduced at the location of the trip. Then it would be explainable if the resolvent approach can not satisfy nonlinear effects in this area or just the issue of an unequal setup leads to the disagreement.

Another distinction between both methods is concerning the Kelvin-Helmholtz structures, which are not present in the resolvent for high frequencies. In contrast the highly amplified modes in the wake fit very well. Therefore the Kelvin-Helmholtz structures could already be present in the resolvent result, but are included in the modes of lower order, as structures that are evolving on the suction side should have a huge influence on the wave packets in the wake. The high amplitude of the modes at the leading edge could lead to the fact that the

Kelvin-Helmholtz structures are only present in lower ranked modes. As the contour plots show good agreement between the third mode of the resolvent and the modes of the SPOD for low frequencies, this is already observed in the data. Besides the structures for higher frequencies could be more dependent on nonlinearity and therefore are not well captured by the resolvent.

Furthermore the numerical setup and results of the LES are discussed, as imperfect features impact the correct comparison of coherent structures tremendously. In general the LES results seem valid. In the validation and the investigations of the flow in the boundary layer the LES results are accurate. In addition the consensus of LES and resolvent for many features affirms the proper behavior. Differences can be explained, as a consequence of the resolvent approach and the tripping method, as described above. A major aspect affecting the comparison and the calculation of the SPOD is the short duration of the simulation. Unfortunately longer simulation time could not be accomplished due to the limited time for this thesis. More snapshots of the data would yield a more "converged" state of the spectrum and SPOD, which would improve especially the comparison of the velocity profiles between resolvent and SPOD. Still other issues remain open for the LES. Another aspect, which has not been studied in this work, is the effect of the mesh or mesh independence. For more reliance on the computed data, mesh refinement in the zone around the airfoil would be pursued in order to verify the results. Thereby the range of resolved structures in the flow would be widened as well. The power density spectrum of the flow in the boundary layer in Figure 24 states that the mesh resolves structures only up to the start of inertial subrange. This leads to good results, but further refinement may improve the simulation. Furthermore during the construction of the final LES setup two different Smagorinsky models are tested. The dynamic Smagorinsky model as proposed by Germano/Lilly is used in this thesis, as it was liable in many earlier studies, and yields a better fit to the validation data in comparison to the dynamic Lagrangian Smagorinsky approach. Nevertheless some incorrect behavior is found in the results of the LES, which are illustrated in Figure 23. Negative viscosity values in the mean flow are observed in areas, where no turbulence is expected. Bad interaction between the Smagorinsky model and the mesh resolution leads to these effects, but as the overall results are accurate the influence on the main flow at the airfoil is limited. For the dynamic Lagrangian approach such kind of perturbations do not occur due to the more sophisticated averaging procedure of the Smagorinsky coefficient C_s. This suggests the use of other models for further investigations to overcome this problems. As the search for better, more accurate models is still a current topic, many other model approaches are possible. In addition not only the effect of the tripping in the resolvent could be adjusted but in the LES setup as well. The tripping of the boundary layer worked well, as the beginning of transition is excited accurately. But in the power density spectrum bumps are observed, which possibly are the result of the trip. The trip may induce perturbations stretching through most of the boundary layer and causing historic effects. On the contrary in the SPOD modes of high frequency the structures induced by the trip decline rapidly after the tripping element. But as these modes refer to a frequency of one magnitude higher than the observed bump in the spectrum, large scale structures induced by the trip could still be the source of perturbations.

In the setup of the LES a different kind of tripping could be implemented to analyze the effect, which is induced by the tripping element, in comparison to other boundary layer tripping methods. Thereby the presence of historic effects by the trip used in this thesis could be explained. Further a smaller tripping element could be tested. As the trip used in this thesis is conservatively designed to force transition inescapably, which may cause the historic effect just due to the large size. Furthermore additional validation data is necessary for a more reliable validation of the LES.

Next the resolvent analysis and the results are further investigated. The results of the resolvent approach are reasonable, when compared to the SPOD. Good agreement in the boundary layer upstream the trailing edge are reached for low frequencies, which supports further use of resolvent in flows with a broadband spectrum. Nevertheless improvements are sought for some nonphysical behavior. The excitement of the response upstream the airfoil is odd. The flow upstream the airfoil should not contain any fluctuations. Probably the low viscosity and therefore the high Reynolds number in front of the leading edge is causing issues. At least this effect can be traced back to the high forcings in the inflow. By observation of the mean velocity fields no conspicuous features are visible, but the mean turbulent subgrid viscosity ν_t, which is also implied in the total viscosity ν_{tot} shows peculiar values at the leading edge. A small increase before the leading edge is seen in Figure 23. Potentially this could have an effect, but as the eddy viscosity computed by the Reynolds stresses is considerably larger, it may not be the initiator. Besides the offset in the pressure response should not be present in the simulation. Several tests did not lead to success in this regard. At first the mesh has been altered in total domain size and overall refinement, but the problem remained. Next the sponge layer was deactivated, which was not removing the pressure perturbation as well. Finally different types of boundary conditions were applied, which could not affect the result. Further investigation have to be undertaken to solve the issue. As mentioned for the results, although the sponge layer is used for the total viscosity ν_{tot}, small perturbations in the forcing appear at the far-field. This could be prevented by allowing only a forcing near the airfoil, where fluctuations are excited physically.

6 Conclusions

Coherent structures evolving in the turbulent boundary layer are of major interest for the control of flow characteristics, for instance noise emission. This work covered the examination of coherent structures for an airfoil with a high Reynolds number, where the LES results showed a high pressure gradient on the suction side. Furthermore the two-dimensional resolvent-based modeling approach yielded a very good match with the SPOD in parts, which concludes that resolvent analysis is capable of modeling emerging coherent structures in the boundary layer for a broadband flow. In addition the resolvent analysis, even though it is representing the nonlinear terms in an unstructured way, leads to a good prediction of the evolving coherent structures upstream the trailing edge for low frequencies, which supports the assumption that the instability mechanism is mainly of linear nature.

Overall the results of the undertaken wall-resolved LES showed reasonable behavior in the examined flow features. The validation data was in overall good agreement with the conducted LES. Transition occured only on the suction side as predicted by *XFoil*. In addition the boundary layer has been sufficiently resolved as the velocity profiles matched the universal laws in the boundary layer mostly well despite the presence of a high pressure gradient on the turbulent suction side. Through SPOD, applied on the LES snapshots, Kelvin-Helmholtz modes were found in the turbulent boundary layer, after the flow passes the tripping element. Most dominant structures resolved by the SPOD were wave packets downstream the trailing edge, where turbulent suction side and laminar pressure side interact. For high frequencies above $f = 3500\,\mathrm{Hz}$ structures evolving at the tripping element were the most energetic fluctuation in the flow.

Furthermore, with the mean flow of the LES as the input, resolvent analysis combined with an eddy-viscosity approach was performed. To dampen perturbations in the far-field, a sponge-layer has been applied for the viscosity, so that a high total viscosity ν_{tot} was presented at the boundary in the far-field. The modes of the resolvent simulations resulted in high amplified modes in the wake, which is consistent to the SPOD. Kelvin-Helmholtz structures were also detected on the suction side, but only appeared as a dominant flow feature for frequencies below $f = 500\,\mathrm{Hz}$. In addition strong instabilities emerged at the leading edge, which were dominant for frequencies above $f = 500\,\mathrm{Hz}$ and were already present at lower frequencies.

The investigations on the velocity profiles in the wake leaded to a very good agreement in the obtained results of both simulations, the LES and the resolvent-based modeling. Furthermore the contour plots showed a decent match in shape and location of the Kelvin-Helmholtz structures upstream the trailing edge observed in both approaches. Hence the instability mechanism, induced by the high pressure gradient, was not only present in the LES but was as well captured by the resolvent method. The velocity profiles near the trailing edge supported this observation by a good fit in the tangential velocity component u_t'.

Considering various improvements, which could be executed in further investigations on both, the resolvent and the LES, and were discussed in the previous section, better agreement in future work is expected. Mainly the tripping in the resolvent simulation could be addressed.

Different kinds of approaches could be realized to force other instability mechanisms than the development of Tollmien-Schlichting waves in the simulation observed here. Therefore an overlap between the modes at the leading edge and the Kelvin-Helmholtz structures could be eliminated and a more clear result of the instability mechanism due to the positive pressure gradient could be obtained. Furthermore research in the field could cover the examination of the high amplified structures appearing in the wake, which have not been in the focus of this thesis.

In the end further research in the modeling of coherent structures by resolvent-based modeling is promising and could yield a fast and accurate method for the calculation of important flow features. This method would help to control the flow and tackle issues like noise emission by wind turbines or other devices.

References

[Dry58] Hugh L. Dryden. "Combined effects of turbulence and roughness on transition". In: *ZAMP Zeitschrift für Angewandte Mathematik und Physik* 9 (1958).

[Wel67] P. Welch. "The use of fast Fourier transform for the estimation of power spectra: A method based on time averaging over short, modified periodograms". In: *IEEE Transactions on Audio and Electroacoustics* 15 (1967).

[RH71] W.C. Reynolds and A.K.M.F. Hussain. "The mechanics of an organized wave in turbulent shear flow. Part 3. Theoretical models and comparisons with experiments". In: *Journal of Fluid Mechanics* 54 (1971).

[Dre89] Mark Drela. "XFOIL: An Analysis and Design System for Low Reynolds Number Airfoils". In: *Conference on Low Reynolds Number Airfoil Aerodynamics* (1989).

[Ger+91] Massimo Germano et al. "A dynamic subgrid-scale eddy viscosity model". In: *Physics of Fluids A: Fluid Dynamics* 3 (1991).

[Lil92] Douglas Lilly. "A proposed modification of the Germano subgrid-scale closure method". In: *Physics of Fluids A: Fluid Dynamics* 4 (1992).

[MLC94] C. Meneveau, T.S. Lund, and W. Cabot. "A lagrangian dynamic subgrid-scale model of turbulence". In: *Center for Turbulence Research Proceedings of the Summer Program* (1994).

[Jas96] Hrvoje Jasak. "Error Analysis and Estimation for the Finite Volume Method with Applications to Fluid Flows". PhD thesis. 1996.

[Pop00] Stephen Pope. *Turbulent Flows*. Cambridge University Press, 2000. ISBN: 978-0-521-59886-6.

[DY01] Mark Drela and Harold Youngren. *XFoil 6.9 Documentation*. 2001. URL: https://web.mit.edu/drela/Public/web/xfoil/xfoil_doc.txt (visited on 10/29/2020).

[Sag02] Pierre Sagaut. *Large Eddy Simulation for Incompressible Flows*. Springer, 2002. ISBN: 978-3-662-04697-5.

[Sel03] Michael Selig. "Low Reynolds Number Airfoil Design Lecture Notes". In: (2003).

[LL04] David Lockard and Geoffrey Lilley. "The Airframe Noise Reduction Challenge". In: *NASA TM-2004-213013* (2004).

[Frö+05] Jochen Fröhlich et al. "Highly resolved large-eddy simulation of separated flow in a channel with streamwise periodic constrictions". In: *Journal of Fluid Mechanics* 526 (2005).

[OBR06] Herbert Oertel, Martin Böhle, and Thomas Reviol. *Strömungsmechanik für Ingenieure und Naturwissenschaftler*. 7th ed. Springer, 2006. ISBN: 978-0-511-29466-2.

[Kit10] Vassili Kitsios. "Recovery of fluid mechanical modes in unsteady separated flows". PhD thesis. 2010.

[SN10] Joseph Spurk and Aksel Nuri. *Strömungslehre: Einführung in die Theorie der Strömungen*. Springer, 2010. ISBN: 978-3-642-13142-4.

[Wol11] William Wolf. "Airfoil Aeroacoustics: LES and acoustic analogy predictions". PhD thesis. 2011.

[MS13] B. J. McKeon and I. Sharma A.S.and Jacobi. "Experimental manipulation of wall turbulence: A systems approach". In: *Physics of Fluids* 25 (2013).

[BM15] J. Boudet and F. Monier J.-F.and Gao. "Implementation of a Roughness Element to Trip Transition in Large-eddy Simulation". In: *Journal of Thermal Science* 24 (2015).

[WHS15] Claus Wagner, Thomas Hüttl, and Pierre Sagaut. *Large-Eddy Simulation for Acoustics*. Cambridge University Press, 2015. ISBN: 978-3-658-07785-3.

[Bla17] William Blake. *Mechanics of Flow- Induced Sound and Vibration, Volume 1*. Academic Press, 2017. ISBN: 9780128092736.

[TSC18] Aaron Towne, Oliver Schmidt, and Tim Colonius. "Spectral proper orthogonal decomposition and its relationship to dynamic mode decomposition and resolvent analysis". In: *Journal of Fluid Mechanics* 847 (2018).

[Kai+19] Thomas Ludwig Kaiser et al. "Examining the effect of geometry changes in industrial fuel injection systems on hydrodynamic structures with biglobal linear stability analysis". In: *Journal of Engineering for Gas Turbines and Power* (2019).

[Mor+19] Pierluigi Morra et al. "On the relevance of Reynolds stresses in resolvent analyses of turbulent wall-bounded flows". In: *Journal of Fluid Mechanics* 867 (2019).

[Wag+19] Georges A. Wagner et al. "Resolvent analysis-based pressure modeling for trailing-edge noise prediction". In: *25h Aeroacoustics Conference* 25 (2019).

[YT19] Chi-An Yeh and Kunihiko Taira. "Resolvent-analysis-based design of airfoil separation control". In: *Journal of Fluid Mechanics* 867 (2019).

Appendix

```
/*--------------------------------*- C++ -*----------------------------------*\
  =========                 |
  \\      /  F ield         | OpenFOAM: The Open Source CFD Toolbox
   \\    /   O peration     | Website:  https://openfoam.org
    \\  /    A nd           | Version:  7
     \\/     M anipulation  |
\*---------------------------------------------------------------------------*/
FoamFile
{
    version     2.0;
    format      ascii;
    class       dictionary;
    location    "system";
    object      fvSchemes;
}
// * * * * * * * * * * * * * * * * * * * * * * * * * * * * * * * * * * * * * //

ddtSchemes
{
    default          backward;
}

gradSchemes
{
    default          Gauss linear;
}

divSchemes
{
    default          none;
    div(phi,U)       Gauss linear;
    div(phi,k)       Gauss limitedLinear 1;
    div(phi,flm)     Gauss limitedLinear 1;
    div(phi,fmm)     Gauss limitedLinear 1;
    div(phi,B)       Gauss limitedLinear 1;
    div(B)           Gauss linear;
    div(phi,nuTilda) Gauss limitedLinear 1;
    div((nuEff*dev2(T(grad(U))))) Gauss linear;
}

laplacianSchemes
{
    default          Gauss linear corrected;
}

interpolationSchemes
{
    default          linear;
}

snGradSchemes
{
    default          corrected;
}

wallDist
{
    method meshWave;
}


// ************************************************************************* //
```

Appendix I: fvSchemes

```
/*--------------------------------*- C++ -*----------------------------------*\
  =========                 |
  \\      /  F ield         | OpenFOAM: The Open Source CFD Toolbox
   \\    /   O peration     | Website:  https://openfoam.org
    \\  /    A nd           | Version:  7
     \\/     M anipulation  |
\*---------------------------------------------------------------------------*/
FoamFile
{
    version     2.0;
    format      ascii;
    class       dictionary;
    location    "system";
    object      fvSolution;
}
// * * * * * * * * * * * * * * * * * * * * * * * * * * * * * * * * * * * * * * * * * * * * //

solvers
{
    p
    {
        solver          GAMG;
        tolerance       1e-6;
        relTol          0.1;
        smoother        GaussSeidel;
        nCellsInCoarsestLevel 20;
    }

    pFinal
    {
        $p;
        smoother        DICGaussSeidel;
        tolerance       5e-07;
        relTol          0;
    }

    "(U|k|nuTilda)"
    {
        solver          smoothSolver;
        smoother        symGaussSeidel;
        tolerance       1e-07;
        relTol          0.1;
    }

    "(U|k|nuTilda|flm|fmm)Final"
    {
        $U;
        tolerance       1e-07;
        relTol          0;
    }

}

PIMPLE
{
    nOuterCorrectors 7;
    nCorrectors     1;
    nNonOrthogonalCorrectors 1;

    pRefCell        1001;
    pRefValue       0;

}


// ************************************************************************* //
```

Appendix II: fvSolution